JPRS-JST-88-025
4 NOVEMBER 1988

JPRS Report

DISTRIBUTION STATEMENT A

Approved for public release;
Distribution Unlimited

Science &
Technology

Japan

OPTICAL COMMUNICATIONS, OPTRONIC
DEVICES MANUFACTURING TECHNOLOGY

19980612 032

DTIC QUALITY INSPECTED 6

SCIENCE & TECHNOLOGY

JAPAN

OPTICAL COMMUNICATIONS, OPTRONIC DEVICES MANUFACTURING TECHNOLOGY

CONTENTS

Techniques of Manufacturing Ultralong Wavelength Optical Fibers

[Article by S. Takahashi, NTT Optoelectronics Research Center]

[Text] 1. **Introduction**

Reducing loss in optical fibers has proceeded along with the development of the long wave band. Initial studies centered on the techniques of manufacturing optical fibers using optical glass of quartz glass through which visible rays could be transmitted; evaluation of the properties was made by using an HeNe laser beam (0.63 μm). In 1970, 20 dB/km (0.63 μm) was achieved with quartz glass. As new manufacturing techniques have been developed since then, wavelengths where low loss is realized have shifted to long wavelengths, from 1.1 dB/km with a YAG laser beam (1.06 μm) to 0.5 dB/km with a semiconductor laser beam (1.2 μm). And now, a minimum loss of 0.2 dB/km has been accomplished at a wavelength of 1.55 μm using quartz optical fiber. This loss is considered a characteristic value of the material.

Since it was judged that further development into a longer wavelength region was necessary research on ultralong wavelength band optical fibers commenced.

Application of ultralong wavelength optical fibers as the transmission medium of the medium infrared ray (wavelengths 2 ~ 10 μm) is also anticipated. There is great demand for these fibers as the transmission medium of a high-output laser such as a gas sensor, a temperature sensor or a carbonic acid gas sensor (10.6 μm). Studies of these ultralong wavelength band optical fibers began near the end of the 1970s. Because of many difficulties involved in the materials, these fibers have not been put to practical use. Basic research to meet demand for such items as ultralow-loss optical fibers and guide fibers for a laser scalpel is continuing.

2. **Details of Development**

Figure 1 shows how the reduction of loss in various optical fibers has been achieved. In quartz optical fibers, following the achievement of 20 dB/km in 1970, development of the MCVD process and the VAD process sharply reduced the optical loss value, to a low 0.2 dB/km in 1979.
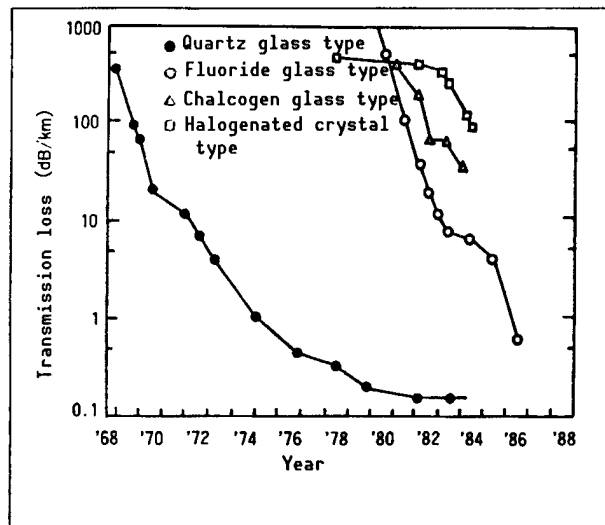
Figure 1. Process of Making Various Optical Fibers Low-Loss

Ever since the possibility of an ultralow loss under 0.01 dB/km was suggested in 1977-1978, work on the ultralong wavelength band optical fiber has been underway to study the materials and to make such fiber. First, a fiber using KRS-5 (TlBr-I) crystals known as X-ray transmissive material was made.

Theoretically, a monocrystal fiber is expected to produce the most reduction in loss because of the absence of factors responsible for diffusion loss such as crystal boundaries and because of extremely small Rayleigh scattering. Actually, fiber-making was so difficult that a loss value on the order of 20 or 30 dB/m was incurred in producing a few meters of fiber.

Glass materials are, after all, suited for fiber-making. Halogenated glass and chalcogen glass with excellent infrared ray transmissivity were examined. For halogenated glass, BeF_2 and $ZrCl_2$ have been long known, but their toxicity and deliquescence make them difficult to use. The ZrF_4 multi-ingredient glass discovered in 1975 is highly promising in this respect, and intensive work is being carried out to study optical fibers using this type of glass.

Chalcogen glass exhibits a comparatively stable glass stage, so making fiber out of this material is easy. Research is being conducted to reduce loss. However, because of the loss factor considered to be inherent in the material itself, it is judged that it will be difficult to reduce the loss to under 10 dB/km.

3. Selection of Materials

As to materials for ultralong wavelength band optical fiber, it is necessary to select materials having excellent infrared-ray transmissivity

The infrared-ray absorbing edge of a material is peculiar to that material and is determined by the constituents and the bonding format. The range of
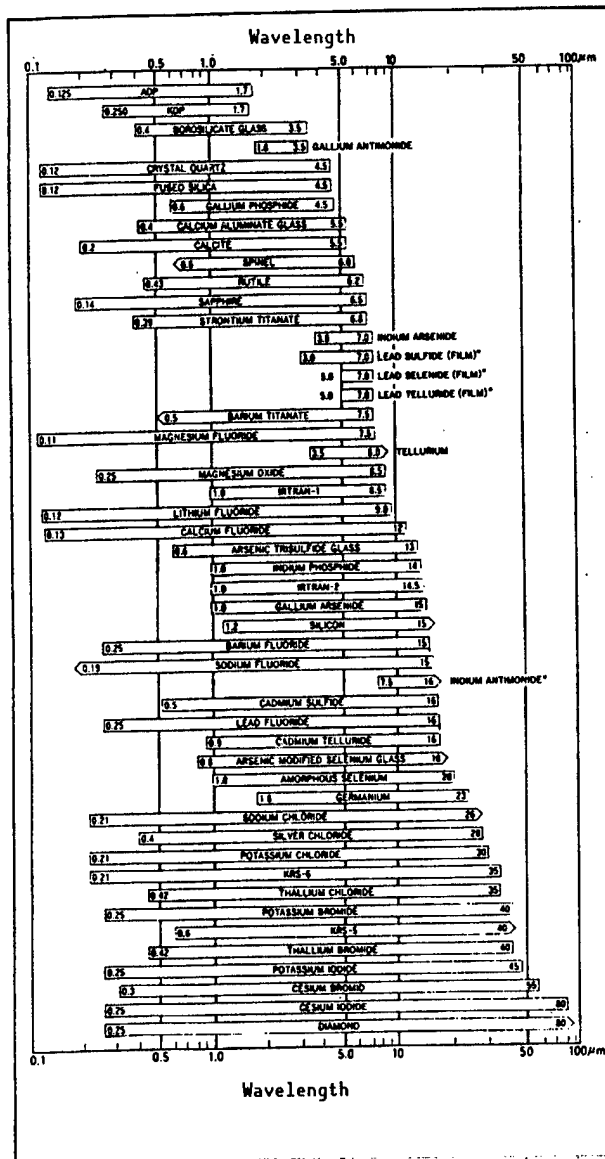
2

Figure 2. Light Transmissive Wavelength Bands of Various Materials

light transmissive wavelengths of various materials is shown in Figure 2. When the constituent atoms are nonpolar and have a strong covalent bond as in diamond, an excellent transmissive property is displayed, although processing such material into optical fiber is difficult. Quartz (SiO_2) is strongly covalent and has a high bonding strength so it is a chemically stable glass; as an optical fiber material, it is better than any other material. But because Si is a comparatively light element, its infrared-ray transmissivity is not on a level with its chemical stability. When Ge, which has a large atomic weight, is used in place of Si, the infrared-ray transmissive property is improved (heavy metal oxide glass). Also, in materials using S, Se or Te, which have a large atomic weight, instead of O (chalcogen glass), the bonding strength weakens and the infrared-ray transmissive property greatly improves.

In BeF_2, which has the same structure as quartz glass, as its ionic strength increases, its bonding strength weakens. Its infrared-ray absorbing edge shifts somewhat to a long wavelength, but it lacks chemical stability.

Halogenated materials with good ionic strength such as KBr and CaF_2 normally excel in infrared-ray transmissive property. As a result, their bonding strength is small and they are difficult to keep in a vitreous state. Another disadvantage is their poor chemical stability. Of these materials, heavy metal fluoride assumes comparatively stable vitreous state (fluoride glass) and its infrared-ray transmissive property is excellent. Consequently, extensive R&D is being conducted on this material as one of the most promising materials.

The techniques of manufacturing optical fibers using fluoride glass, chalcogen glass, heavy metal oxide glass, and halogenated crystals, and their properties, are outlined here.

4. Techniques of Manufacturing Fluoride Optical Fibers

4.1 Glass Composition

A typical composition of the fluoride glasses studied for use in optical fiber is shown in Table 1. Although the glasses shown in this table are more stable in regard to crystallization than other fluorides, they are more prone to crystallization than ordinary oxide glasses and their vitrification calls for quenching.

Table 1. Composition of Fluoride Glasses for Optical Fiber Use

	Composition (mol %)									
Glass	ZrF_4	BaF_2	LaF_3	GdF_3	YF_3	AlF_3	PbF_2	CaF_2	LiF	NaF
1	61.8	32.3		3.9		2				
2	57.5	33.5	5.5			3.9				
3	57	36	3			4				
4	60	31	1	4		2.5	1.5			
5	51	16	5			3	5		20	
6	58	15	6			4				21
7		20			17	43		20		

Mainly composed of ZrF_2 and BaF_2, they contain rare earth elements such as La and Gd. For use in optical fiber, it is desirable to have as few constituents as possible in order to achieve high purity and uniformity of the glass. However, as in the case of ordinary glass, the more constituents there are, the greater the stability, the result being four to six constituents in a material.

4.2 Techniques of Manufacturing Optical Fibers

Because of the instability of the vitreous state, the manufacture of fluoride optical fiber calls for techniques totally different from those used for manufacturing quartz optical fiber.

4

First, transition metal impurities must be removed from the melted fluoride glass. Steps must also be taken to prevent oxygen and moisture in the air from mixing in. Because OH impurities exert basic absorption upon 2.9 μm, this has considerable effect on the absorption property of the optical fiber. Oxygen impurities, which are a cause of generating crystal nuclei, make unstable fluoride glass more prone to crystallization. Consequently, refined raw materials are completely fluorinated by $MJ_{4HF}2$ and melted and vitrified in a dry inert gas.

Next, optical fibers are manufactured by the preform process. In making preforms having a waveguide structure, original techniques such as the build-in casting method and the rotational casting method have been devised for fluoride glass. In the build-in casting method presented in Figure 3, clad glass melt is cast into a brass mold; before its center solidifies, that section is poured out. The core glass melt is cast into an empty space in the center of the cylinder thus created to produce a waveguide structure of the step type. Since quenching is required for fluoride glass, the casting method is utilized. Another characteristic is the formation of a core clad interface making use of the smoothness of the liquid surface.
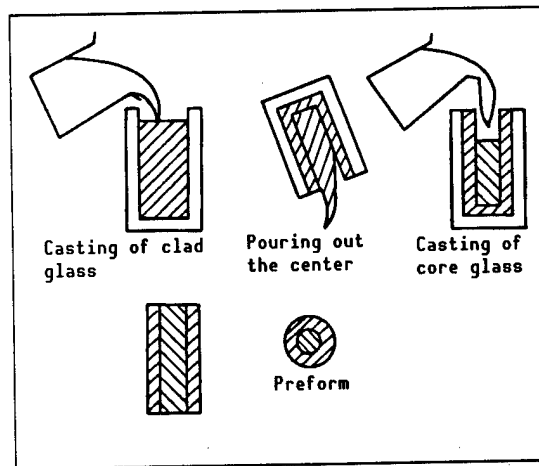

Figure 3. Method of Making a Preform of Fluoride
Optical Fiber by Build-In Casting

When processing the preform into optical fiber (wire drawing), it is necessary to soften it under the temperature of crystallization. Moreover, when the preform is subjected to wire drawing in air as is, crystallization very often occurs from the surface. As a result, the technique used is to jacket it with a fluoride resin tube having roughly equal softening temperature to make a unified piece, which is then subjected to wire drawing.

4.3 Loss Property

The loss spectrum of an optical fiber which obtained a minimum loss of 0.7 dB/km is shown in Figure 4. The startup on the long wavelength side in excess of 3.5 μm corresponds to the infrared-rays multiple phonon absorbing
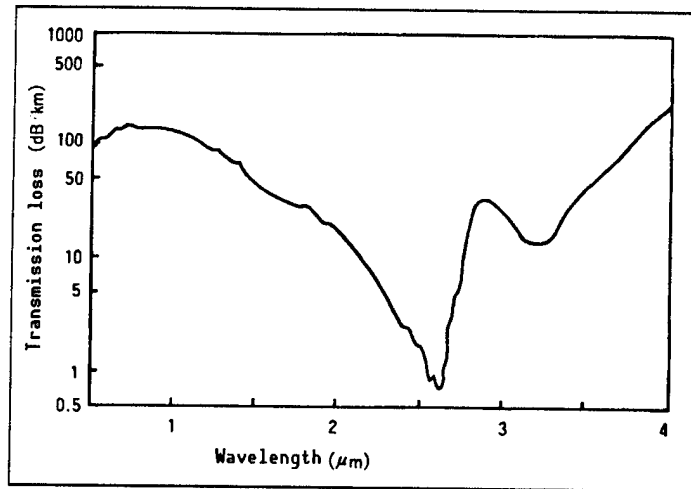
5

Figure 4. Loss Spectrum of Fluoride Optical Fiber

edge. The absorption observed in 2.9 μm is due to the Oh radical, and the absorption peak appearing in 1 ~ 2 μm is due to minute quantities of metal impurity ions. Diffusion loss due to the nonuniformity of glass is large and constitutes an obstacle to minimizing loss.

Single-mode optical fiber is also manufactured. Despite its cutoff wavelength of 2.1 μm with a refractive index difference of 0.47 percent, it has a large core diameter of 11 μm, providing characteristics of ultralong wavelength band optical fiber. Also, the materials diffusion of fluoride glass is less than that of quartz glass--a zero diffusion wavelength of approximately 1.6 μm.

5. Techniques of Manufacturing Chalcogen Optical Fibers

5.1 Glass Composition

For chalcogen glass for optical fiber, the AS-S type, AS-GE-SE type, and, for 10.6 μm transmission fiber, the Ge-As-Se-Te type, are being examined. Of the two-component glass types, the As-S type is the most stable glass, having a red color with a transmission window of 0.6 ~ 13 μm. The As-Ge-Se type, which is opaque in the visible range, is a glass exhibiting metallic luster (a transmission window of 0.8 ~ 19 μm). It is reliable as material for fiber transmitting a ray of 10 μm. However, the Ge-As-Se-Te type is more promising as material for 10.6 μm.

5.2 Techniques of Manufacturing Optical Fibers

Because of the high vapor pressure of the constituent elements and the ease of oxidation, the manufacture of chalcogen glass is performed by the vacuum seal melting method into a quartz ampoule.

For wire drawing to fiber, the double crucible method is possible by the rod method in view of its higher stability to crystallization than fluoride glass. A schematic representation of this is given in Figure 5. In the
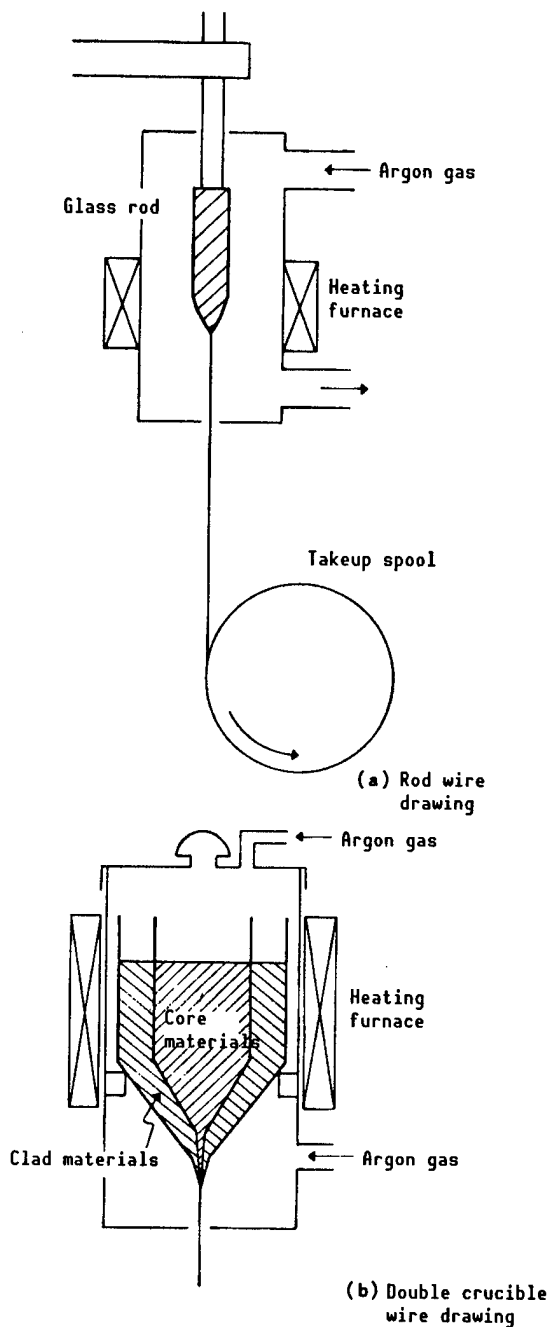
6

Figure 5. Schematic Diagram of Wire Drawing of
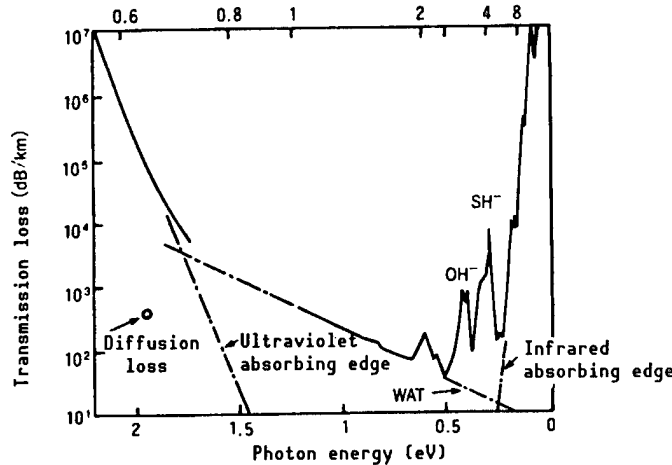Chalcogen Optical Fiber

double crucible method, by changing composition, a step type waveguide with
different refractive index core clad can be structured. In the rod method,
however, the waveguide structure is plastic clad or loose tube clad. On
both methods, oxidation during heating is prevented by assuring that Ar gas
is run in the furnace to maintain an inert atmosphere.

7

5.3 Loss Property
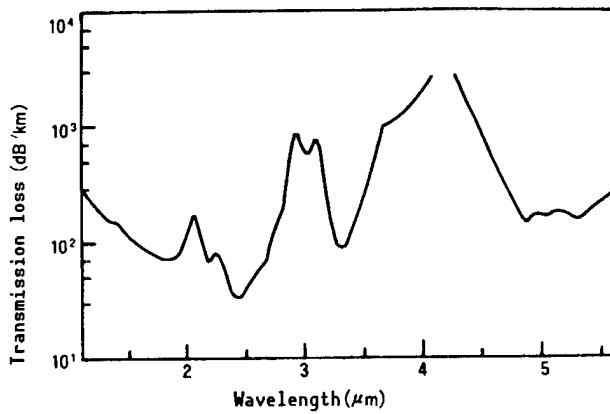
(a) Wavelength dependency of transmission loss

(b) Photon energy dependency of transmission loss

Fiugre 6.   Loss Spectrum of As-S Type
             Optical Fiber

Figure 6(a) shows the loss spectrum of As-S type optical fiber, in which the lowest loss value, 35 dB/km (2.44 μm), was obtained in chalcogen optical fiber. The characteristics of the loss property of chalcogen optical fiber are an absorption peak in 2 ~ 5 μm through SH and SeH in addition to OH impurities, serving as an obstacle to loss minimization, and a considerable WAT (weak absorption tail) or absorption generated by a defect such as a dangling bond of the glass itself. In Figure 6(b), which shows the loss spectrum with respect to photon energy, the WAT is clearly seen as a straight line portion in 1 ~ 2 μm, thus indicating a larger loss than the measured value of diffusion loss. if the WAT is a loss factor peculiar to the material, the estimated minimum loss of this type comes to about 10 dB/km, and the realization of ultralow-loss optical fiber is considered difficult. In the chalcogen optical fiber, to cope with the transmission window spreading to the medium infrared zone, loss in the vicinity of 5 μm is held under 0.2 dB/km, and even in the vicinity of 10 μm, an optical fiber (the type including Se and Te) on the order of 1 dB/km is realized. One field of application is as a medium of power transmission.

6.   Techniques of Manufacturing Heavy Metal Oxide Optical Fibers

6.1   Glass Composition

It has long been known that heavy metal oxide glass excels in infrared-ray transmissive property. However, there are very few examples of it being studied for use in optical fibers. Because GeO_2 type glass using Sb_2O_5 as a stabilizer can be used for making preforms through the VAD process, it has been reviewed for use in optical fiber. Furthermore, there are reports of

manufacturing fiber of comparatively good infrared-ray transmissive property using TeO_2-ZnO-BaO type glass.

6.2 Techniques of Manufacturing Optical Fibers

The VAD process was developed as a technique for manufacturing quartz optical fiber, and heavy metal oxide glass optical fiber has been manufactured using this technique. For raw materials, $GeCl_4$ and $SbCl_5$ were used. Through fire hydrolysis, oxide glass particles are accumulated and used for making porous glass preforms. Because of refractive index control by the addition of Sb_2O_5, fiber NA is a small 0.09, so the waveguide structure is incomplete.

The wire drawing process is conducted in the same way as in the quartz type. The softening point is low and the wire drawing temperature is approximately 1,000°C.

6.3 Loss Property

The loss spectrum of GeO_2-Sb_2O_5 optical fiber is shown in Figure 7. In silicon resin coated fiber, absorption by silicon is observed (Figure 7(a)). On the other hand, an evaluation of glass materials without coating indicates that the minimum loss is under 5 dB/km in the zone of a wavelength of 2 μm, as shown in Figure 7(b). The absorption peak in the spectrum results from OH. Because of the use of the VAD process, the effect of transition metal impurities is not observed. But diffusion loss due to the instability of glass is so substantial as to make it very difficult to obtain ultralow loss.
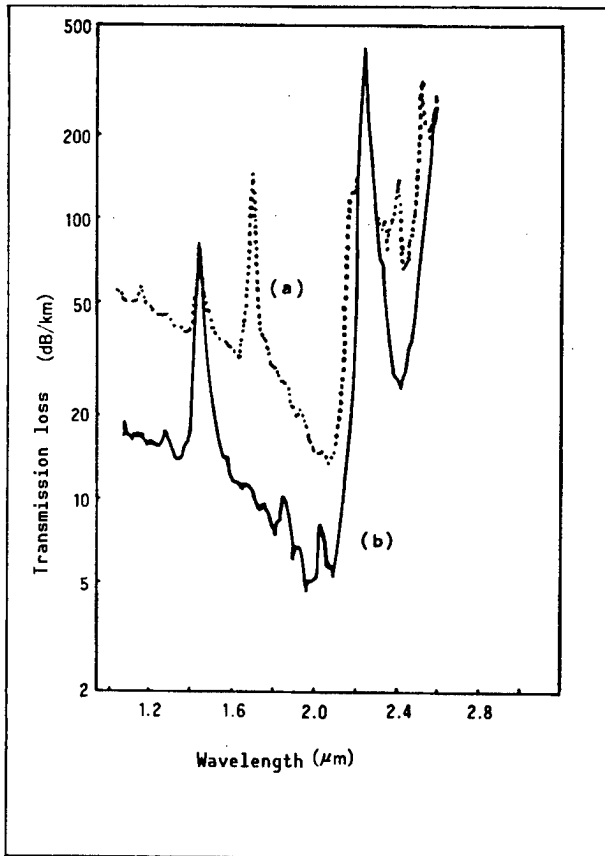

Figure 7. Loss Spectrum on GeO_2-Sb_2O_5
Type Optical Fiber

9

7. Techniques of Manufacturing Halogenated Crystal Optical Fibers

7.1 Fiber Materials

Many infrared-ray transmission crystal materials can be cited. For optical fiber materials, those materials prone to plastic deformation are selected in consideration of wire drawing processing. KRS-5 (TlBr-I), long known as an infrared-ray transmissive material, can be subjected to extrusion processing. Likewise, silver halide crystals can be subjected to extrusion wire drawing for the manufacture of polycrystalline optical fiber.

For single crystal fiber materials, various alkaline halides are available; KCl and CsBr are under consideration. Table 2 lists the main properties of various halide crystals for fiber.

Table 2. Main Properties of Metallic Halide Crystals

Properties / Item		Transmission wavelength [1] band (μm)	Refractory index [2]	Melting point (°C)	Solubility to water [3]	Mechanical properties		
						Hardness[4]	Fiber rupture stress (kg/mm^2)	Elongation (%)
Silver halide	AgCl	0.4 ~28.0	1.98 (10μm)	455	8.9×10^{-5}	9.5	1.8	20.0
	AgBr[5]	0.45~35.0	2.25 (10μm)	434	1.2×10^{-5}	---	2.5	24.0
Thallium halide	TlBr	0.44~48.0	2.338 (10μm)	460	0.05	---	—	---
	KRS-5[6]	0.5 ~40.0	2.371 (10μm)	415	0.02	40.2	6.3	3.1
Alkaline metallic halide	KCl	0.21~30.0	1.454(10.6μm)	776	34.7	9.3	1.1	<1.0
	CsBr	0.22~55.0	1.663 (10μm)	636	124.3	19.5	0.9	25.0
For reference: Quartz glass	SiO$_2$	0.2 ~ 4.5	1.458 (0.6μm)	Softening point 1,710	—	500	530	---

*1 A 2-mm thick crystal sheet with a transmissivity range of over 10 percent

*2 Figures in parentheses indicate wavelengths when the refractive index was measured

*3 Amount in gram to be dissolved in 100 grams of water

*4 Knoop hardness (kg/mm^2, load 200 g)

*5 Silver halide mixed crystals of 98 wt.%, AgBr-2.0 wt.%, and AgCl

*6 Thallium halide mixed crystals of 45.7 mol%, TlBr-54.3 mol%, TlI

7.2 Techniques of Manufacturing Optical Fiber

Polycrystalline optical fiber is produced by the extrusion method. For example, crystal growth of refined AgBr and AgCl is made by the Bridgman process to produce high-purity crystals, which are then placed in a heated container and pressed by an oil pressure press for extrusion forming of fiber with a diameter of 0.5 ~ 1.5 mm. As a result of plastic deformation, the fiber obtained is polycrystalline. Its insertion into a fluorine resin tube produces a loose tube clad fiber. A polycrystalline fiber having a waveguide structure of KRS-5 core and KRS-6 clad is also manufactured. Preforms are made by the rod-in-tube process and subjected to wire drawing by extrusion. By diffusing Cl through heat treatment, a graded waveguide structure is manufactured.

EFG (edge defined film-fed growth) is applied for manufacturing a single crystal fiber at a growth rate of a few millimeters to a few centimeters per minute. Except for the loose-tube-clad type, no other waveguide structure of single crystal fiber is made.

7.3 Loss Properties

The lowest loss optical fiber was obtained from the silver halide group-- 0.07 dB/m for a wavelength of 10.6 μm. This value is sufficient for transmitting any large output for a carbonic acid gas scalpel. Applications to laser processing machines and laser scalpels are being studied. The problem is deterioration on standing of the fiber's reliability and loss. The loss spectrum of graded fibers using KRS-5 and KRS-6 is shown in Figure 8. Although the loss value is affected by the measured NA, low-loss fiber under 1 dB/m is now available. The loss value measured by a 10.6 μm laser (measurement of NA 0.05) is 0.2 dB/m.
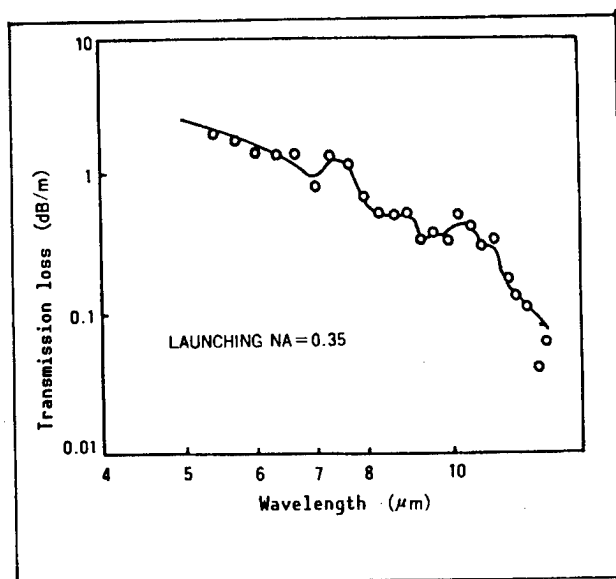

Figure 8. Loss Spectrum of KRS-5 Core,
KRS-6 Clad Optical Fiber

The loss value of single crystal fiber is 10.6 μm, a little under 1 dB/m, but many problems remain to be solved before it can be put to practical use.

8. Application of Ultralong Wavelength Band Optical Fibers

A two-fold application can be considered using the infrared-ray characteristic of superior transmissive property: one is application to an optical communication system by creating an ultralow-loss fiber whose development is anticipated because of its wide transmission window; and the other is direct application of a medium infrared-ray which is transmitted.

In developing low-loss optical fibers for communications, while 0.2 dB/km has been accomplished in a quartz optical fiber, it is essential to achieve ultralow loss beyond this level. The most promising product at present is fluoride optical fiber, and expectations are entertained for further progress in R&D on this subject.

Power transmission, infrared image transmission, and sensors can be cited as field of application directly utilizing the transmissive property of the medium infrared-ray. High-output lasers abound in the infrared region, and the multijoint mirror type is currently available for practical use for power transmission. When the infrared optical fiber does become available, it will be very easy to handle, making possible its application to precision machine processing and the laser scalpel. For a YAG laser of 1.06 μm, quartz optical fiber is adequate; for a CO laser of 5.3 μm, As-S chalcogen optical fiber is appropriate; and for a CO_2 laser of 10.6 μm, silver halide crystal fiber is appropriate.

Application in other fields using the characteristic of infrared-ray transmission, e.g., an infrared-ray image guide by bundling infrared-ray fibers and transmitting infrared-ray images, such as application to a remote temperature sensing system that transmits thermal radiation rays, and a gas sensor that detects a C-H absorbing band in the 3 ~ 8 μm band, is being studied.

9. Conclusion

Since the loss value peculiar to quartz optical fiber was established, intensive studies have been carried out regarding ultralong wavelength band optical fibers. The materials themselves have many inherent problems (a tendency to crystallize because of small bonding strength, and low strength, and reliability), and progress has not been rapid. Nevertheless, the development of ultralong wavelength band optical fibers will have a major impact--ultralow-loss optical fibers and power transmission media--and high expectations are entertained for their progress. It is considered that now is the time to continue development of higher performance fibers and application fields while proceeding with basic studies of the physical properties of the materials.

20107/9365

Techniques for Improving Heat-Resistant Property of Plastic Optical Fibers

[Article by N. Takeya, et al., Hitachi, Ltd.]

[Text] 1. Introduction

In the optical industry field, which is making great strides, optical fibers, as the transmission medium, occupy a critical position. Currently, optical fibers can be roughly divided into glass type (GOF) and plastic type (POF). GOF has low transmission loss, so it is widely used for long-distance transmission.

On the other hand, POF has a large transmission loss. But because of its flexibility, it can have a large-diameter core and it is easy to connect. Other advantages are a loss window in the visible region (660 nm) and ease of handling.

The possible use of POF for short-range communication is attracting attention. In particular, prospects are good for use in optical communications in mobile bodies and optical transmission within equipment or a facility. For example, if it were to be used for all four-wheeled vehicles, counting domestic production of over 1 million cars per month and the possible use of 30 m per car, the size of this potential market alone is immense. For POF to be used for cars, it is necessary to improve its high thermal-resistance and environment-resistance properties, and to achieve high durability, high reliability, significantly lower loss, and lower cost. In particular, thermal resistance is the primary question to be tackled. Overcoming these hurdles will open the way for volume demand for use in cars.

2. Current Status of Plastic Optical Fibers

Reducing loss has been a major task facing POF to date, so this issue was studied. As shown in Figure 1, what was 1,000 dB/km in the initial stage of development came down to under 200 dB/km in the current product level. The loss has been brought further down to 20 dB/km in the laboratory. However, the loss is still larger than that of GOF. At present, many POFs use polymethyl methacrylate (PMMA) as core material. This has low thermal resistance (approximately 80°), so POF is not widely used even for
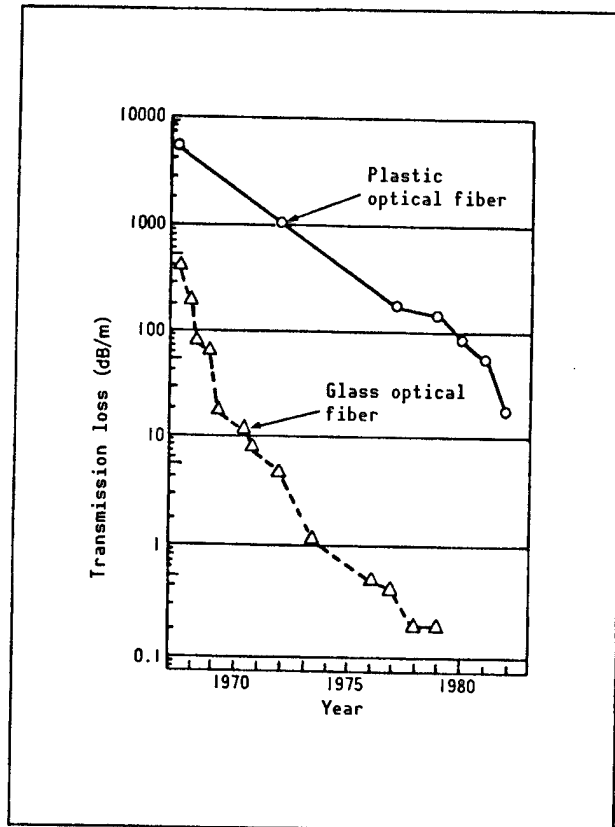
Figure 1. Reducing Loss in Fibers

short-range application. This suggests that when the thermal resistance is improved, the demand for POF will probably skyrocket in view of its application to cars where the market is enormous, as previously noted. Consequently, the emphasis in current POF research has shifted from obtaining low loss to improving thermal resistance.

3. Review of Heat Resistance

Improving POF thermal resistance calls for a review of core materials and clad materials. Above all, the core is where light is transmitted, so transparency is required for the material. At the same time, thermal resistance is a critical requirement. Other requirements are that the clad material be transparent and that its refractive index be lower than that of the core.

As the foregoing discussion points to the large weight that the core occupies in the development of thermal-resistant POFs, the following discussion will center on the thermal resistance of the core section.
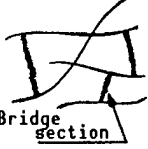
4. Review of Heat-Resistant Core Materials

PMMA has been used for the core material of conventional POFs. This material excels in optical properties, especially transparency. However, its thermal resistance is only up to 80°C, so its use is limited. Generally,

14

the methods of improving thermal resistance include the use of a ring structure within the main chain. This will limit the ease of movement of the segment and increase the hardness of the polymer's main chain. Next, to reduce chemical change at high temperatures, the order of bond is increased. For this purpose, introduction of an aromatic ring is effective. This aromatic ring, together with the above-mentioned ring structure, will meet the requirements. Polycarbonate (PC) is a material having an aromatic ring and excellent transparency. This PC has drawn attention especially as resin for other optical parts. Specially developed for compact disks (CD) in recent years, some PC materials are of optical grade, having excellent transparency. A few years ago, a POF using PC material with its thermal resistance temperature raised to 130°C was announced. And now, there is demand for even higher thermal resistance temperature. Because the aromatic ring generally has strong optical anisotropy, adversely affecting transmission loss, improvement of thermal resistance without using an aromatic ring is sought.

As we have seen, conventional core materials for POFs have been thermoplastic resins that, soften upon heating. However, when a thermoplastic resin that hardens upon heating is used as the POF core material, the amount of deformation upon heating is small, thereby enhancing thermal resistance. A comparison of thermoplasticity and thermosetting resins is given in Table 1. As shown by the schematic diagram, a thermoplastic resin maintains its shape as molecules get wound around. Consequently, heating makes it soft and fluid, and generally its thermal resistance is low. On the other hand, in a thermosetting resin, in addition to its molecules winding around, its molecules bridge one another so that heating does not contribute to deformation. In other words, thermal resistance rises to suppress the movement of the segment and to increase the polymer's hardness.

Table 1. Comparison of Thermoplastic Resin and Thermosetting Resin

Characteristics	Thermoplastic resin	Thermosetting resin
Thermal resistance	Low	High
Optical anisotropy	Large	Small
Flexibility	Large	Small
Fiber-making	Easy	Difficult
Schematic diagram		Bridge section

Furthermore, when a thermosetting resin is used, no stretch process is set up, thus reducing diffusion loss (having an adverse affect as optical anisotropy) due to the stretch orientation generated at the time of spinning, a problem encountered when a conventional thermoplastic resin is used. This orientation due to the stretch process results in increasing

15

diffusion loss, especially in the case of materials having large anisotropy effects of the polarity radical (PS: polystyrene, and PC: polycarbonate).

The foregoing shows that a thermosetting resin is more advantageous as a POF core material with high thermal resistance. However, the thermosetting resin's disadvantage is its general brittleness with low bending strength. And because it consists of many components, an increase in diffusion loss due to compatibility is possible. Taking these factors into consideration, we erected a molecular design and succeeded in developing a bridge type resin of a multicomponent ester type having high thermal resistance and excellent bending strength.

5. Spinning Method of Thermosetting Resins

Thermosetting resins are difficult to make into fibers. Processing up to a general textile have hardly been studied. Therefore, it was necessary to develop a new spinning process concurrently with developing the material.

Because conventional POF utilizes thermoplastic resin, the method of molten spinning is to heat a resin into a molten state and extrude it through a nozzle. But thermosetting resins, when heated, do not assume a molten state, so molten spinning cannot be conducted. Consequently, we considered a process in which the resin is formed into a fiber shape while bridge polymerization is performed. Table 2 presents the concept of the fiber-making process. Also, the condition of the resin inside the tube is schematically shown. A model experimental device for examining this process is outlined in Figure 2. We also reviewed a method of monitoring the polymerization status inside the tube by using a laser beam to control spinning conditions. It was determined that basically, fibers could be manufactured by these methods. An improved process based on this result was developed taking the possible low loss of the POF thus obtained into consideration.

Table 2. Design Concept of Fiber-Making Process

Key points	Countermeasures
Continuous process	Continuous polymerization until shape is held
Uniform polymerization	Uniform heating and suppressing heat generation

Monomer → [...] Polymer →
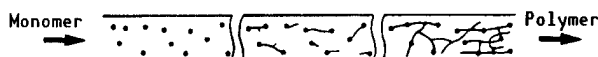
6. Examination of Thermal-Resistant Clad Materials

The clad materials must have a lower refractive index than that of the core materials. Since multicomponent ester type resins were considered for the core material, a fluorine type was used for the clad material.
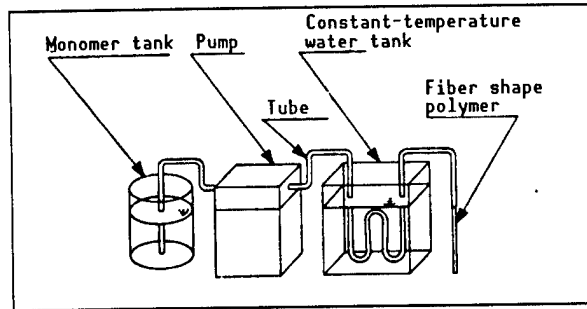
16

Figure 2. Outline of Model Experimental Device

7. Examination of Thermal-Resistant Jackets

An optical fiber with only core and clad structures permits light from outside to enter into the fiber, adversely affecting the transmission properties. Hence, a black jacket is placed outside the clad material. In the case of a thermal-resistant POF, this jacket needs to be studied.

The usual optical fiber has a three-layer structure of core, clad, and jacket, as shown in Figure 3 on the left. When the optical fiber is used under high temperature, its core and clad may jump out of the jacket because of the insufficient thermal resistance of the jacket; as the stretched jacket is heated, it contracts.
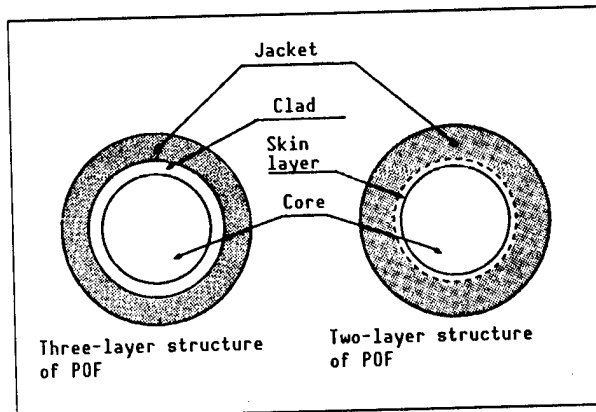

Figure 3. POF Sectional View

To solve this problem, as shown in Figure 3 on the right, POF of a double layer structure, with the core and jacket made by EEP containing carbon, was employed. For the clad, a skin layer of the jacket (surface layer not containing carbon) was used. By enhancing the adhesion between the core nd the jacket the jumping out phenomenon can be prevented, thus improving thermal resistance.

8. Properties of Thermal-Resistant Plastic Optical Fibers

The transmission loss of thermal-resistant POF is, as shown in Figure 4, approximately 1.0 dB/m at a wavelength of 660 nm. An effort to obtain low
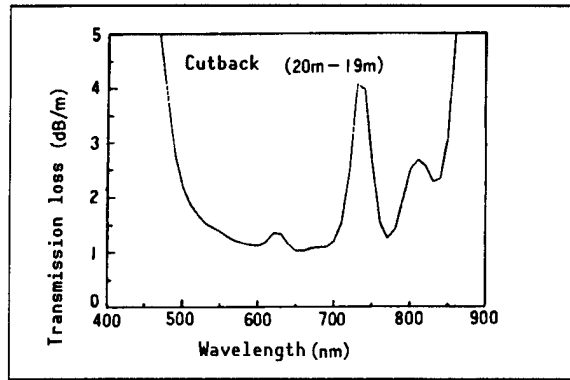
17

Figure 4.   Transmission Properties of Thermal-Resistant POF

loss was made by optimizing the forming and processes, and POF with a loss of 0.5 dB/m (wavelength 660 nm) was obtained. When the loss is 1.0 dB/m, transmission over a distance of some 20 m can be achieved using normal LED (light-emitting diode) and PD (photodiode). It can be adequately used for transmission purposes in cars.

Furthermore, when a powerful light source such as an LD (laser diode) and low-loss POF is used, the POF can serve as an indoor LAN (local network) such as in buildings covering a long distance. This transmission property will be further subjected to study from the standpoint of both the material and the process, so that a further reduction in loss can be achieved.

8.2 Thermal Resistance Property

Figure 5 shows the results of testing thermal resistance when the testpieces were held for 20 minutes at each temperature. The quantity of light holding rate used here indicates the quantity of light at each temperature in percentage, with the quantity of light at room temperature as 100. It is expressed by the following formula:

$$\text{Quantity of light holding rate} = \frac{\text{Quantity of light at at each temperature}}{\text{Quantity of light at room temperature}} \times 100 \ (\%)$$

The squares in Figure 5 pertain to normal POF using PMMA core materials, while the triangles represent thermal resistant POF made of PC core materials. As shown here, POF made of conventional thermoplastic resins, when heated, invariably becomes soft, does not maintain the fiber structure, and cannot transmit light. On the other hand, POF using thermosetting resins exhibits hardly any physical change and excels in thermal resistance. Moreover, it can withstand a service temperature of 200°C for a period of 10 hours.
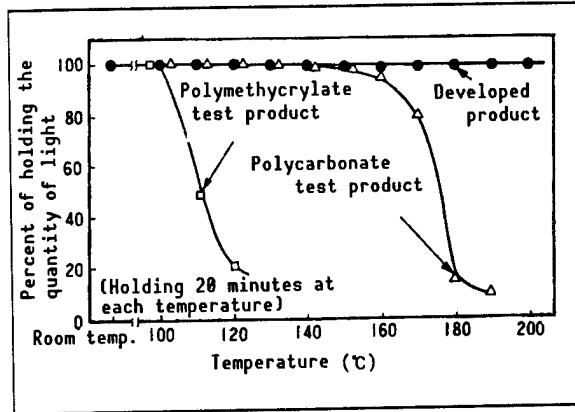
18

Figure 5. Results of Brief Thermal Resistance Test

8.3 Bending Properties

Generally, thermosetting resins as a simple substance are brittle. The bending properties of the POF developed at this time were studied in the material, and its bendable radius (radius free from exfoliation, damage, and any actual service trouble) is under 3 mm (when the core diameter is 1 mm). As shown in the photograph in Figure 6, curl cords can easily be made. Also, because its core material is a bridge resin, its shape-holding property is high. Thus, its characteristic is that the curl shape is difficult to change.
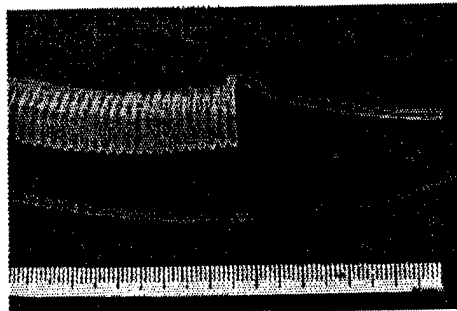

Figure 6. Curl Cord Fiber

9. Postscript

At the beginning of research on thermal resistant POF, our problem was whether to use thermosetting resins for developing both the process and the material using the same material, or to use the conventional method for the process and work on the development of core materials by improving the thermoplastic resins. We elected to take the former course. That decision was based on the consideration that although the developmental task itself was substantial, what was more important was to ensure that the properties of the POF to be developed would be so good as to overthrow established theory. However, the first POF we manufactured a few years ago was enveloped in a glass container and we could not touch it. We never imagined

then that a POF that was that brittle could be developed to the current state, wherein it can be freely bent and curling can be achieved.

In any case, this type of POF has now been developed. Although it is used for various types of sensor, it is not widely in use as yet for data transmission. Should the need for an EMI (electromagnetic interference) shield increase in the future, demand for this type of POF will intensify. Accordingly, the performance of POF will rise increasingly. Our hope is that POF will serve not only as a passive element for merely transmitting light, but will also develop into an active element endowed with function.

20107/9365

II-VI Group Compound Semiconductor Superlattice Formation

[Article by T. Yokogawa, et al., Matsushita Electric Industrial Co., Ltd.]

[Text] **1. Introduction**

Recent years have seen rising demand for short-wavelength light-emitting elements as the light source for high-density light memories. Because of the wide band gap of the direct transition type, II-VI group compound semiconductors such as ZnSe and ZnS are considered the most promising materials for blue light-emitting diodes and blue semiconductor lasers. Consequently, active R&D is now underway to develop techniques of epitaxial growth for II-VI group semiconductors by means of metal-organic vapor phase epitaxy (MOVPE) and molecular beam epitaxy (MBE).

In this paper, superlattice formation technology using MOVPE, which is a highly promising epitaxial growth technology of II-VI group semiconductors, will be mainly discussed.

2. Background to Development of Superlattice Formation Technology

A look at the flow of Si transistor-IC-LSI shows that electronic products follow the road to integration, and this is natural as a technological flow. Likewise, in optical products, all-out efforts are being made to develop optical integrated circuits of optical electronic integrated circuits (OEIC).

The current status of OEIC is represented mostly by reports on trial manufacture of optical devices using semiconductor lasers and photodiodes as well as integration of peripheral electric circuits. In terms of OEIC, this should be interpreted as having just taken the first step. In other words, OEIC today has not reached the stage yet where optical functions are compounded as a substrate to create new optical functions.

This would call not only for setting up an optical device and an electric device parallel on the same substrate but also for forming an optical guide connecting each device on the substrate via light. As optical guide materials that can be expected to create a low loss, they must be materials having an absorbing edge to an even shorter wavelength than the

light-receiving and emitting element materials that make up OEIC. Optical devices are compound semiconductors of the direct transition type. Currently, the InP type and GaAs type of the III-V group from the mainstream. As a result of demand from the high-density optical information processing field, light-emitting elements in the 600 nm band are being put to practical use. In this case, it is necessary to make an optical guide with materials having larger band gap than materials such as AlGaInP. This is difficult to accomplish with III-V group semiconductors.

There are semiconductors having extremely large band gaps in II-VI group compound semiconductors, and low loss can be expected. If such an optical guide of II-VI group semiconductors can be formed on a III-V group semiconductor substrate, a breakthrough can be made in the future development of OEIC.

Moreover, since II-VI group compound semiconductors are materials exhibiting considerable nonlinear optical effect, interest is high in them as materials for the second-harmonic generation (SHG) element that can realize a dream laser beam in blue color. Realization of this calls for the development of low-loss optical guides that excel in enclosing optical waves using II-VI group semiconductors.

Generally, optical guides and other commercially available III-V group semiconductor devices are based on a laminated structure of different types of materials, a so-called heterojunction structure. This heterojunction structure makes it possible to enclose the carriers and light indispensable to electronic and optical devices. However, in II-VI group semiconductors, which are practical enough for short wavelength optical devices, there are no combinations of different types of materials that provide lattice matching as in the AlGaAs/GaAs type of III-V group semiconductors. For example, there is 4.7 percent lattice mismatch between ZnSe and ZnS. Also, because it is difficult to obtain high-grade substrate crystals of II-VI group semiconductors at low cost, substrates of different types of materials having lattice mismatching of GaAs crystals must be used. Therefore, in these heterojunctions, some technique needs to be devised that will achieve a higher grade of crystallinity in the vicinity of the heterojunction interface.

As a means to meet this need and also as a means to control freely the absorbing edge and other physical constants, this company has taken note of the effectiveness of the ZnSe-ZnS strained-layer superlattice (SLS), consisting of an ultrathin-film multilayer structure, and has worked on development of superlattice formation technology using the reduced-pressure MOVPE method.

3. Method of Forming Superlattice

The superlattice structure of III-V group semiconductors is produced by the MOVPE method and the MBE method in which ultrathin-film growth is possible. In forming a superlattice of II-VI group semiconductors, the reduced-pressure MOVPE method, which anticipates the fraction of superlattices having steep interfaces, was used. The growth device was an oblong type

employing the load lock method. For heating the substrate, a high-frequency heating method was used.

For MOVPE growth of ZnSe, an organic metal such as dimethyl zinc (DMZ) and hydrogen selenide (H_2Se) are used as raw materials. However, in this case, under normal pressure growth, DMZ and H_2Se react easily at room temperature to produce nonvolatile complex matter, and it is difficult to obtain quality crystals.

Judging that it would be very difficult to obtain top-quality ZnSe crystals with the H_2Se type, we mainly used, as the raw material of selenium (Se), dimethyl selenium (DMSe), which is metal of weak reactivity, and conducted growth under a reduced pressure below 100 Torr to improve the steepness of the superlattice heterojunction interface. In the conventional growth method, the growing temperature is some 300°C, while a characteristic of the current method is that it is conducted at a somewhat higher temperature level, in excess of 400°C. For the growth substrate, a Cr doped (100) GaAs substrate was used. For pretreatment of the substrate, after it was washed in organic solvent, the surface was subjected to etching by sulfuric acid, then thermal etching was conducted for 20 minutes at 600°C in a hydrogen atmosphere to eliminate surface oxide film. Each layer of ZnSe and ZnS making up the current superlattice structure was formed by switching the raw material gas by automatic valve operation.

When a ZnSe epitaxial layer (film thickness 1 μm) obtained as a single layer was evaluated according to the photoluminescence method (PL) at 4.2 K, no red color emission from a deep level was seen, and light emission from a strong free exciton was observed. This indicated that the ZnSe layer was of high quality. Also, the reflected high-energy electron beam diffraction (RHEED) pattern was in a streak state, and a Kikuchi line was seen. These results confirmed that the surface was very flat with high crystallinity.

4. Evaluation of ZnSe-ZnS Strained-Layer Superlattice

Although there is a lattice mismatch of 4.7 percent between ZnSe and ZnS, making each layer extremely thin will generate no defects such as dislocation due to lattice mismatch (misfit dislocation), so that so-called coherent growth or growth in which the lattices in every layer stretch and shrink becomes possible. Superlattices formed by maintaining such a condition are called strained-layer superlattices, and making them in higher quality can be expected.

After evaluation of the formed ZnSe-ZnS strained-layer superlattices, Figure 1 presents the result of secondary ion mass (SIMS) analysis. The model used was CAMECA IMS-3f, and Cs^{3+} was used for the primary ion. The horizontal axis of Figure 1 shows depth. Each element of Se and S changes periodically, and the lamination by 10 layers each of the ZnSe well layer and the ZnS barrier layer can be confirmed. This testpiece has a period of 10 for ZnSe (50 Å)-ZnS (50 Å), as estimated from the growth rate of each layer. This is in good agreement with the film thickness of each layer estimated from the SIMS profile. It is considered that strained-layer superlattices were formed with good control. Also, when an X-ray locking
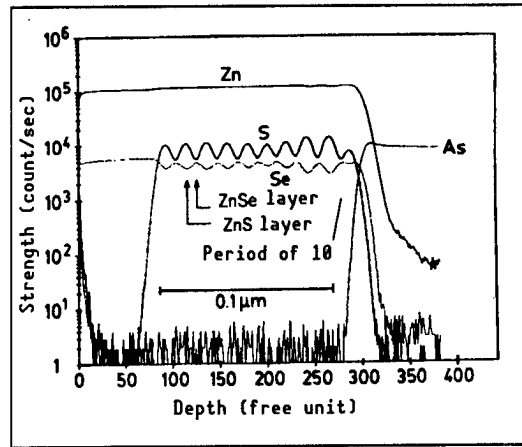
Figure 1.   SIMS Depth Direction Profile

curve is sought by the X-ray two-crystal method, the following so-called satellite reflection peaks--zero degree peak, ± primary peak and ± secondary peak--are found near the GaAs substrate peak. These peaks are evidence that a superlattice structure was formed. Computing the film thickness of one period of the superlattice from this difference in the Bragg angle, we obtained 116 Å, roughly in agreement with the set value (100 Å).
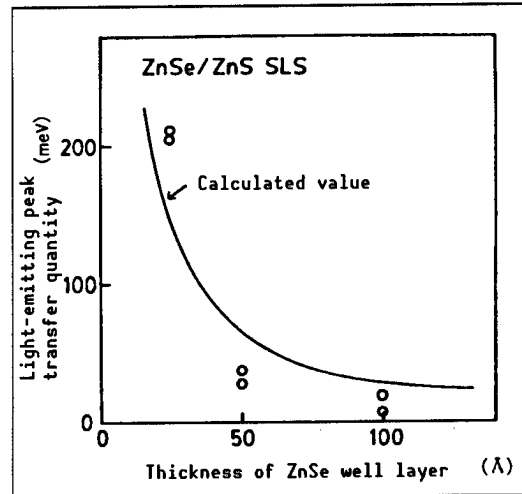

Figure 2.   Dependency of Light-Emitting Peak Transfer Quality
Upon Thickness of ZnSe Well Layer

Next, the optical properties were investigated using PL. This superlattice has a multiquantum well structure.   In this case of III-V group semiconductors, it is well known that when the well width changes, the Pl light-emitting wavelength also shifts. The same tendency was confirmed in the current ZnSe-ZnS strained-layer superlattice structure by changing the ZnSe well width.   Figure 2 shows the dependence of the ZnSe well layer thickness upon the shift quantity of the superlattice light emission peak. This shift quantity was obtained on the basis of the bound exciton light emission (I_x: 2.795 eV) exhibited by the ZnSe epitaxial film.   It is clear that as the ZnSe film thickness decreases, the light emission peak position shifts to the high energy side. When calculating the quantum level of a

24

quantum well structure of the ZnSe-ZnS type, changes in the band structure must be taken into consideration because of considerable lattice mismatch and the generation of respective lattice deformation. From the lattice constants of ZnSe and ZnS, the effective band gap of ZnSe increases, while that of ZnS, conversely, decreases. The results of calculating the quantum level according to the Kronig-Penney model that takes all these factors into consideration give the curve in Figure 2. The fact that this is in good agreement with experimental data confirms that this strained-layer superlattice structure has such superb crystallinity that the quantum size effect can be ascertained.

5. Buffer Effect of ZnSe-ZnS Strained-Layer Lattice

In the field of III-V group semiconductors, also, heteroepitaxy having a large lattice mismatch such as GaAs growth on an Si substrate is drawing attention. It is known that as a means of solving lattice mismatch problems, two-stage growth and a strained-layer superlattice buffer layer of GaP/GaAsP and GaAsP/GaAs are effective. Therefore, we examined ZnSe heteroepitaxial growth (lattice mismatch of 4.7 percent) on ZnS to study the effect of the above-mentioned ZnSe-ZnS strained-layer superlattice buffer layer. The structures of the testpieces evaluated are shown in Figure 3. It is confirmed that these structures constitute optical waveguide structures from the results of calculations taking into account the refractive indices of ZnSe and ZnS. To examine the optical properties of these testpieces, PL evaluation at 4.2 K was conducted. In Figure 4, in the case of ZnSe direct growth on ZnS, light emission from free excitons was not observed; light emission arising from impurities was predominant. On the other hand, when strained-layer superlattices of a 10-layer repair of ZnSe (20 Å)-ZnS (20 Å) were introduced as the buffer layer, light emission due to free excitons was observed.
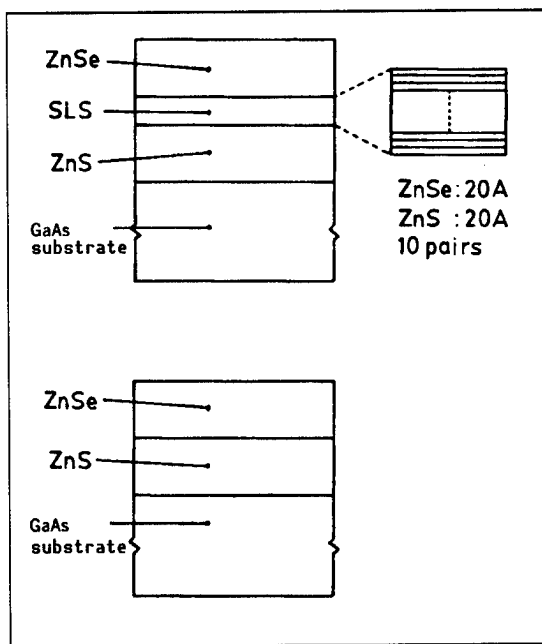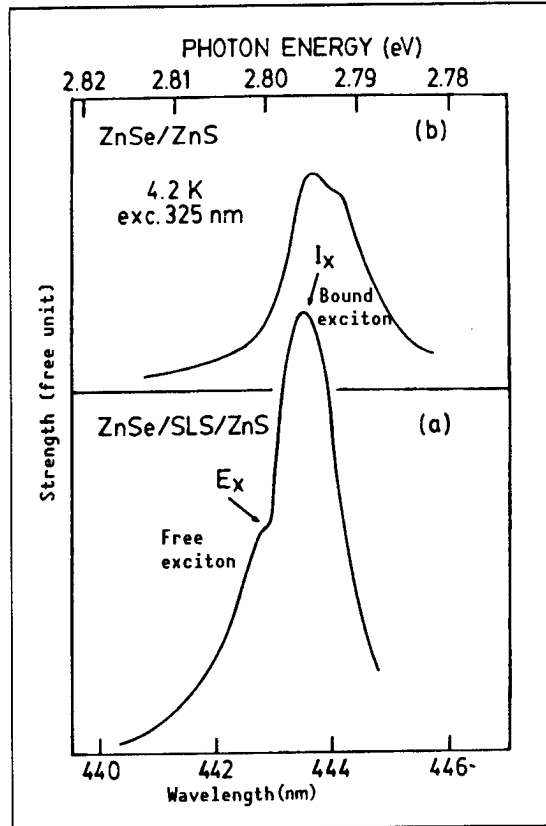

Figure 3. Structure of Test Specimens for Evaluation

Figure 4. PL Spectrum at 4.2 K

Guided by our interest in the behavior of impurities, we also conducted SIMS analysis to investigate the effect of lattice mismatch. In Figure 5(a), a SIMS profile of a structure where ZnSe has directly grown on ZnS is shown. The heterojunction interface is clear from the Se and S element profiles. A close look at the Na element, which is an impurity, shows that most of it has piled up in the interface between ZnSe and ZnS. It is considered that this is caused by mutual action of the Na impurities that move easily in crystals and dislocation due to lattice mismatch, and that the Na impurities are trapped in that dislocation. On the other hand, when strained-layer superlattices are treated as the buffer layer, as shown in Figure 5(b), no pileup of Na impurities was observed on the hetero interface. It follows, then, that this strained-layer superlattice buffer contributes to reducing comparatively the density of defects which can act mutually with impurities.

Figure 6 [not reproduced] presents a cross section photograph by transmission electron microscope (TEM). As shown in Figure 6(a), direct growth propagates a dislocation generated on the heterojunction interface near the surface of the ZnSe layer, whereas, in the case of using the medium of strained-layer superlattices, as in Figure 6(b), it is seen that propagation of the dislocation stops near the interface and that good crystallinity is obtained near the surface of the ZnSe film. This difference is considered to be related to the residual strain in the ZnSe film. To examine this deformation, evaluation was made by the X-ray
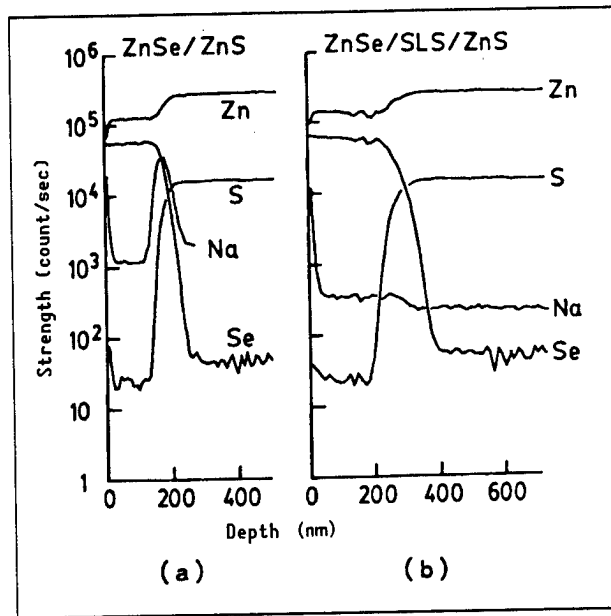
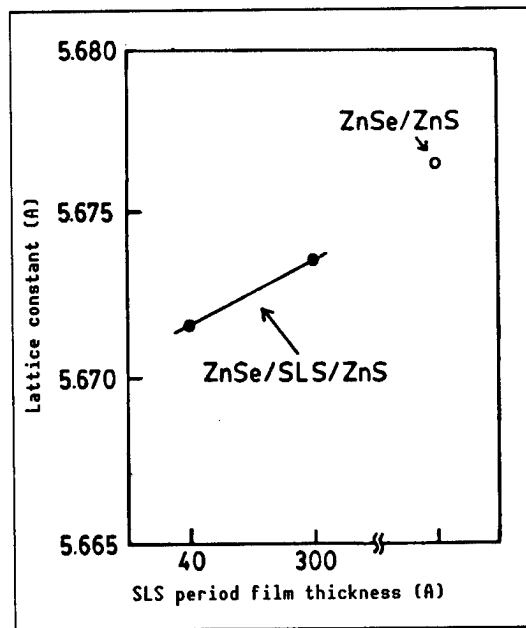26

Figure 5. SIMS Depth Direction Profile

Figure 7. Dependency of Lattice Constant Upon Superlattice Period

two-crystal method. Figure 7 shows the changes in the lattice constant of the ZnSe film. For the X-ray source, (400) reflection of the CuKα1 line was used. In the (400) reflection, the lattice constant vertical to the substrate is obtained as information. The lattice constant of bulk ZnSe is larger than that of bulk ZnS. Because of this lattice mismatch, it is considered that the lattices in ZnSe shrink in a direction transverse to the substrate and stretch in a direction vertical to the substrate. From this, it is concluded that the lattice constant obtained by the X-ray

27

two-crystal method is equivalent to the degree of misfit stress remaining in the film. As shown in Figure 7, when ZnSe is directly grown on ZnS, that lattice constant assumes a large value, signifying the presence of residual strain. On the other hand, when strained-layer superlattices are used as the medium, the lattice constant of ZnSe decreases. Thus, this confirms that strained-layer superlattices act favorably to relieve misfit stress. Furthermore, this effect depends to a great extent on the strained-layer superlattice forming conditions. The smaller the film thickness of one period of superlattice, the more residual strain decreases, thus enhancing the effect as a buffer layer.

6. Formation and Evaluation of Superlattice Optical Guide

From the foregoing, it is clear that the ZnSe-ZnS strained-layer superlattice formed by the reduced-pressure MOVPE method possesses high quality. Next, as an example of superlattice application to devices, an optical guide was made. Figure 8 shows the outline of the element structure of the superlattice tertiary optical guide. To enclose light, it is necessary to set up a low refractive index ZnS between the strained-layer superlattice and the GaAs substrate from the correlation of the refractive index difference with the GaAs substrate. First, ZnS of a thickness of 1.4 μm (film thickness that ensures lattice relaxation) is grown on a (100) GaAs substrate; then, on top of that, 50 pairs of ZnSe (50 Å)-ZnS (50 Å) are continuously grown for a total 0.5 μm strained-layer superlattice (SLS) layer. After that, SiO_2 film to a thickness of 0.3 μm is deposited, and stripes 2 ~ 10 μm wide each are formed by conventional photolithography techniques to make the loading type waveguide structure. Next, the GaAs substrate is ground to a thickness of about 100 μm, and an optical waveguide a few millimeters long is formed, by cleaving. Then, an He-Ne laser beam of 6328 Å is applied from the edge of cleavage.
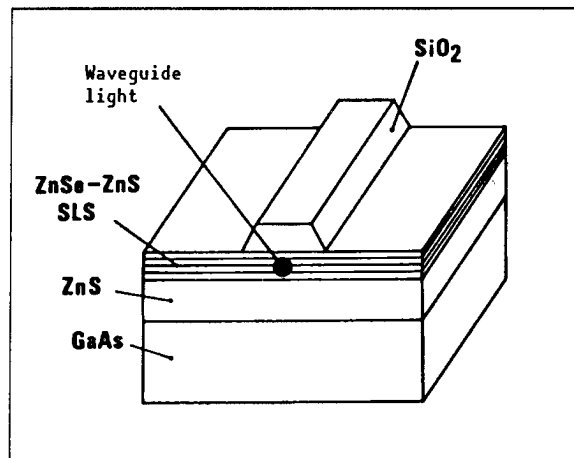

Figure 8. Structure of Loading Type Optical Waveguide

Figure 9 [not reproduced] indicates near field pattern of the transmitted light. The light spot in the center is the transmitted light pattern, and the curve with a peak at the bottom is the light intensity distribution. It is clear that the He-Ne laser beam is enclosed three-dimensionally in

good condition. Formation of a strained-layer superlattice optical guide of II-VI group semiconductors and confirmation of its visible light-guided wave have been achieved for the first time.
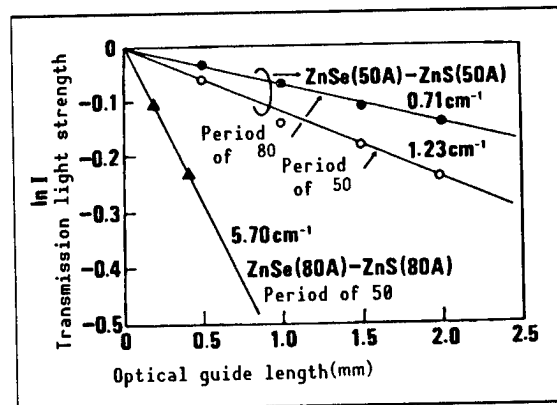

Figure 10. Transmission Light Properties of
Loading Type Optical Guide

Next, we measured propagation loss in the waveguide. Figure 10 shows the dependence of waveguides made under a variety of conditions upon the length of the element. Light transmitted through the waveguide shows attenuation as a result of its peculiar propagation loss, which is calculated from its incline. In the waveguide consisting of optical guide layers of ZnSe (80 Å)-ZnS(80 Å) at a period of 50, propagation loss was large, and $\alpha = 5.70$ cm^{-1} was obtained. On the other hand, when the strained-layer lattice period was further reduced, propagation loss dropped. In the case of ZnSe (50 Å)-ZnS (50 Å) at a period of 50, a comparatively low value of $\alpha = 1.23$ cm^{-1} was obtained. Furthermore, at a period of 80, an extremely low value of $\alpha = 0.71$ cm^{-1} was obtained. These results and optimization of epitaxial growth and structure are very likely to realize an optical guide that can be properly applied to OEIC. Also, this superlattice technology is considered to come into full play as a technology to unify III-V devices, Si devices, and II-IV devices.

7. **Future Development**

Currently, heteroepitaxy on a substrate whose lattice constant differs considerably is drawing attention. As one such technique, GaAs growth technology on Si is highly important as a technology combining III-V devices and Si devices or III-V devices technology using low-cost Si substrates. Already, there are reports of the manufacture of semiconductor lasers and ring oscillators on Si, and properties equal to elements formed over GaAs substrates have been obtained. The current strained-layer superlattice formation technology is critical as a technology combining II-VI devices and III-V devices.

Use of this strained-layer superlattice technology will make it hardly necessary to consider the degree of lattice match in selecting substrates for manufacturing heterojunction devices, thus contributing to increasing the degree of freedom for substrate selection. Moreover, when unifying the

III-V device and the II-VI device, an AlGaAs-GaAs device, for example, a semiconductor laser, is first manufactured at high temperature (700 ~ 800°C). This method assures the absence of thermally adverse effect on the III-V device properties, and, from the standpoint of processing, it is a very worthwhile combination technology.

As discussed above, the method of using a common GaAs substrate to form a III-V optical device or electric device, and then a II-VI optical device (e.g., optical guide), will draw us nearer to the day when a III-V/II-VI optical electronic integrated circuit (OEIC) having complex multiple functions a step beyond the current level becomes a reality.

Thus, II-VI group semiconductor superlattice formation technology is not only significant in the development of II-VI optical devices, but it is also indispensable as a future technology of OEIC. This significance is, indeed, great.

20107/9365

Production Technology for AlGaAs/GaAs Quantum-Well Laser

[Article by O. Wada, et al., Fujitsu Research Center]

[Text] 1. Introduction

The AlGaAs/GaAs laser is now a key device in an optical information system such as the short-wavelength band optical communications system and in optical disks as a result of development since the start of continuous oscillation at room temperature in 1970. This is due largely to the formation of a high-grade, double heterostructure with lattice matching in this material type. Recent developments replacing the conventional liquid phase epitaxy (LPE) method include the metal-organic vapor phase epitaxy (MOVPE) method and the molecular beam epitaxy (MBE) method, which have brought about higher precision, more minute, multilayer heterostructures. Backed by such development of crystal technology, research on the quantum-well laser proceeded almost concurrently with the development of transistors (HEMT, etc.) using two-dimensional electron gas in the electronic device field, bearing fruit in 1981 in the form of a laser with an extremely low threshold current ($250 \ A/cm^2$). In the quantum-well laser, reduction of threshold current, improvement of its temperature properties (increase in T_0), and reduction of the oscillating spectrum width arising from two-dimensional representation of electrons and holes have been realized. The values of these properties have been raised nearly every year, and, particularly in recent years, phenomenal progress has been achieved--e.g., confirmation of the ultrahigh-speed modulation properties due to higher level designs of element structure and application to OEIC [optical electronic integrated circuit) making use of its low power consumption property.

In this paper, recent development of the quantum-well laser using AlGaAs/GaAs materials will be described, and in particular, the production technology and laser properties. The authors have undertaken research for the basic goal of achieving a low threshold value and low power consumption property in the quantum-well laser. Establishing simple and stable production technology suitable for integration has also been a general aim of the research. The following report is based on the results of experiments reviewed during this process.

2. Low Threshold Quantum-Well Laser

2.1 Variety of Quantum-Well Structures

In designing a quantum well to obtain the laser oscillation properties of low threshold and high efficiency, it is important to pay attention to enclosing both the carrier and light. Figure 1 shows the various quantum-well laser structures used for comparing laser properties. In a multiple quantum-well (MQW) structure, the thickness of the GaAs well layer (L_z), the Al composition ratio of the barrier layer (X) and its thickness (L_b), and the number of wells (N) need to be optimized. In a single quantum-well (SQW) structure of graded refractive index waveguide separate confinement (GRIN-SCH), reduction of threshold carrier concentration through the use of a single well and an increase in optical enclosing coefficient through a built-in waveguide are sought. The effort to introduce a superlattice buffer (SLB) is aimed at improving the quality of the quantum-well at the time of MBe growth. Figure 2 shows data on the dependence of threshold current upon the cavity length (L) obtained for these three types of structures. These structures were obtained by MBE growth, and the laser element structure is of the ridge waveguide type, to be discussed later. As is clear from the illustration, the lowest threshold current can be obtained from an SLB GRIN-SCH SQW structure. The accomplishment of such a low threshold is considered to be the result of the multiplier effect of the use of the GRIN-SCH structure, reduction of the probability of nonlight-emitting recouping inside the quantum well, and improvement of optical enclosing through the low refractive index clad layer (X = 0.7). This is also shown in the cavity length dependence of a reciprocal of the differential quantum efficiency (η_d) in Figure 3. In other words, in the structure with SLB, high internal quantum efficiency (η_i = 90 percent) and low waveguide loss (α = 5.3 cm^{-1}) are obtained.
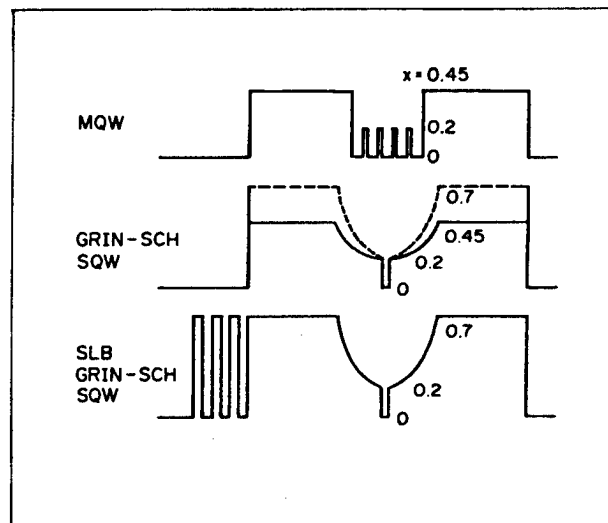

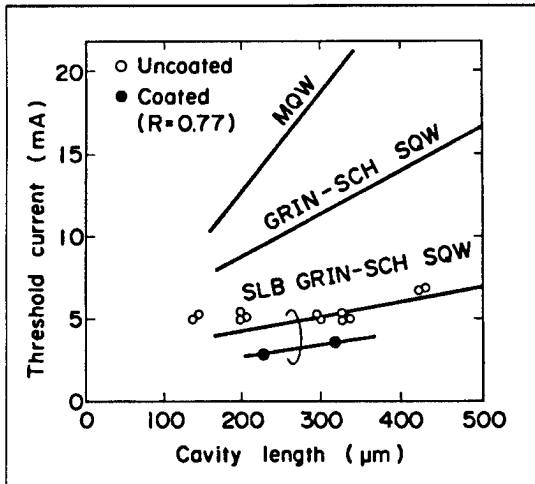Figure 1. Various Quantum-Well Laser Structures

Figure 2. Dependency of Threshold
Current Upon Cavity Length
With Respect to Various
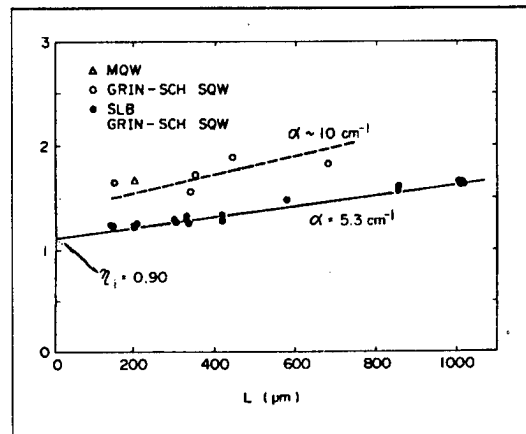Quantum-Well Laser
Structures

Figure 3. Dependency of Reverse of
Differential Quantum
Efficiency Upon Cavity
Length With Respect to
Various Quantum-Well Laser
Structures

2.2 Element Structure

To provide a lower threshold and stable transverse mode, it is essential to
have a built-in refractive index waveguide structure. Figure 4 shows the
element structure of the ridge waveguide laser used for the experiment. The
process required for manufacture was very simple as compared with the buried
hetero (BH) structure: after MBE growth, a ridge waveguide is formed by
etching, and further forming of an insulation film and electrode completes
the process. To assure good waveguide properties, it is necessary to make
a good selection of the clad layer thickness to increase sufficiently the
effective refractive index in the waveguide. The quantity shown as t_R in
Figure 4 is critical. Figure 5 presents the t_R dependence of η_d and I_{th} in
regard to the GRIN-SCH SQW structure, indicating that sufficient waveguide
properties can be realized in a region under approximately 0.4 μm. In
$t_R < 0$, the quantum well will be exposed, thus sharply degrading its
properties. Figure 6 illustrates the waveguide width (W) dependence of I_{th}
and near field pattern measured in a direction parallel to the well layer.
At W = 4 μm or less, a single peak near field pattern is obtained with a
drop in I_{th}. Over an extremely narrow width, the clad layer under the
waveguide and current expansion in a transverse direction inside the quantum
well contribute to suppressing the drop in I_{th}. In this way, optimization
of the ridge waveguide parameter improves the laser oscillation properties.
In the actual production process, a method of forming waveguides by means
of the ion beam etching method is effective in order to determine t_R with
good control. Also, to realize a narrow waveguide width, the flat
photoresist method is used. The data in figures 2 and 3 and in the next
subsection were obtained in the ridge waveguide structure W = 2 ~ 3 μm.
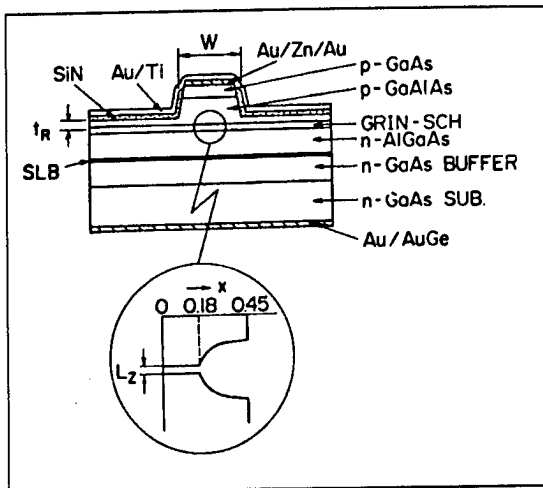
33

Figure 4.   Sectional Structure of
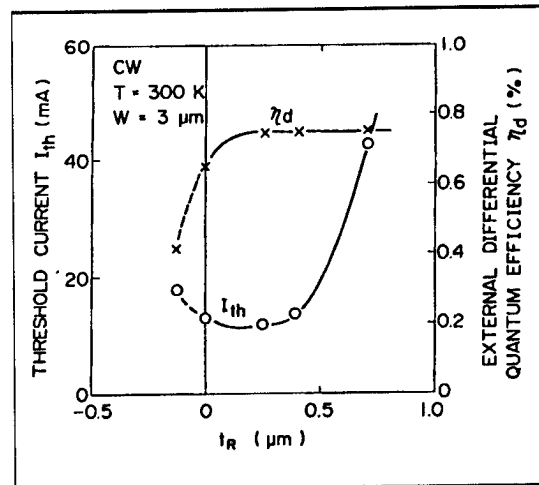Ridge Waveguide Quantum-
Well Laser

Figure 5.   Dependency of Threshold
Current and Differential
Efficiency Upon t_R
(Figure 4) in Ridge
Waveguide Laser

2.3 Element Properties

The representative properties of optimized laser elements as explained above are shown below. Figure 7 shows the current (I)-light output (L) properties at the time of CW oscillation of the SLB GRIN-SCH SQW laser--very good properties with a threshold current of 5 mA and a differential quantum efficiency of 81 percent. As shown in Figure 7, property parameter T_0, representing the temperature dependence of the threshold current, is a high 160 K. Also, in this laser, no element deterioration is seen at least up to 30 mW/facet, and it is considered that for high-output operation, this structure can be used. Vertical mode properties are shown in Figure 8. A spectrum at a bias current (I_b) 1.33 times the threshold current exhibits roughly single-mode oscillation. Furthermore, the spectrum at the time of fluctuation operation when a pulse current of 0.8 I_{th} is repeatedly applied, one pulse on top of another, to a bias current of I_b = 0.9 I_{th} at 1 Gb/s, also exhibits a narrow line width property in a spectrum width of some 0.5 nm. Thus, in the quantum-well laser, a good oscillation spectrum can be obtained at the time of high-speed modulation, too. The high-speed modulation frequency in this laser can be estimated from the optical output power dependence of the relaxation vibration frequency. It can be as high as 8 GHz at an output of 40 MW.

An effective method to realize low threshold properties is to shorten the cavity length so as to increase the reflection factor on the edge, which will result in decreasing loss inside the element structure. Figure 2 presents the result with an effective refractive index (R_f R_y) of 0.77 at L = 230 μm. Figure 9 shows the I-L properties of this element and the element structure. Note that 2.8 mA is obtained as the CW threshold current, and a sufficiently high differential quantum efficiency is obtained for the front optical output. Also, in this laser, a threshold of 0.35 mA
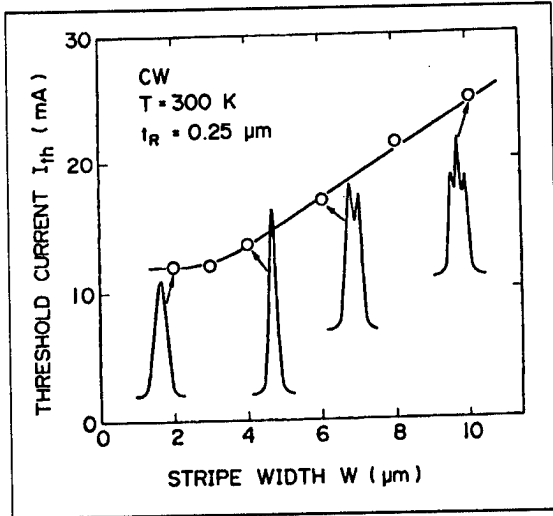
34

Figure 6. Dependency of Threshold
Current in Ridge Wave-
Guide Laser Upon Wave-
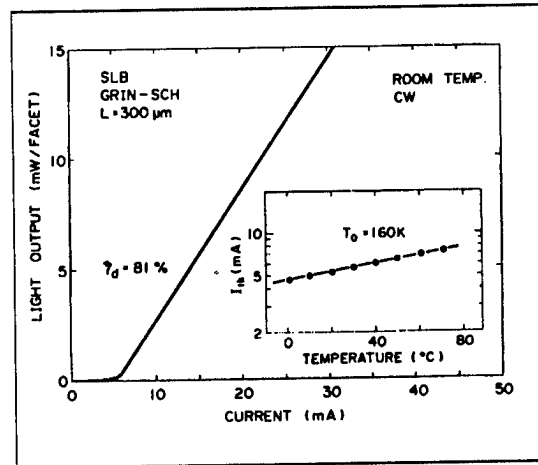guide Width and Near
Field Pattern

Figure 7. I-L Properties of GRIN-SCH
Single Quantum-Well Laser
With Superlattice Buffer
Layer and Temperature
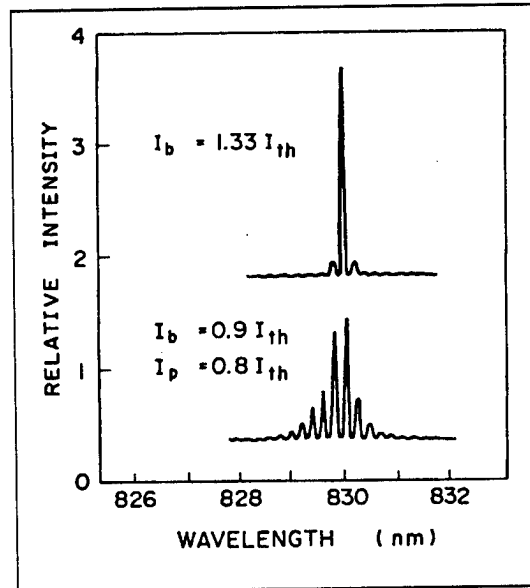Properties of Threshold
Current

Figure 8. Oscillation Spectrums of GRIN-SCH Single
Quantum-Well Laser in CW Operation and in
High-Speed Modulation

at a temperature of 77 K is observed. On the other hand, further
optimization of the cavity length and the edge reflection factor is expected
to realize a threshold temperature of 0.45 mA even at room temperature.
Research on achieving low thresholds through optimization of the structure
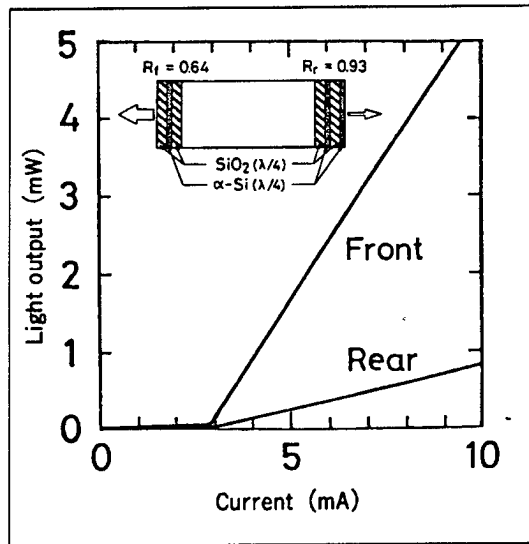
35

Figure 9.   I-L Properties of GRIN-
SCH Single Quantum-Well
Laser With Superlattice
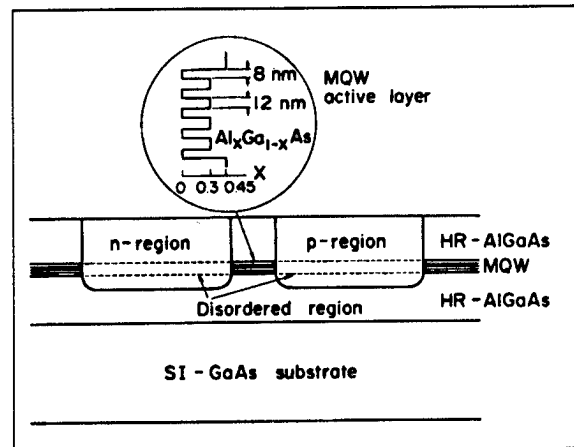Buffer Layer Having High
Reflection Factor Film

Figure 10.   Structure of Lateral
Current Injection (LCI)
MQW Laser

is now being pursued with increasing intensity.   A very recent report
indicates threshold current at room temperature extending to the
submilliampere region (0.9 mA and 0.55 mA).

3.   New Quantum-Well Laser Structure

3.1   Structure of Lateral Current Injection (LCI) Laser Oscillation
Properties

As we have seen, as long as low threshold current and low power consumption
are achieved without impairing good laser oscillation properties, major
contributions can be made to achieving alleys and monolithic integration
with other types of elements (making OEIC), let alone application to
individual laser elements.   However, the main problems in the integration
of lasers are the electrode structure and the manufacturing process.   In the
above-mentioned vertical structure, it is not easy to develop a stable
integration process.   A new lateral current injection (LCI) laser structure
devised from this standpoint is shown in Figure 10.   In this structure, an
MQW structure placed between high-resistance AlGaAs clad layers is used.
P and N electrodes are established on the wafer surface through respective
diffusion of impurities, and a planar structure is thus realized.
Consequently, current injection is not vertical as in the conventional
structure but lateral along the well face.   Furthermore, the prime
characteristic of this laser structure is that the electrode region is made
into a low refractive index zone to obtain a built-in waveguide by using a
disordered phenomenon of the quantum-well structure due to diffusion of
impurities.   The characteristics expected of this laser structure are:

36

(1) Simplification of structure and process
(2) High speed through capacity reduction
(3) Expansion of the degree of freedom in selecting the quantum-well
     structure parameters

The capacity can be reduced to at least under one-tenth that of the conventional ridge waveguide because of reduction of the cross section of the counter electrode. To explain (3), a transverse energy diagram is presented in Figure 11 to show how carrier injection is conducted in the conventional and the current laser structures. In the conventional MQW structure, as explained above, optimization of L_z, L_b, barrier layer composition, etc., is required to assure uniform injection of the carrier into all wells. However, in the LCI structure, carrier injection is primarily made into each well uniformly so that restrictions on the selection of the quantum-well structure parameters are substantially relaxed. Note that because in the LCI structure enclosing the carrier is handled by a potential barrier generated at the disordered P and N electrodes, selection of the structure parameter is critical.

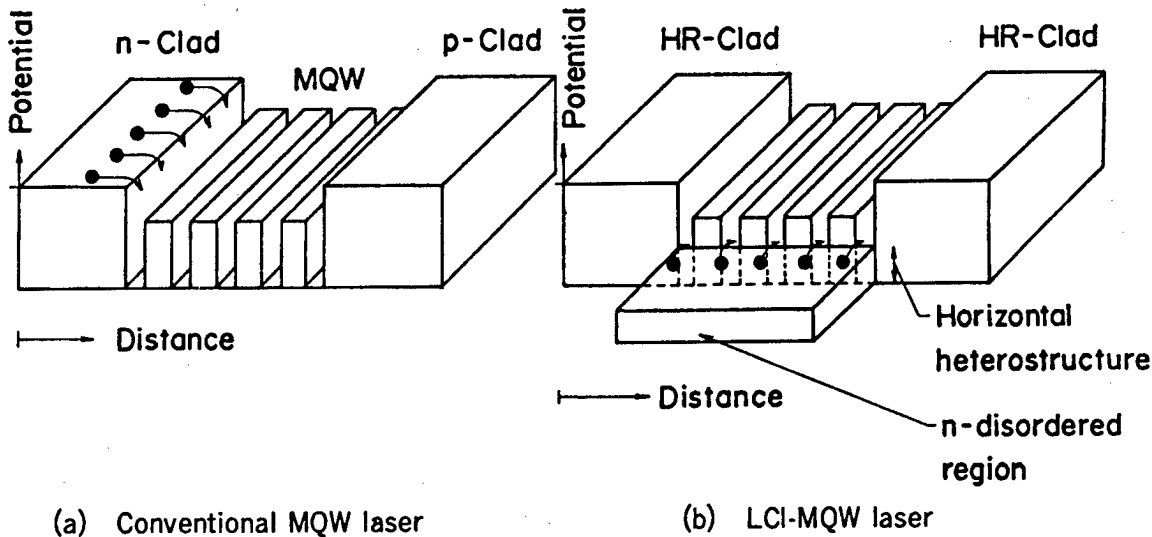(a) Conventional MQW laser   (b) LCI-MQW laser

Figure 11. Potential Diagrams of Conventional Longitudinal Direction
            Structure (a) and LCI-MQW Structure (b)

Figure 12 shows the process flow used in the trial manufacture of the LCI laser. Following mask formation (1) for the diffusion process, N type diffusion process (2) to be conducted with the Si evaporated film as a source, Zn diffusion process (3) by the normal closed tube method, and electrode forming process (4)--these processes form an element. As is clear from this, a very simple production process can be realized. There are also many other advantages such as the stabilization of the distance between electrodes due to self-alignment and the improvement of the possibility of realizing a minute structure through the planar structure.

Figure 13 shows the pulse oscillation properties at room temperature of elements that were experimentally manufactured. It was observed that the
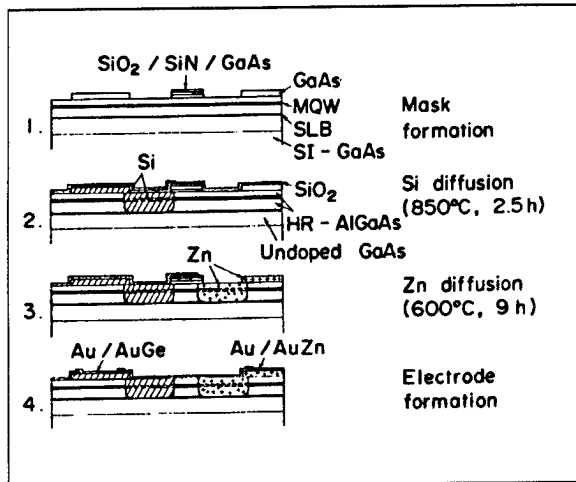
Figure 12. Fabrication Process of
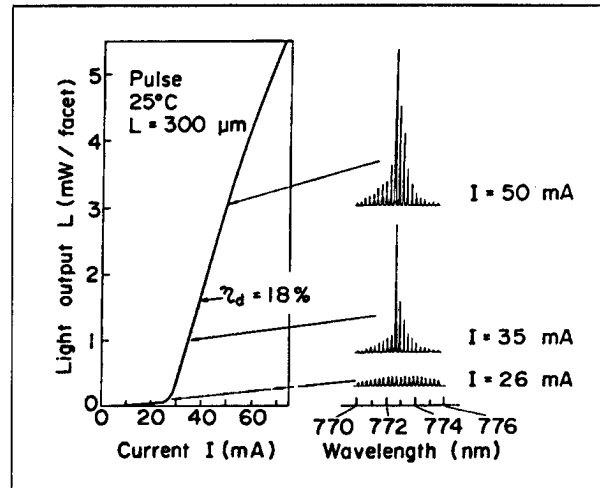LCI-MQW Laser

Figure 13. I-L Properties of LCI-MQW
Laser and Its Oscillation
Spectrum

oscillation properties relied largely on the width between electrodes. In
the case of about 0.5 μm, the properties shown in Figure 13 were obtained.
A threshold current on 28 mA, a differential quantum efficiency of 18
percent and an oscillation wavelength of some 772 nm were obtained. These
results were initial ones, and several problems can be surmised. As for the
success of CW oscillation, increased effectiveness of the carrier enclosing
structure and improvement of electrode serial resistance will probably be
necessary. To improve the differential quantum efficiency, reduction of
optical loss inside the quantum well and the disordered region is probably
necessary. Also, the oscillation wavelength has become quite short
(~ 50 nm) in comparison with the quantization level of the MQW structure
used, conceivably because of disorder proceeding to some extent in the
active quantum-well region, also, during the diffusion process. Therefore,
selection of the structure and process parameter to fit the disordered
phenomenon are required. Recently, some progress has been made in
interpretation of the disordered structure under arsenic pressure and in the
level of comprehension of the effect upon the disordering process of mask
materials for diffusion. This is expected to contribute greatly to
improving the properties of a laser having this structure.

3.2 Application of the LCI Laser

An LCI laser that can be manufactured in a process simplified by a planar
structure is suitable for laser integration. Figure 14 is an example of an
OEIC structure using the vertical-structure QW laser (a) and the LCI laser
(b). Attempts at integration with GaAsFET, etc., by using the QW laser as
in (a) have been made by several research groups, and a four-channel
transmitter alley has been realized to date. Nonetheless, it is difficult
to obtain a sufficiently stabilized process with an integrated structure
having these differences. It is hoped that an LCI laser such as in (b) will
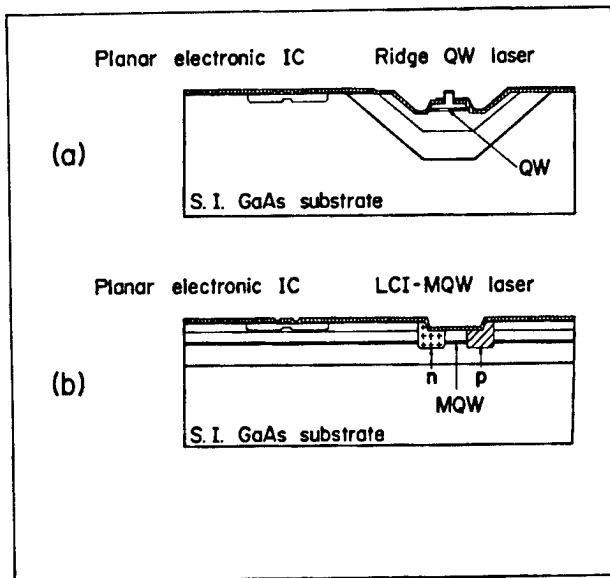be applied to realize a perfect planar structure. Also, in a more advanced

Figure 14. Conventional Longitudinal Structure Laser (a)
and OEIC Structure Using LCI-MQW Laser (b)

quantum-well structure, application to other element structures, including not only lasers but also photodetectors and transistors, is possible. It is hoped that by skillfully using these properties, compatibility between light and electronic elements can be established.

4. Conclusion

In this paper, recent progress in the AlGaAs/GaAs quantum-well laser has been explained from the standpoint of improvement and integration of laser properties. In addition to these directions, studies have been conducted in the areas of obtaining ultrahigh speed and producing short wavelength or visibility. Also in progress is research on realizing a one-dimensional quantum-well structure with an increase in the enclosed dimension, as well as research on providing a modulation function and other new optical functions by actively using the optical properties of excitons existing stably even at room temperature in this material group. On the other hand, there seems to be no case as yet of quantum-well lasers being made commercially available. This suggests that it is necessary for the crystal growth and manufacturing process technology to make further advances on the basis of sufficiently deep knowledge of crystal engineering concerning heterojunction. It is our sincere hope that continuation of these endeavors will bear fruit in the form of optical elements which are useful in terms of both phenomenal improvement of laser properties and realization of new-function lasers and integrated lasers.

20107/9365

39

InGaAsP/InP DFB Laser Manufacturing Process Technology

43064053e Tokyo OPTRONICS in Japanese No 4, Apr 88 pp 95-101

[Article by Y. Hirayama, Toshiba, Ltd.]

[Text] **1. Introduction**

With advances in optical transmission technology, increasingly high expectations are entertained for semiconductor lasers as a light source. In particular, the InGaAsP/InP semiconductor laser has the advantage of an oscillation wavelength of 1.2 ~ 1.6 μm, featuring small transmission loss and wavelength dispersion in the quartz optical fiber. Consequently, its introduction to long-distance, ultrahigh-speed optical fiber transmission has commenced. In 1985, a 1.3 μm band, InGaAsP/InP Fabry-Perot type semiconductor laser was adopted for a route running through Japan (data transmission rate of 400 Mbit/sec and a maximum relay distance of 40 km). This semiconductor laser generates oscillation at many wavelengths during high-speed modulation, and each spectrum of oscillation wavelength varies with the passage of time. As a result, its transmission band due to mode distribution noise is restricted so that it cannot be applied to large-capacity optical fiber transmission systems exceeding the above system. Consequently, development of single vertical mode semiconductor lasers has been carried out, and lasers of various systems have been proposed. Above all, the distributed feedback (DFB: distributed feedback) semiconductor laser formed in periodic irregularities (diffraction lattice) of a pitch of about 0.2 μm in the laser resonator is attracting attention because single vertical mode oscillation can be achieved even at the time of high-speed modulation.

The DFB semiconductor laser has a long history of development. Already in the 1970s, intensive R&D was being conducted on the GaAlAs/GaAs semiconductor laser, but it did not reach the practical stage because of the immature growth technology. After that, development of the InGaAsP/InP DFB laser was actively pursued for optical communication. Recent years have again seen intensive work on developing the GaAlAs/GaAs semiconductor laser in view of the possible application to a photosensor light source.

Figure 1 shows a schematic structure of the InGaAsP/InP DFB laser. To realize the DFB laser, the key technology includes:

(1)   Technology to form diffraction gratings, with good reproducibility, uniformly over a wide area at a predetermined period

(2) Crystal growth technology to grow a thin film over a diffraction grating without destroying that diffraction grating

(3) Wavelength control technology for single mode oscillation with good control because even DFB lasers permit two-mode oscillation
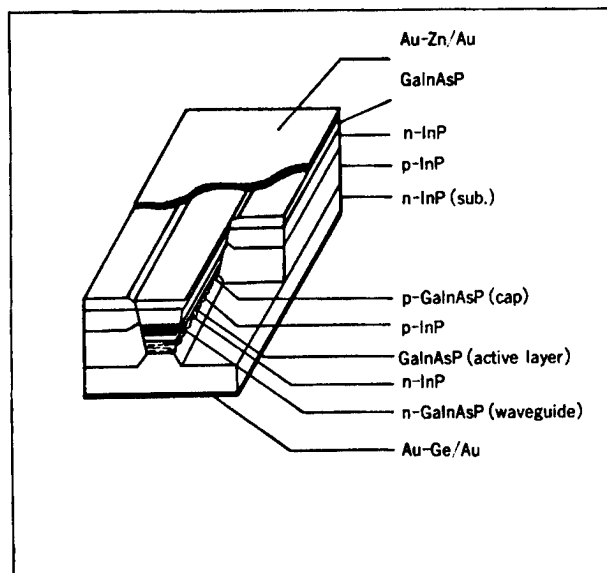

Figure 1.   Structure of InGaAsP/InP Type DFB Laser

In this report, an outline of these technologies is given on the basis of the results of our studies and an introduction is made of the five-wavelength DFB laser with a light source for high-density wavelength multiple transmission which we developed using these technologies. Technologies other than those mentioned above--for example, transverse mode control technology and technology to enable ultrahigh-speed operation--are commonly used with conventional lasers (Fabry-Perot semiconductor lasers), so they are not dealt with in this report.

2. Diffraction Grating Formation Technology

A diffraction grating set up in the vicinity of the active layer is used as resonator in the DFB laser. The period and depth of the diffraction grating are critical factors to determine the oscillation wavelength, threshold current, and mode selectivity of the DFB laser. Consequently, formation of the diffraction grating of a predetermined period and depth with good control and reproducibility is a critical technology to realize the DFB laser. The period of the primary diffraction grating necessary for the InGaAsP/InP DFB laser having an oscillation wavelength of 1.2 ~ 1.6 μm is 2,000 ~ 2,500 A. In forming such a minute pattern, the normal method is first to prepare a diffraction grating over a photoresist coated on the semiconductor surface; then, this is used as mask to be transcribed to the

41

semiconductor substrate. The use of focusing ion beam etching to make a diffraction grating directly on the substrate can be considered, but it is not feasible at present.

The methods of making diffraction gratings on a photoresist include the interference exposure method and the electron beam exposure method. The former is in the mainstream in consideration of productivity and ease of control.

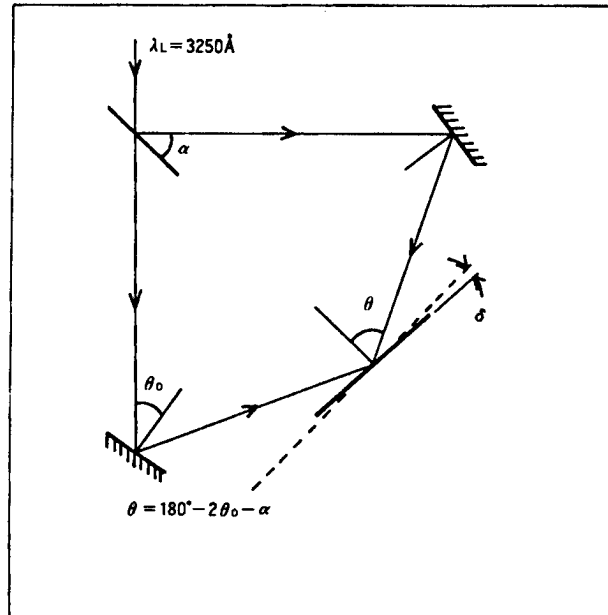$\theta = 180° - 2\theta_0 - \alpha$

Figure 2. Diffraction Grating Fabrication Device
Using Interference Exposure Method

As shown in Figure 2, an interference exposure device separates the incident single color light (wavelength λ_0, an He-Cd laser with a wavelength of 3,250 A used for the experiment), distributes it in two directions through a translucent mirror, and reunites it on the test specimen table. This is a so-called two-beam interference method. A photoresist which has sufficient exposure sensitivity and which has resolving power for the diffraction grating period to be formed is coated on the test specimen surface. The period of interference strip corresponds to the period of the diffraction grating, where period Λ is given by

$$\Lambda = \frac{\lambda_0}{2 \sin\theta \cos\delta} \tag{1}$$

where 2θ is the angle of intersection of two beams and δ is the incline of the test specimen. Oscillation wavelength λ_p of the DFB laser is proportional to the period of the diffraction grating. If the set margin of the oscillation wavelength is expressed by the set margin of the diffraction grating, we obtain

$$\left| \frac{\Delta\lambda_p}{\lambda_p} \right| = \left| \frac{\Delta\Lambda}{\Lambda} \right| = \left| \frac{\Delta\theta}{\tan\theta} \right| + \left| \tan\delta \cdot \Delta\delta \right| \tag{2}$$

42

If the DFB laser's oscillation wavelength is set at 1.3 μm to be controlled within 10 A, an accuracy of $\Delta\theta \leq 1.3 \times 10^{-3}$ rad would be required when $\delta = 0$. Adjustment of this angle is possible with the zero method using a personal computer and a step motor. Use of a step motor with one step 0.25 minute in this method could control $\Delta\Lambda/\Lambda = 1.2 \times 10^{-4}$. Table 1 gives a comparison of the set periods of the diffraction grating with the actual periods of the diffraction period produced. The periods were determined by measuring according to the Bragg condition using the He-Cd laser (direction of the incident ray matches that of the diffraction ray). It is clear that the set values and the formed values of the periods are in agreement within the margin of measured error.

Table 1. Set Values and Formed Values of Diffraction Grating Period (Reference position 1960 Å)

Set values	Formed values	Error (percent)
2,000 Å	2,000.61 Å	0.03
2,100	2,100.92	0.04
2,200	2,200.54	0.02

A diffraction grating on a photoresist is used as a mask when the diffraction grating is transcribed to the surface of the semiconductor substrate. Whether or not the mask can endure at the time of transcription to the substrate determines the optimum exposure condition. Etching methods for diffraction grating transcription to a surface of InP and InGaAsP include a dry process such as reactive ion etching (RIE) and a wet process using chemicals. Because diffraction gratings for the DFB laser are built in the vicinity of the active layer of the semiconductor laser, it is necessary to make them by a method that ensures no damage to crystals. The dry process is considered inferior to the wet process in regard to damage, so the wet process is mostly used.

Photograph 1 [not reproduced] is an SEM photograph of a diffraction grating made by the wet process. When forming a minute structure such as a diffraction grating on the surface of a III-V group semiconductor, use of the etching rate's dependence on the facial orientation make this task relatively easy. In other words, use is made of the fact that because the etching rate is faster on a (111) A surface where III group elements appear than on a (111) B surface where V group elements appear, etching stops at the (111) B surface. When this property is used, a triangular shape, as shown in Photograph 1 [not reproduced], is obtained. For etchants used for making diffraction gratings on the InP and InGaAsP surfaces, there are $HCl:CH_3COOH:H_2O_2$, $HBr:HNO_3:H_2O_2$, and $HBr:HNO_3:CH_3OH$.

To increase the controllability of the vertical mode that will be explained in section 4, a so-called phase shift structure, in which the diffraction grating phase is shifted by a ratio of one to an integer of the period in the middle of the resonator direction, may be used. Basically, this can be dealt with by a variation of the above-mentioned interference exposure method, the explanation of which is omitted here.

3. Crystal Growth Technology Over Diffraction Gratings

3.1 Thermal Deformation of Diffraction Gratings

The crystal growth methods used for making a semiconductor laser mainly include (1) liquid phase epitaxy growth, (2) hydride vapor phase epitaxy growth, (3) metal-organic vapor phase epitaxy growth, and (4) molecular beam epitaxy growth. Liquid phase epitaxy growth, which excels in crystallinity, is a practical technique used for making lasers on the mass-production level, despite its slightly inferior controllability of film thickness and composition. On the other hand, epitaxial growth methods through the medium of vapor phase excel in controllability of film thickness and composition, and their crystallinity is on a par with that of liquid phase epitaxy.

In any of the growth methods, because of the need to supply such energy during growth as to enable adsorption seeds to move to the stability point on the substrate surface, growth takes place at high temperatures from 550°C to 700°C. This necessarily means subjecting the InP of InGaAsP surface on which gratings have already been formed to high temperatures prior to growth. At this instant, phosphor exfoliation and adsorption occur repeatedly, and indium moves from the convex section to the concave section to assure energy stability. The result is that the convex section is shaved low while the concave section is filled, and deformation and disappearance of diffraction gratings take place. When this happens, the periodic quantity of change of the diffraction index lessens and the quantity of light returning diminishes, thus resulting in increasing the threshold and other difficulties.

Consequently, a great deal of R&D effort has been devoted to each growth method to devise techniques for maintaining the diffraction gratings over which to perform crystal growth. At present, in each of the above-mentioned growth methods, a process is available to suit the characteristics of each method in conducting crystal growth without inducing the deformation of diffraction gratings. Accordingly, the properties of elements have greatly improved. A specific process will be explained in this paper for liquid phase epitaxy and hydride vapor phase epitaxy.

3.2 Liquid Phase Epitaxy Growth

Figure 3 shows a schematic diagram of liquid phase epitaxy growth. Usually, this is conducted in a graphite boat in a hydrogen atmosphere. A substrate is placed on a slider in the boat, and in each melt-containing section of the upper part are held source material crystals of GaAs, InAs, and InP appropriate for the composition of the growth film and In to melt them. Usually, in the fabrication of a wafer for a Fabry-Perot laser, an InP single crystal is positioned facing the InP substrate as its protective cover, subjected to a temperature of 670°C, and held there to stand by to make an In melt uniform. After that, gradual cooling takes place. When the temperature drops to about 645°C, the slider is moved to allow the substrate to come into contact with the melt, and crystal growth commences.
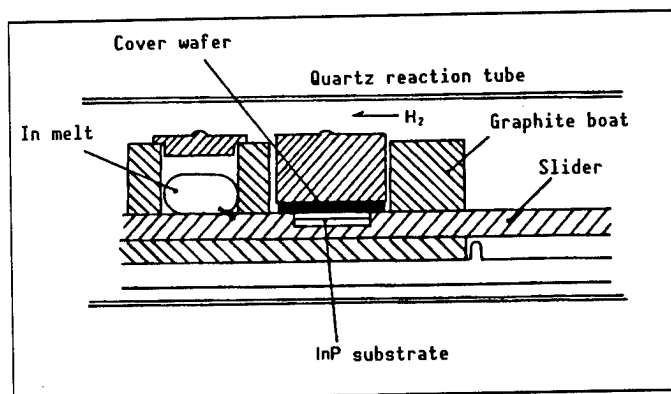
Figure 3. Schematic Diagram of Liquid Phase
Epitaxial Growth Method

In making a DFB laser, the low-temperature growth method is used in which the standby temperature is set at a comparatively low temperature of 600°C and the growth temperature is accordingly set to under 600°C. The reasons are: 1) to minimize phosphor defoliation from a diffraction grating formed on the InP and 2) to increase the controllability of film thickness by reducing the growth rate. The quantity of source materials to be melted in each In can be estimated through thermodynamic calculation. The quantity of InP to be used is very minute. Because of the difficulty of measuring it on a scale, the two-phase melted liquid method is used. In this method, by putting in excess InP crystals, the In melt is made to remain in contact with the source InP crystals at all times. Because the melt's supersaturation degree is low, it also has the advantage of decreasing the growth rate. Accurate quantities of other materials to be used are subject to micro-adjustment by the X-ray two-crystal method to provide for lattice matching on the InP substrate within ±0.02 percent.

In this type of material, a relatively wide thermodynamically unstable region exists. Especially in the case of InGaAsP of a 1.3 μm composition, it is known that, under a growth temperature of under 600°C, approach is made to this region. Nevertheless, when lattice matching was performed within ±0.02 percent, the results of photoluminescence measurements and electroluminescence measurements indicated no specific problem; the intensity of light emitted turned out to be roughly equal to the high-temperature growth. Also, the use of low-temperature growth and the two-phase melted liquid method contributed to the controllability of film thickness, which was relatively good with a 0.1 μm-thick film in a growth time of 5 seconds. It was noted that the use of such low-temperature growth did not completely eliminate the diffraction grating deformation and that its reproducibility was poor.

Consequently, an investigation was made of the relationship between the cover material to protect thermal dissociation of the InP wafer with a diffraction grating and the degree of preservation of the diffraction grating after heat treatment. The results of the experiments are shown in Figure 4. On the right is the number of experiments, and on the left the number of experiments with deformation. In many cases, the InP cover
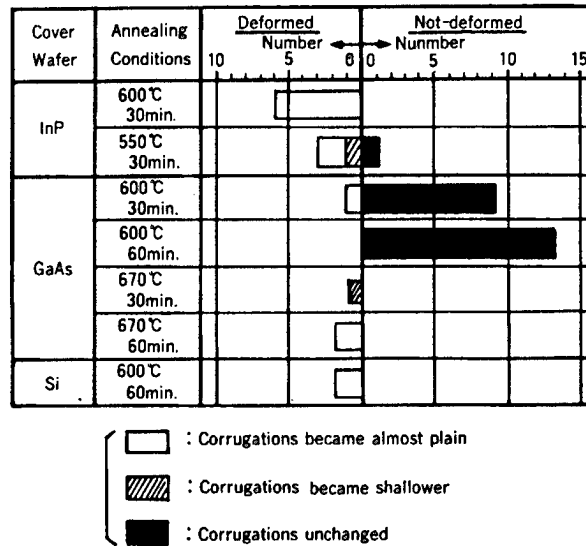
Cover Wafer	Annealing Conditions	Deformed Number (10 ← 5 → 0)	Not-deformed Number (0 → 5 → 10 → 15)
InP	600°C 30min.	□ (≈3, became almost plain)	
InP	550°C 30min.	□▨■ (shallower/unchanged)	
GaAs	600°C 30min.		■ (almost plain, ≈8 unchanged)
GaAs	600°C 60min.		■ (unchanged, ≈12)
GaAs	670°C 30min.	▨ (shallower)	
GaAs	670°C 60min.	□ (became almost plain)	
Si	600°C 60min.	□ (became almost plain)	

□ : Corrugations became almost plain

▨ : Corrugations became shallower

■ : Corrugations unchanged

Figure 4. Correlation Between Cover Materials and Frequency of Diffraction Grating Deformation Under Various Heat Treating Conditions

normally used produced deformation when the temperature was dropped to 600°C or even 550°C. Even an Si cover produced deformation. As compared with the case of holding for 30 minutes at 600°C, the use of a GaAs substrate as cover was found to be remarkably effective. At 600°C for 60 minutes, the diffraction grating was preserved with good reproducibility. Even in this case, deformation occurred at 670°C.

Since arsenic was thought to have some effect on the preservation of diffraction gratings, experiments were conducted when polycrystals of InAs were used as a cover, and they were found to be effective with good reproducibility. From this result, it is considered that diffraction gratings are preserved because arsenic forms an InAsP protective film difficult to deposit on the surface of the diffraction gratings.

These results indicate that the use of a GaAs or InAs protective cover at a low temperature of 600°C can contribute to protecting diffraction gratings with good reproducibility.

After protecting diffraction gratings during standby in this way, growth begins. In the case of a 1.3 μm stripe, the five layers--1.12 μm composition InGaAsP guide layer, n-InP layer, 1.28 μm composition InGaAsP activated layer, p-InP clad layer, and p^{+}-InGaAsP contact layer--grow successively. Photograph 2 [not reproduced] is a cross sectional SEM photograph taken after the growth. It can be seen that the diffraction grating is cleanly buried. A wafer thus obtained has intensity of light emission on a par with that of high-temperature growth, and the low threshold DFB laser is obtained.

3.3 Hydride Vapor Epitaxial Growth

Figure 5 shows a schematic diagram of hydride vapor phase growth. With two growth chambers, the substrate is held vertical to the gas stream. Through a rapid substrate transfer between growth chambers, each composition film can be made to grow swiftly and consecutively. For Group III materials, metallic chlorides are generated by poring hydrogen chloride gas diluted in hydrogen over the In and Ga melt. This and a gas mixed with arsine and phosphine of Group V materials precipitate to form a film. Normally the metal source is held at 820°C and the substrate at 670°C.
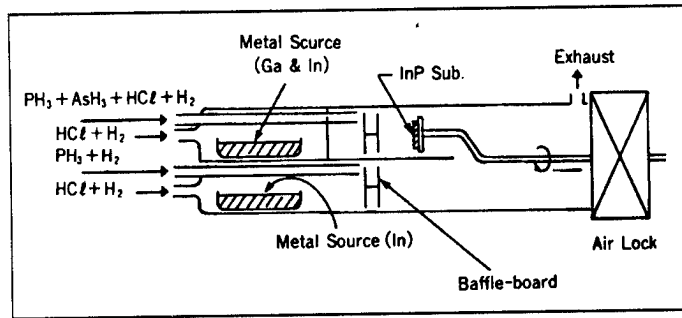
Figure 5. Schematic Diagram of Hydride Vapor Phase
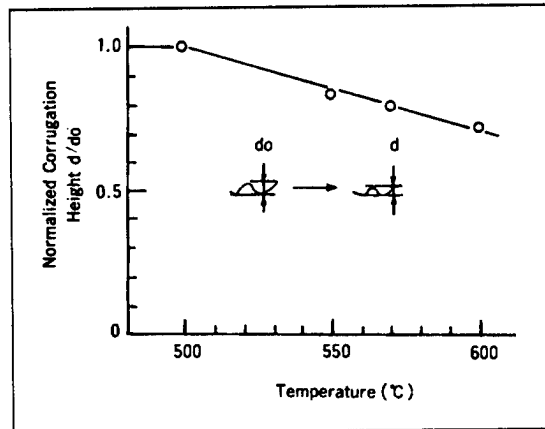Epitaxy Growth Method

Figure 6. Relationship Between Annealing Temperature
and Deformation Degree of Diffraction Gratings

In this case, too, it was found that while standing by until growth, diffraction gratings disappear. Inasmuch as the deformation of diffraction gratings is susceptible to temperature, the temperature dependency of the deformation was studied. A diffraction grating of a period of 2,000 A and a depth of 600 A was formed over a 1.2 μm composition InGaAsP optical guide layer and subjected to 40 minutes of annealing. The results of comparing the depths of the diffraction grating before and after annealing were plotted, as shown in Figure 6. It shows that as the temperature drops, the degree of deformation diminishes. At a low temperature of 500°C, diffraction grating deformation was completely suppressed. However, a temperature of

500°C is a very low temperature as compared with normal growth temperature. Consequently, when InP grew at this temperature, surface homology deteriorated. The thicker the film, the more pronounced this tendency became.

From these results, it was decided to try a two-stage growth method: InP protecting InGaAsP was once permitted to grow to a thin 0.1 μm at 500°C, then the temperature was raised to 670°C, at which an InP clad layer with good crystallinity was grown with thickness. As a result, deformation was not induced in the diffraction grating and clean burying took place with excellent homology as well. With this method, DFB lasers as low as elements of liquid phase epitaxial growth are obtained.

4. Wavelength Control Technology

4.1 Selectivity of the ± Primary Modes

It is known that because the DFB laser can provide a difference of gain between resonance modes by using the wavelength selectivity of diffraction gratings, it can obtain single longitudinal-mode oscillation. However, in actuality, the phase condition is not in agreement in terms of the Bragg wavelength, so two-mode oscillation occurs in a DFB laser which has completely eliminated the reflection factor of the edge. Since the reflection factor remains in reality, the edge phase determines in which of the ± primary modes oscillation will occur. Controlling this edge phase is difficult because the period of the diffraction grating is 0.2 μm. Normally, it is determined by chance at the time of cleavage.

Figure 7(a) shows a scattering of wavelengths calculated by the coupling wavelength formula. This indicates how far the oscillation wavelength has slipped from the Bragg wavelength.

By assuming reflection factors of 30 percent to 2 percent, the edge phase was altered 16 times, respectively, for left and right, a total of 256 times. It is clear that wavelengths are distributed on both sides with the Bragg wavelength in between. This means that even if the crystal growth technology were improved to such an extent as to control film thickness and composition properly as well as the Bragg wavelength, the wavelength is determined by probability and cannot be controlled. This is a serious problem for controlling the absolute wavelength required for coherent communication and for controlling the wavelength spacing in integrated lasers for wavelength multiple transmission.

4.2 Oscillation at the Bragg Wavelength

Methods to obtain oscillation at the Bragg wavelength include introducing a phase shift to the diffraction gratings and varying the propagation constant of the waveguide. In this case, too, the reflection factor and phase of the edge exert influence, so that reduction of the reflection factor is simultaneously required. Figure 7(b) presents an example of calculating wavelength scattering when a λ/4 shift is made. The reflection factor on both edges was set at 2 percent-2 percent, and the edge phase was
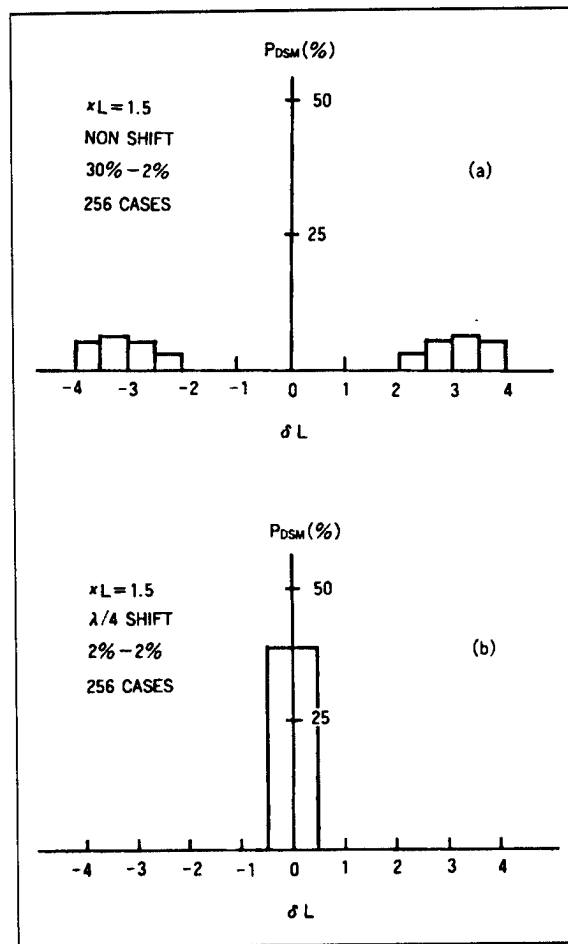
Figure 7. Examples of Calculating Wavelength Scattering
(a) In case of no phase shift
(b) In case of λ/4 phase shift

altered 256 times. It is clear that oscillation occurred roughly at the Bragg wavelength with little scattering in wavelength.

As a method of realizing this phase shift in actual devices--for example, by using both positive and negative resists to reverse the unevenness of the diffraction grating--a diffraction grating whose phase shifts spatially can be formed. Also, by changing the stripe width, the propagation constant is changed to obtain an equivalent phase shift.

By means of the latter method, which is easy to implement, we developed a DFB laser oscillating in the Bragg wavelength. This laser can be easily prepared by using a strip mask with an altered width in the center when forming an active layer stripe. The strip width is 1.3 μm. By making a width of 2.3 μm, over the 30 μm region of the center, the propagation constant is changed and an equivalent λ/4 shift is made. Through the window construction, the reflection factor of the back side edge is lowered, while the front side edge is treated with an SiN nonreflective coating film through plasma CVD. Figure 8 shows a spectrum prior to oscillation.
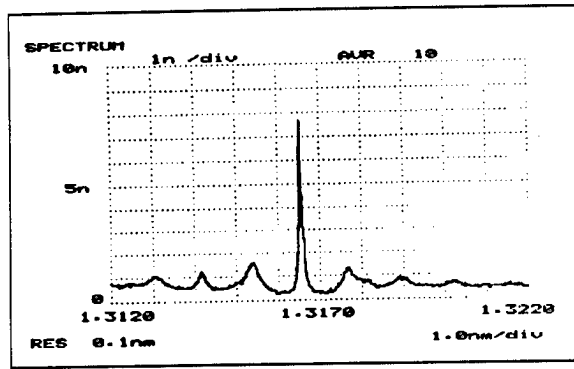
49

Figure 8. Spectrum of λ/4 Phase Shift Type
DFB Laser Prior to Oscillation

Resonance peculiar to the Bragg wavelength accompanied by valleys on both sides was confirmed. When current injection was increased, oscillation in the Bragg wavelength was obtained.

5. Wavelength Integrated DFB Lasers

The current status of the key technology of making high-performance DFB lasers has been explained. In this section, a brief explanation will be given of a comprehensive survey of this technology and the properties of the phase shift five-wavelength integrated DFB laser that was developed as the light source for high-density wavelength multiple transmission.
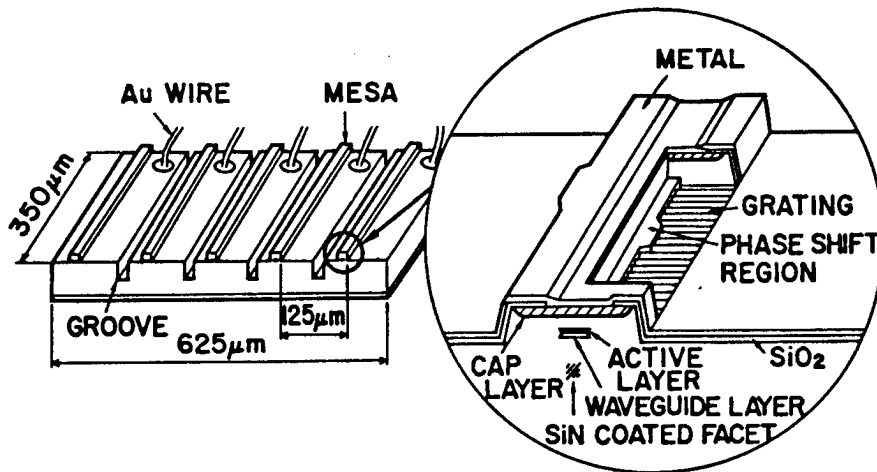

Figure 9. Structure of Five-Wavelength Integrated
DFB Laser of λ/4 Phase Shift Type

Figure 9 is a structural schematic diagram of the phase shift five-wavelength integrated DFB laser. A DFB laser buried by the mass transport method serves as the basic model. By changing the stripe width of the active layer, the propagation constant is changed to make an equivalent λ/4 shift. Also, by means of the window structure and an SiN nonreflective coating film, a low reflection factor under 0.5 percent is achieved. Between respective DFB lasers, the period of the diffraction grating is

50

varied by 9.4 A to set a wavelength space of 50 A. From spectrum observation prior to oscillation, resonance peculiar to the Bragg wavelength accompanied by valleys on both sides was confirmed in all five lasers. Upon injecting current, resonance at these Bragg wavelengths was obtained. THe current-optical output property and oscillation spectrum are illustrated, respectively, in Figures 10 and 11. The threshold current was 25 ~ 38 mA. Also, the suppression rate in the side mode was more than 30 dB. In this way, wavelength controllability was increased as a result of oscillation in the Bragg wavelength, thus making it possible to hold down the wavelength space within the range of 50 ± 5 A.
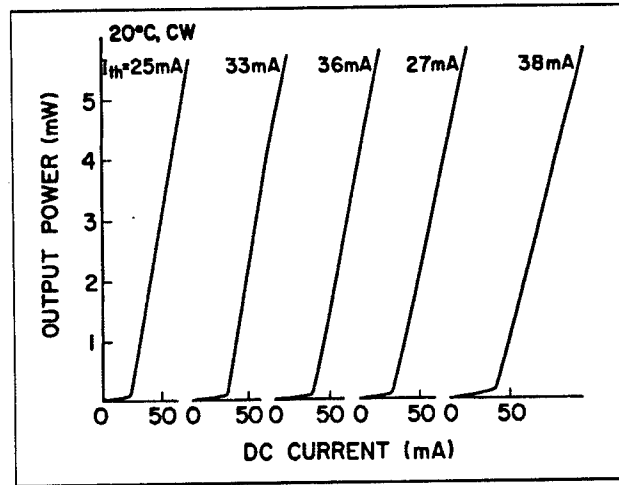

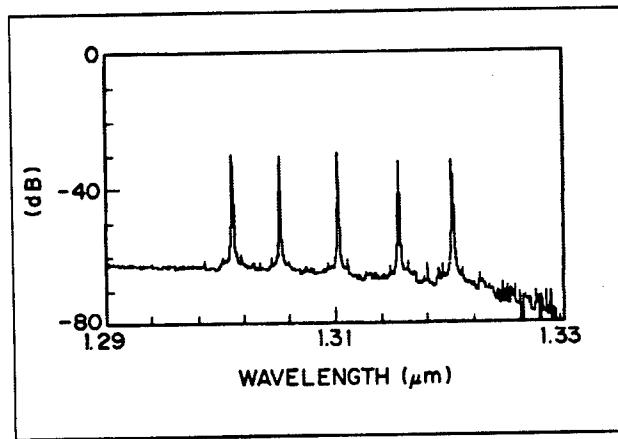Figure 10. Current-Optical Output Properties of Five-Wavelength Integrated DFB Laser of λ/4 Phase Shift Type

Figure 11. Oscillation Spectrum of Five-Wavelength Integrated DFB Laser of λ/4 Phase Shift Type

51

6. Summary

An overview has been given of the basic formation technology for long-wavelength-band DFB lasers. An even higher level formation technology will be required to obtain high performance in the control of absolute wavelength. High expectations are entertained for further advances in techniques, including the dry etching process and metal-organic vapor phase epitaxy growth.

20107/9365

Planar Type InGaAs-APD Manufacturing Process Technology

[Article by T. Torigai, NEC]

[Text] 1. Introduction

Initially, a Ge avalanche photodiode (APD) was developed as a light-receiving element for optical fiber communication over a wavelength band of 1.3 μm and 1.5 μm. However, Ge itself has limits peculiar to the material such as the large dark current and its temperature coefficient; the ratio of ionization rate of electron to hole; the noise index of the APD, close to 1; and the small absorption coefficient at 1.55 μm of ~ 10^3 cm^{-1}. Studies of InP/InGaAs heterojunction APDs having lower noise and higher speed than the Ge type have been made since the second half of the 1970s, and they are finally being put to commercial use. Making a planar type APD is a must for the development of high-reliability APDs following the example set by Si devices.

In this paper, an explanation will be given centering on the structural design and related manufacturing process technology that determine the performance of the planar type InGaAs-APD. Furthermore, trends in high-speed APDs matching the recent long-distance, large-capacity optical communication system will be covered.

2. Basic Structure and Operating Principles

The basic structure of the InP/InGaAsP heterojunction APD is shown in Figure 1(a). An n$^-$-InGaAs light-absorbing layer, n-InGaAsP intermediate layer, and n$^-$InP avalanche multiplication layer are successively formed on an n$^+$InP substrate by way of an n-InP buffer layer. The buffer layer is established to suppress the infiltration of impurities and generation of dislocation. A structure which separates the InGaAs light-absorbing layer from the InP avalanche multiplication layer to prevent the generation of tunnel dark current from InGaAs having a narrow bandgap is normally used. Because of this structure, InGaAs is controlled at a relatively low electric field, thus obtaining a low noise property.

When the APD is in operation, inverse bias voltage is impressed. Electric field distribution and band structure at that time are shown, respectively,
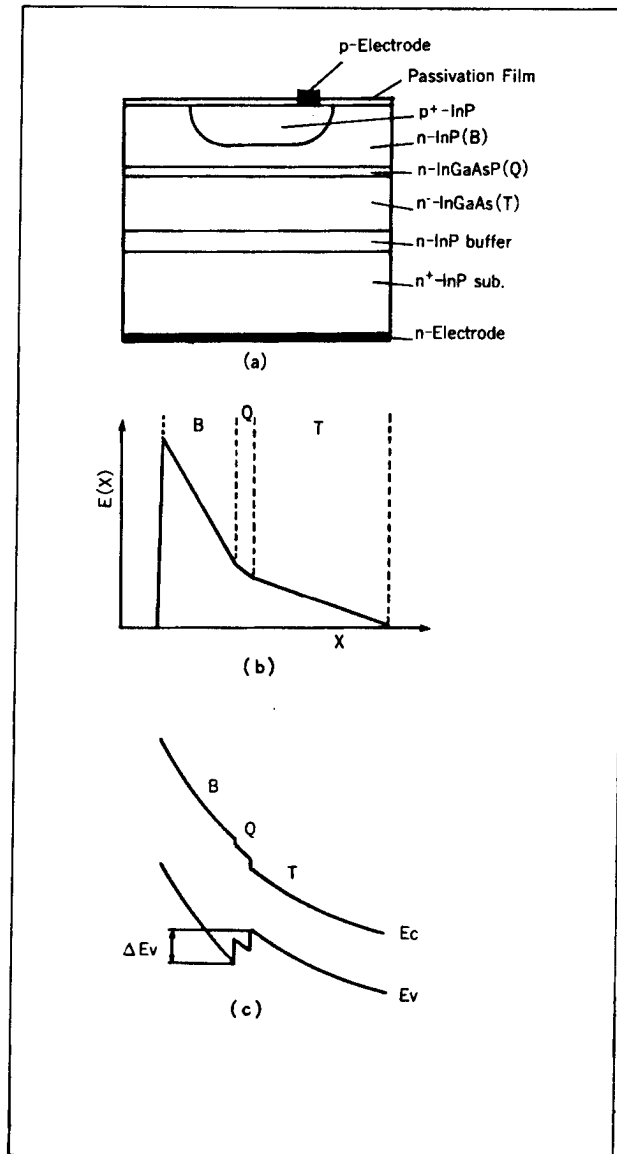
Figure 1. Basic Structure of InGaAs-APD (a), Electric
Field Distribution (b), and Schematic Diagram
of Band Structure (c)

in the schematic diagrams in Figure 1(b) and (c). Generally, implantation
of a carrier with a high ionization rate contributes to providing low noise.
Since the hole's ionization rate is larger than that of the electron in InP
which is an avalanche multiplication layer, a method of transporting only
the holes to InP out of the pairs of electron and hole which have been
generated in photoexcitation inside InGaAs is employed. The InGaAsP
intermediate layer is established to realize a high-speed response by
suppressing the accumulation of hole carriers due to band discontinuity
between InP and InGaAs.

3. Process Manufacturing Technology

3.1 Planar Structure and Crystal Growth Techniques

Planar type APDs currently in the practical stage can be divided into two types as shown in Figure 2. All have a guardring around the p^+n junction in the light-receiving region to enable uniform multiplication it the light-receiving region. Guardring formation will be explained in detail in the next subsection.
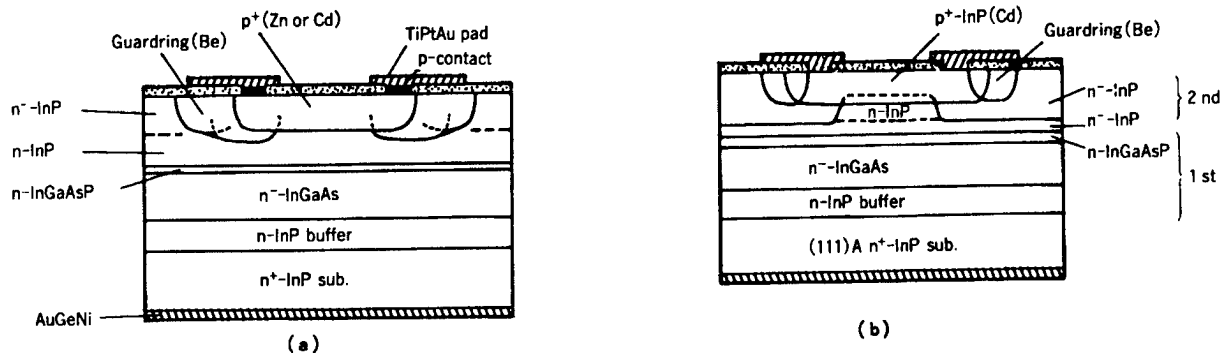

Figure 2. Sectional View of Planar Type InGaAs-APD: Structure
of selective laterally expanding guardring (PLEG)
(a) and buried structure (b)

The structure in Figure 2(a) has the advantage that the heterolayer structure can be formed in one-time epitaxial growth; it was put to practical use for the first time by hydride vapor phase epitaxial growth (VPE). In hydride VPE made up of three growth chambers, InGaAs, InGaAsP and InP are successively grown on the n^+-IP substrate with a (100) face. The growth temperature is normally 600~700°C. Advantages of hydride VPE are controllability of InGaAsP composition with greater ease than other vapor phase epitaxial growth methods and generation of excellent hetero interfaces.

The structure in Figure 2(b) requires two-time epitaxial growth because of burying the n-InP of the light-receiving section. Recent practice involves burying n^--InP in the n-InP region formed by Si ion implantation. The heterolayer structure is prepared on the (111) A surface of the InP substrate by liquid phase epitaxial growth (LPE). When manufacturing an APD using the LPE method, the (111) A surface substrate is used because of its advantages of little meltback when integrating InP on the InGaAs (P) with a narrow bandgap and the generation of a mirror free from "hill rocks."

3.2 Guardring Formation Techniques

Unlike Si or Ge-APDs, in the case of a heterojunction APD, guardring design is critical. As a result of the requirement to reduce the electric field intensity impressed on the InP/InGaAsP/InGaAs hetero interfaces in order to suppress the generation of tunnel current from InGaAs, the guardring pn junction cannot be made sufficiently deep. Also, it is difficult to obtain
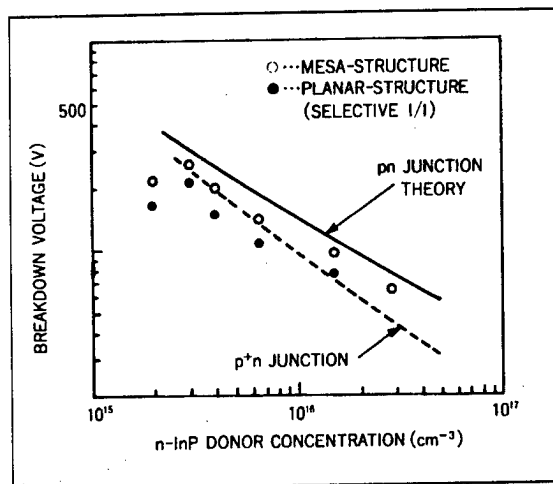
Figure 3. Breakdown Voltage of pn Junction
Formed by Be Ion Implantation

an ideal incline type pn junction to raise the breakdown voltage V_{BGR} of the guardring. The breakdown voltage for the ideal incline type pn junction is expressed by

$$V_B \simeq 60\left(\frac{E_g}{1.1}\right)^{6/5}\left(\frac{a}{3\times10^{20}}\right)^{-2/5}[V]$$

(1)

where E_g and a are, respectively, bandgap (eV) and degree of junction incline (cm^{-4}). From formula (1), the breakdown voltage should exist only in the incline, whereas, in reality, it is smaller than the value anticipated in the formula. This state is illustrated in Figure 3. This was found as a result of investigating the breakdown voltage of the pn junction formed by Be ion implantation (100 kV acceleration, 5 x 10^{13} cm^{-2} quantity of implantation) with respect to InP background concentration. The breakdown voltage of the planar structure pn junction is lower than that of the mesa structure, demonstrating that the guardring is not in an ideal incline junction and that it is affected by curvature of the junction margin. The breakdown voltage of the guardring formed by Be implantation seems to be closer to the breakdown voltage of the step type p^+n junction having curvature r_j expressed by the formula

$$V_B \simeq 60\left(\frac{E_g}{1.1}\right)^{3/2}\left(\frac{N_B}{10^{16}}\right)^{-3/4}\left\{[(n+1+\frac{r_j}{W})\,(\frac{r_j}{W})^n]^{\frac{1}{n+1}}-\frac{r_j}{W}\right\}[V]$$

(2)

where N_B is the background carrier concentration (cm^{-3}), W is the depletion layer width (cm), and n is a value from 1 to 2. To improve V_B of the pn junction formed by InP (E_g = 1.34 eV), it is necessary based on formula (2) to make N_B low and r_j large. In both structures in Figure 2(a) and (b), the guardring breakdown voltage is increased by setting up the n^--InP cap layer. In addition, in the structure in Figure 2(a), use of the selective laterally expanding guardring (PLEG) through two-time Be ion implantation has enlarged effective r_j. And by purposely forming the p^- region in the lateral direction, an effort is made to approach the ideal incline junction. By

56

including junction in the n⁻ region under the guardring, an attempt is made to improve pressure resistance in the structure shown in Figure 2 (b).

Figure 4 presents the correlation in the PLEG structure (Figure 2(a)) between guardring pressure resistance V_{BGR} and breakdown voltage V_B of the APD element. Over a range of 50 ~ 120 V, breakdown voltage is obtained with a pressure resistance difference of 10 ~ 20 V. Figure 5 shows the multiplication sensitivity distribution of the APD. Even at M = 50, uniform multiplication of the light-receiving region is made possible through the guardring effect.
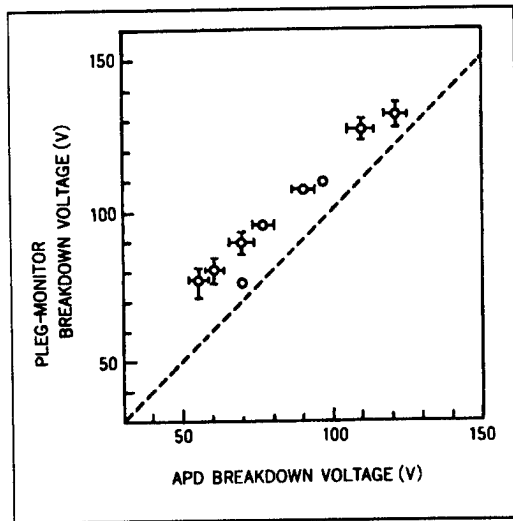

Figure 4. PLEG Structure: Correlation Between the Guardring Pressure Resistance and APD Breakdown Voltage
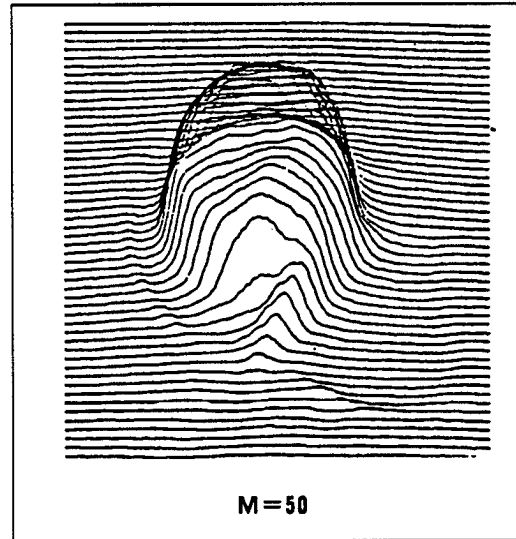

Figure 5. Multiplication Sensitivity Distribution

3.3 p⁺n Junction Formation Techniques

The p⁺n junction is normally formed by the thermal diffusion of Zn or Cd. In the case of Zn, the surface concentration can be made higher than Cd so that the ohmic resistance of the p side electrode can be lowered. Despite this advantage, because of its large diffusion rate, care must be exercised to maintain precision control of the junction position.

The p⁺n junction position is controlled to optimize electric field intensity E_I of the InP/InGaAsP/InGaAs hetero interface. The upper limit of the hetero-interface electric intensity is determined by tunnel current suppression from InGaAs. Tunnel current J_t is expressed in differential equation

$$\frac{dJ_t}{dx} = \frac{g^2 m^{*1/2} F^2(x)}{2\sqrt{2}\,\pi^3 h^2 E_g^{1/2}}\, \ell xp\left[-\frac{\pi m^* E_g^{3/2}}{2\sqrt{2}\,ghF(x)}\right] \tag{3}$$

57

where q is unit charge, m^* is effective mass, h is Planck constant, and F(x) is internal electric field. To control the tunnel current obtained from formula (3) to nA order, it is necessary to set the upper limit of E_I at 200 kV/cm.

The lower limit of the hetero-interface electric field intensity is established to relax hole accumulation on the hetero interface. However, the upper limit changes somewhat depending on how the hetero interface is formed by the crystal growth method. Generally, it is set at 120 ~ 150 kV/cm. Figure 6 presents the results of obtaining experimentally the dependence of the product of gain multiplied by bandwidth upon the hetero interface electric field intensity. It is clear that when E_I falls below 150 kV/cm, the product of G multiplied by B sharply decreases as affected by hole accumulation. But it is also seen that the higher the carrier concentration N_B of the InP avalanche multiplication layer becomes, the lower the lower limit shifts. This may be because valence band discontinuous value E_v on the hetero interface diminishes in effect, and this is in good agreement with the simulation results.
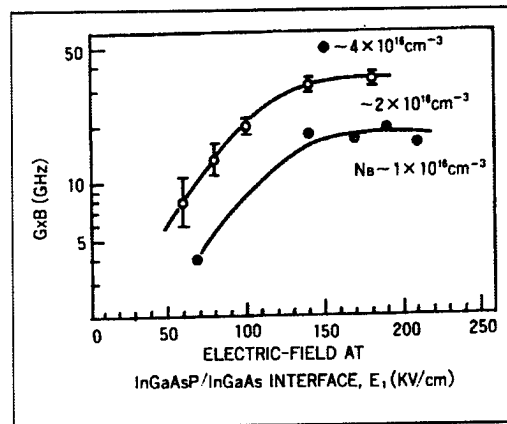

Figure 6. Dependency of Product of Gain Multiplied by Bandwidth Upon Hetero Interface Electric Field Intensity

From the above discussion, the p^+n junction position is controlled in such a way as to make the hetero interface electric field 120 ~ 200 kV/cm. If the distance from the p^+n junction front to the InGaAsP/InGaAs interface is W_B, to set E_I in the above range, W_B is controlled in approximation by the formula

$$W_B \simeq \frac{2.5 \sim 3.0 \times 10^{12}}{N_B} \text{ (cm)}$$

(4)

As is clear from formula (4), the higher the InP carrier concentration N_B becomes, the narrower the W_B tolerance limit becomes. This also means that not only position control of the p^+n junction but also high uniformity of the InP layer thickness (or the product of N_B multiplied by W_B) in the wafer are called for.

58

4. Design for High Speed

Since optical fiber communication is moving toward long distance and large capacity, high-speed APDs operating at more than Gb/s are needed. APD response R (ω) can be approximated by the formula:

$$R(\omega) = [1 + (\omega CR)^2]^{-\frac{1}{2}} \cdot [1 + (\omega \tau_{tr})^2]^{-\frac{1}{2}}$$
$$\cdot [1 + (\omega \tau_h)^2]^{-\frac{1}{2}} \cdot [1 + (\omega \tau_{av} M_0)^2]^{-\frac{1}{2}} \tag{5}$$

where CR is the CR time constant, τ_{tr} is the carrier traversing time in InGaAs, τ_h is the hole accumulation time constant on the hetero interface, τ_{av} is the real avalanche multiplication rise time, and M_0 is the DC gain (multiplication factor). Response is governed by the product of G·B in the fourth term in the high gain region, while it is controlled by the first, second, and third terms. In other words, to meet the high-speed demand, not only enlarging the product of G multiplied by B but also expanding the band in the low gain region are required. Hence, APDs have been developed in which the light-receiving diameter is reduced to 30 μm in order to decrease capacity C.
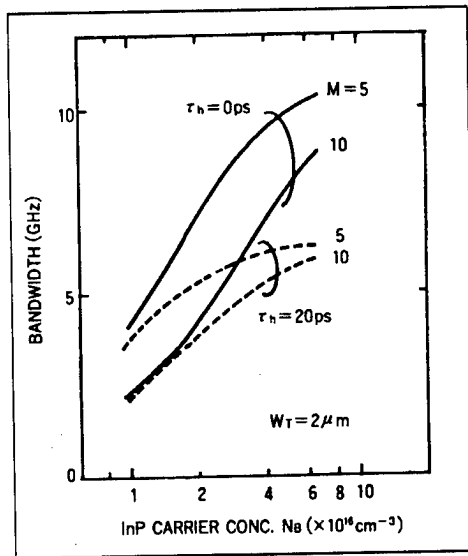

Figure 7. Dependency of Band Upon InP Carrier Concentration
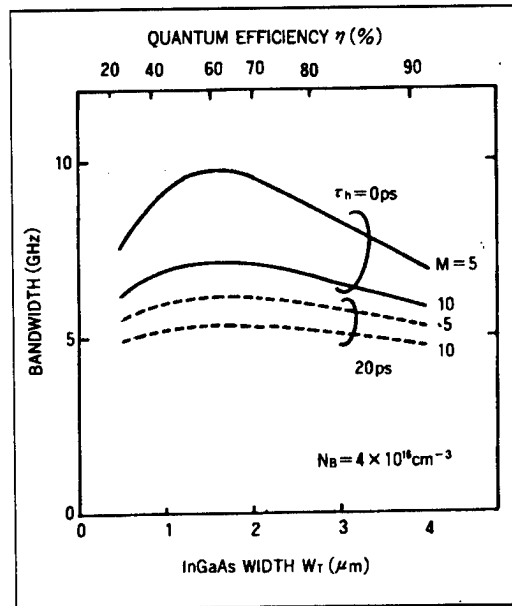

Figure 8. Dependency of Band Upon InGaAs Depletion Layer Width

Figures 7 and 8 present the dependence of the band obtained from formula (5) upon the INP carrier concentration (N_B) and upon the InGaAs depletion layer width (W_T). Calculations are performed when M = 5 and 10, and τ_h = 0 and 20 ps. From Figure 7 it is clear that the higher N_B is made, the more the band expands as the avalanche rise time is shortened, but if τ_h is about 20 ps, the band will reach saturation with $N_B > 4 \times 10^{16}$ cm^{-3}. Figure 8 shows

the presence of the optimum InGaAs layer thickness to obtain the maximum band. With $N_B = 4 \times 10^{16}$ cm^{-3}, if W_T is set to equal 1.5 ~ 2.9 μm, a band of 10 GHz can be expected. At $W_T < 1.5$ μm, response is governed by capacity, and at $W_T > 2$ μm, it is governed by the traversing time. From Figure 8, it is seen that τ_h has substantial effect on the band. To obtain a band in excess of 5 GHz, it is necessary to create a situation wherein no hole accumulation exists on the hetero interface. This calls for connecting gently the valence band discontinuity (ΔE_V ~ 0.4 eV) between InP and InGaAs. In APDs (mesa type only) having a three-stage InGaAsP intermediate layer introduced by the chemical beam epitaxy process (CBE), a maximum band of 8 GHz is obtained. In the planar structure, through the two-stage InGaAsP intermediate layer, a maximum band of 7.5 GHz and the product of G•B 75 GHz are obtained.

5. Conclusion

Years of R&D on the planar type InGaAs-APD have borne fruit, and the practical stage has been reached. An overview of the pn junction forming technology including the forming techniques of heterolayer structures that are a key to realizing the planar structure and guardrings have been provided. Currently active is the development of high-speed APDs operating at over GB/s, and APDs having the product of G•B of 20 ~ 30 GHz are now commercially available. As a result of the appearance of planar type APDs with a band in excess of 5 GHz in the research stage, 80-km nonrelay transmission at 10 GB/s has been realized.

20107/9365

Bistable Optical Switching Element Manufacturing Technology

[Article by K. Kojima, et al., Mitsubishi Electric Corp.]

[Text] 1. Introduction

With the rapid development of optical technology, many new optical systems
such as optical fiber communication, compact disks, optical disks, and
optical measuring instruments have been developed. Today, research on
optical computers is actively pursued the world over. Optical computers
purport to handle massive volumes of data processing at very high speed by
using the super parallel property of light. For example, great expectations
are entertained for their application to large-scale matrix operation, real-
time image processing, and neuro computers. A number of proposals on
optical computer systems have been made. As regards the actual hardware,
it remains small scale with insufficient speed. Lagging development of
devices is cited as the main reason for this state. For realization of
optical computers, the development of many key devices is necessary. Above
all, the most critical device is the optical switch element (called the
optical theoretical element or optical threshold element). The properties
which the optical switch element should have include:

    (1) Easy to be made into one- and two-dimensional alleys
    (2) High-speed operation
    (3) Large optical output
    (4) Large ON/OFF ratio
    (5) Switching at very little optical input
    (6) Not sensitive to input light wavelength

There are several types of optical switch elements. Bistable semiconductor
laser type optical switch elements using a saturable absorber possess
properties (3) to (6). However, making these conventional optical switch
elements into two-dimensional alleys is difficult, so their speed is not
very high.

The surface light-emitting bistable MQW (multiple quantum well)-DBR
(distributed Bragg reflector) laser type optical switch which we recently
developed [at Mitsubishi Electric], has such characteristics as superhigh
speed because of the MQW structure which permits light input and output in

the vertical direction to the substrate and is suitable for being made into two-dimensional alleys. In this paper, the operating principles, manufacturing technology, switching properties, and future outlook for this element will be discussed.

2. Operating Principles

The basic structure of a bistable semiconductor laser type optical switch element is shown in Figure 1(a), and its current-optical output properties in Figure 1(b). Since no current is injected into the absorbing region (depending on the field, very small current is run with an electrode different from the gain region), saturable absorption properties are exhibited. In other words, when the light intensity is small, light is absorbed with intensity, while light absorption weakens when the light intensity is high. When power is implanted into the gain region of such an element, as shown in the illustration, optical output gradually increases. But as a result of large absorption in the absorption region, oscillation does not start easily. At a certain current (I_1), suddenly oscillation begins. After oscillation, absorption is small because of intensive light, and oscillation is maintained until the current is reduced below the level of I_2.
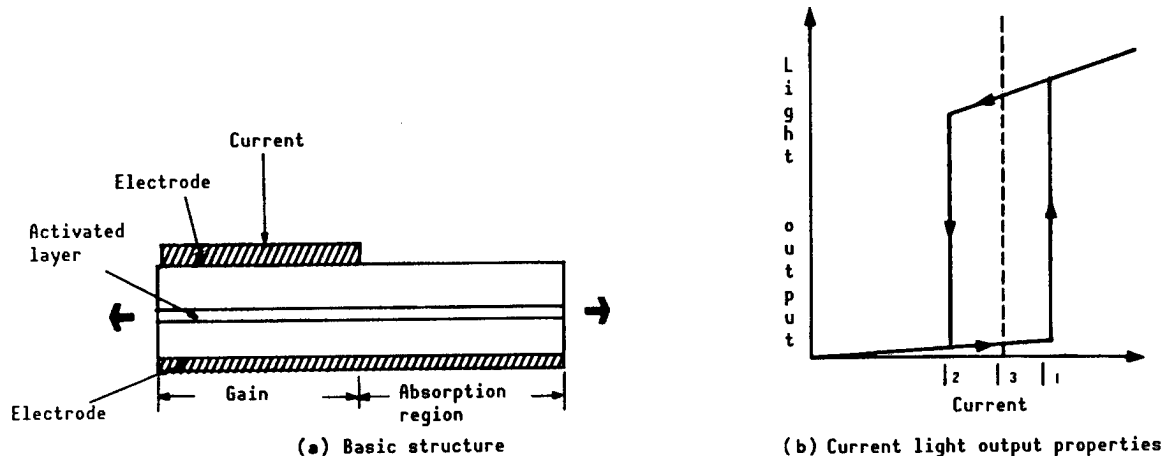

Figure 1. Optical Switch Element of Bistable Semiconductor Laser Type

In this way, there is a record property between current and the optical output property. If a bias current is run at I_3, because of its past record, the two states of ON and OFF can be adopted; this element, called an optical bistable element, has a memory function. Also, when light with an intensity over a certain level enters from the outside, the OFF state can change to the ON state, so this can be used as an optical threshold element.

3. Manufacturing Technology

In the element structure, shown in Figure 2, the gain region functions to multiply light in the same way as a conventional semiconductor laser, and
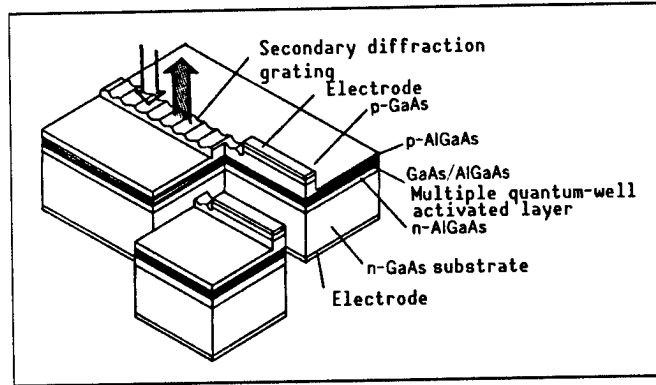
Figure 2. Schematic of Bistable Light Switch Element
of Surface Light Emitting Type

the absorbing region simultaneously performs the three functions of the saturable absorber, Bragg reflection mirror and grating coupler. In the Bragg reflection mirror, the reflection factor is provided with wavelength selectivity through the action of a diffraction grating. The grating coupler is a coupler that takes part of the light vertically to the substrate (surface light emitting) by a secondary diffraction grating. Also, for enclosing transverse direction light and current, the ridge waveguide structure is used. A major characteristic of this element is that it can be manufactured by one-time crystal growth. Therefore, it is expected that massive volumes of uniform quality elements can be manufactured with high yield in the future.

Figure 3 shows the manufacturing process. An MQW active layer consisting of the n-GaAs buffer layer (0.2 μm), an n-$Al_{0.35}Ga_{0.65}As$ clad layer (1.5 μm), a five-layer undoped GaAs well layer (10 nm) and a four-layer undoped $Al_{0.20}Ga_{0.80}As$ barrier layer (5 nm), as well as a p-$Al_{0.35}Ga_{0.65}As$ clad layer (1.5 μm) and a p^+-GaAs contact layer (0.5 μm), are successively grown on the 2-inch n-GaAs substrate by the MBE (molecular beam epitaxy) process.

In Figure 3(a), the wafer is subjected to careful etching by the use of a resist mask 4 μm x 300 μm so that the p-clad layer of 0.2-0.3 μm remains, and ridges are formed in the gain region. Ridges are formed in the (011) direction of the substrate.

Next, as shown in Figure 3(b), secondary diffraction gratings are formed over the entire wafer except on the ridges in the gain region. The diffraction grating is made as the period structure of the photoresist prepared by the two-luminous flux interference exposure method (also called the holographic exposure method) using an He-Cd laser (wavelength 325 nm) is transcribed to the wafer by chemical etching. The period of this diffraction grating is 257.5 nm, designed to be 20 or 30 nm shorter than the gain peak wavelength which was measured in advance. In measuring this gain peak wavelength, the effective refractive index of the absorbing region obtained by calculation is used. Detuning to this short wavelength side is highly effective for increasing the record loop width and achieving high-speed switching.
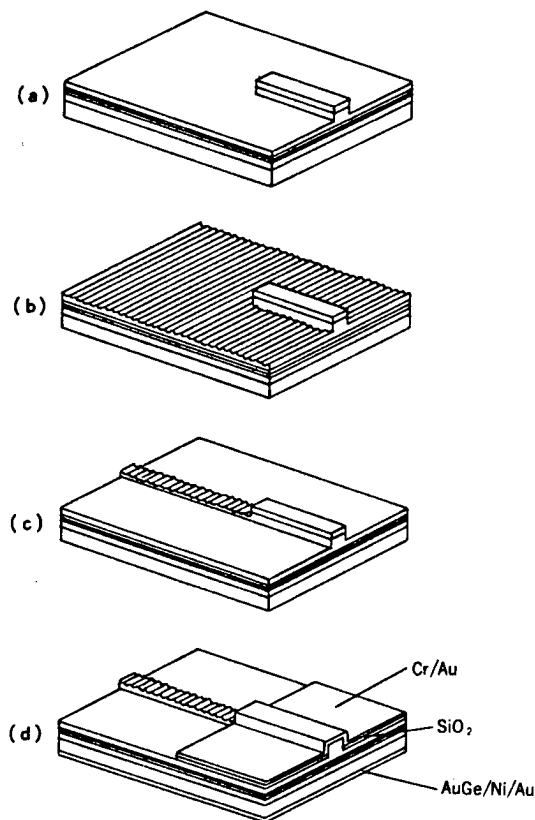
63

Figure 3. Fabrication Process

Next, etching is performed using a 4 μm stripe mask, as shown in
Figure 3(c), and ridges are formed through the gain region and DBR region.
After this process, an SiO_2 insulation film is deposited over the entire
surface of the wafer, and a window opening for current injection is formed
on the ridges in the gain region.

As shown in Figure 3(d), Cr/Au is evaporated and Cr-Au on the absorbing
region is removed for taking out surface light-emitting components and
injection of external light. The final step consists of grinding the wafer
to as thin as 80 ~ 100 μm and evaporating AuGe/Ni/Au on its reverse side.

A wafer finished in this way is subjected to cutting by cleavage in such a
way that each tip has a gain region of 150 μm and an absorbing region of
300 μm; then, each is mounted on the Cu mount by way of an Si submount and
Ag block. The cleavage face of the gain region side is treated with
dielectric multifilm coating of a high reflection factor to increase the
surface light-emitting output, and the element is completed.

One key point in the manufacture of this element lies in the distance
between the diffraction grating and the MQW active layer. Figure 4 presents
the result of calculating coupling efficiency η of the gain region and the
absorbing region and coupling constant κ which is a parameter to show the
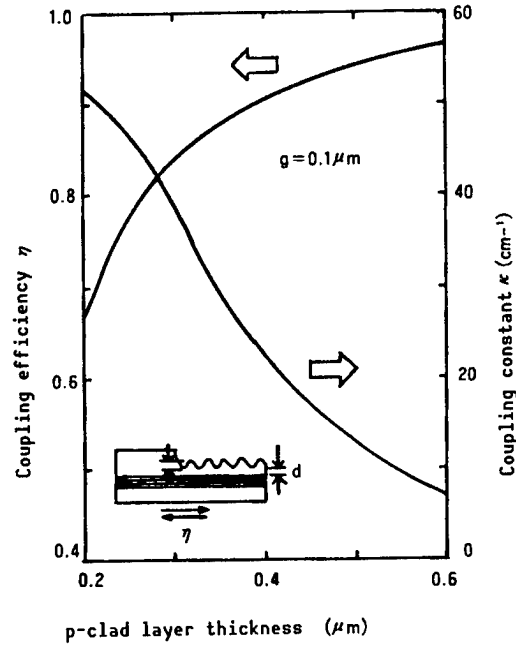
Figure 4. P Clad Layer Thickness Dependency of Coupling
Efficiency and Coupling Constant

diffraction grating strength as a function of distance d between the
diffraction grating and the MQW active layer. When d is large, κ becomes
small. When d is small, η becomes small. Therefore, it is necessary to
control d with precision to some degree. To relax this requirement, it is
necessary to utilize a so-called SCH (separate confinement heterostructure)
by setting up an optical guide layer over and under the active layer so that
the value of d will not appreciably affect the electric field distribution
in the vertical direction.

4. Switching Properties

Photograph 1 [not reproduced] shows the current-optical output property.
A threshold current of 37 mA and a surface light-emitting output of over
2 mW are obtained. Equally important is the exceedingly large ON/OFF ratio,
which is more than 50:1. This cannot be obtained in devices such as
nonlinear ETALON and SEED. It is a major characteristic of the bistable
semiconductor laser type optical switch element, a critical point in
building it in an actual system.

Figure 5 shows the startup property when pulse current is applied. The rise
time was a very high-speed 12 ps (1 ps = 10^{-12} seconds), and the rise time
was a very high-speed 60 ps. Conventional bistable semiconductor laser type
optical switch elements take about 200 ps for both rise and breaking time.
This high-speed property is due to the use of the MQW structure and detuning
to the short wavelength side.

Next, switching time by optical input, which is very critical in application
to optical computers, was measured. While running slightly lower current
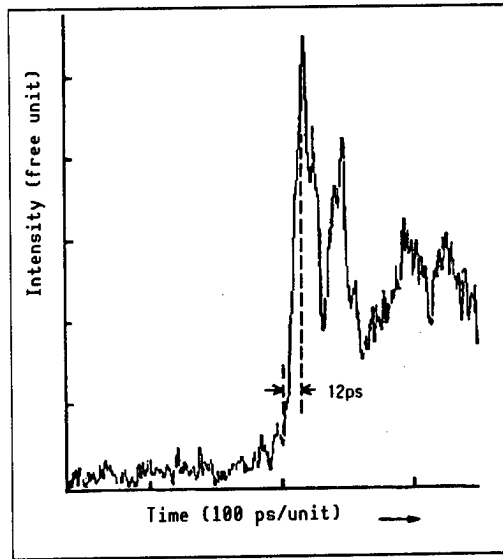
65

Figure 5. Switching Properties Through Current Trigger

to the optical switch element than the threshold current, external light was injected from the upper part of the element's absorbing region to decrease absorption, and the switch was made from the OFF state to the ON state.
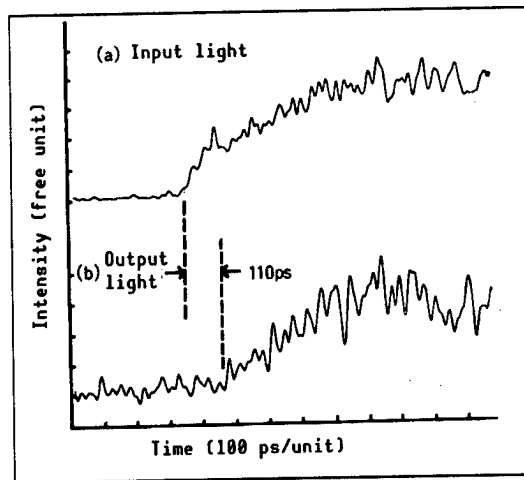

Figure 6. Switching Properties Through Semiconductor
Laser Input Light

Figure 6 presents input light and output light measured by a streak camera when switching was performed by an external semiconductor laser light (wavelength 830 nm). It is clear that the optical switching element performs switching with a very small time lag of about 100 ps to the input light. The minimum switching power when the semiconductor laser was used for switching was 2 mW, and the switching energy was 10 pJ. At present, the greater part of the light injected from the outside is not effectively used for switching. Through optical system improvement and optimization of the element structure, high-speed switching could be performed with lower power.

66

To measure even higher speed response, injecting Ar laser light from the outside was tried. Photograph 2 [not reproduced] shows the measurement results giving the response of optical switching elements. The time lag and rise time with respect to input light were under the limits of this measurement system (20 ~ 30 ps). Thus, it is clear that this element responds to external light input with very high speed.

5. Future Outlook

The characteristics of this element are roughly threefold. The first is the capacity to perform high-speed operation. The second is that this element, being a surface-light-emitting type, makes it possible for light to enter or leave in the vertical direction to the substrate. This enables integration of a large number of elements over the same substrate, a feature that lends itself to optical computers where the objective is two-dimensional optical data processing. The third is that these switching properties are hardly dependent on the wavelength and angle of input light, signifying a greater degree of freedom when building the elements in optical computers.
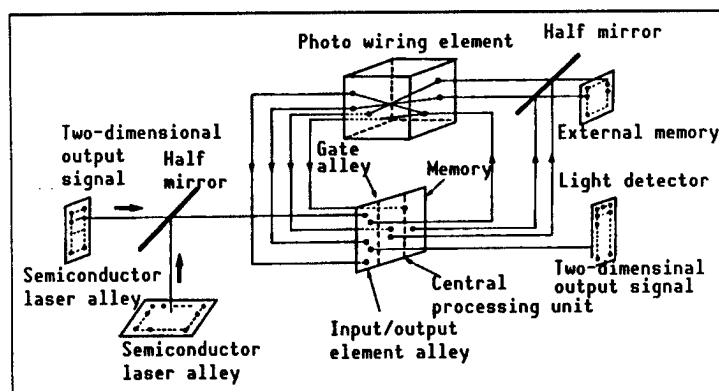

Figure 7. Schematic Diagram of Optical Computer

Figure 7 is an example of an optical computer schematic diagram. The input/output element alley, central processing unit, and memory perform control and operation by the light entering vertical to the substrate and, in turn, function to output light vertically from the substrate. Hence, currently developed optical switching elements can be put to effective use here. For realizing optical computers, the development of many new devices such as that shown in Figure 7 is required. Among such devices, the optical switching element is the most critical device.

The above-mentioned characteristics are contained in the optical switching element currently developed. To build it in an actual system, it must meet the following requirements: operation at smaller light input, less power consumption, and smaller element dimensions to realize large-scale two-dimensional alleys. These problems need to be solved in the future.

As the foregoing discussion indicates, the optical switching element is indispensable to the realization of an optical computer. The development of this new type of optical switching element is a positive step forward.

20107/9365

68

R&D Trends of Optical Isolator in Optical Communications

[Article by S. Takeda, Hitachi Metals, Ltd.]

[Text] 1. Introduction

With the progress of optical communications technology of late, work is proceeding rapidly to provide optical communications systems with high-speed, large-capacity, and long-distance capability. To realize this, reduction of the line width of the laser diode (LD) and improvement of stability are required. The former may be resolved, as there is a possibility of producing a line width of some 10 MHz with the appearance of the DFB laser. Accordingly, R&D on optical communications systems such as ultrahigh-speed, coherent transmission using semiconductor lasers has accelerated. The question posed here is the second problem, stability. since the LD's oscillation wavelength fluctuates sensitively according to temperature and bias current, auxiliary equipment such as LD chip temperature control and a super stabilizing power source are required. In addition, unstable oscillation of the LD due to "returning light" from various parts inserted in the transmission lines of the optical transmission system poses a serious problem in terms of system configuration. Prevention of this calls for high-performance optical isolators.

The device called an "isolator" is already indispensable in microwave communication and is widely used today. One of the authors was engaged in the development of isolators for microwave and is currently at work developing optical isolators. A comparison of the two shows a very close similarity in terms of necessity from the system side. Another similarity is that the physical phenomenon to be used in microwave is the Faraday effect due to ferromagnetic resonance, while the physical phenomenon to be used in light is the Faraday effect due to electron transition peculiar to the magnetic substance.

Recently, great progress has been made in R&D on optical isolators, and considerable achievements have been accumulated. Classifying them to put them in order here is worthwhile. In this paper, R&D trends in optical isolators used for optical communication are outlined from such a standpoint.

2. Properties Required of Optical Isolators

The basic function of the optical isolator is, as shown in Figure 1, to transmit the light coming from the LD to transmission lines such as optical fibers scarcely with loss, and, on the other hand, to shut off almost completely the reflective light coming from the fibers. The former transmission loss is called insertion loss, and the latter isolation loss. In practice, the smaller the former ($\leq$1 dB), the better, while the larger the latter ($\geq$30 dB or 60 dB), the better. In addition, the following are required from the practical standpoint.
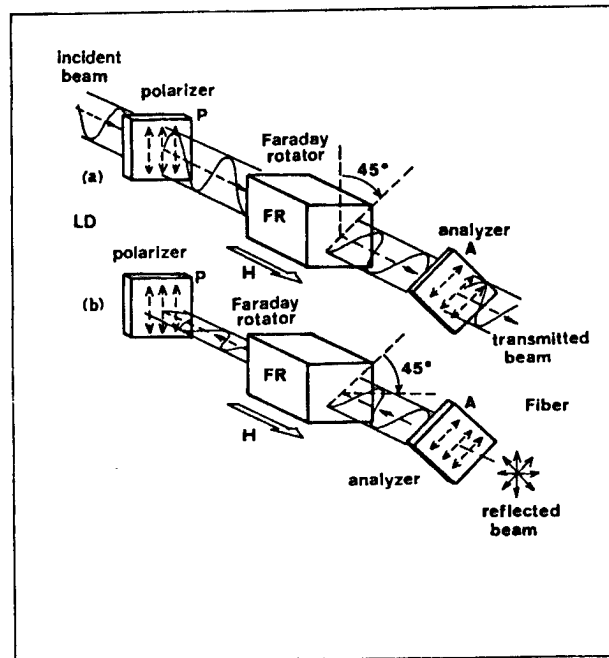

Figure 1. Diagram Showing Principles of Optical Isolator
(a) in Regular Sequence (b) in Reverse Sequence

1) Wider band

To cope with future technical trends, such as wavelength multiple and frequency multiple communication systems, optical isolator properties should be secured over as extensive a range of wavelength as possible. Also, in reality, if the band is specified as the 1.3 μm band or 1.55 μm band, it is necessary to have a minimum bandwidth ($\pm$10 ~ 20 nm) to cope with the scattering of the LD's oscillation wavelength.

2) Temperature stability

Generally, isolator properties should not deteriorate over the temperature range of -20° to 60°C required for communication equipment. The materials used for the isolator are oxide magnetic materials, so Faraday rotation θ_F (°/cm) changes with temperature. Accordingly, the device properties also change. The question is how to resolve this in terms of design or material properties.

70

3) Matching With Other Optical Circuits

Depending on the means used for connection of the optical circuit to which the optical isolator is linked--space propagation, fiber propagation, waveguide or LD module--the optical isolator's structure varies greatly. It is necessary to select the optimum structure for the optical isolator in accordance with the optical circuit to which it is to be connected.

3. Classification of Optical Isolators

Optical isolators, as in Table 1, are classified in terms of the type of optical circuitry to which they are to be connected.

Table 1.   Classificiation of Optical Isolators

Microoptic circuit	Polarizer analyzer type	Spatial propagation type LD module type Optical fiber type
	Wedge shape prism type	LD module type Optical fiber type
Optical waveguide	Mode selector type Nonreversible phase shifter type	

4. Microoptics Type Optical Isolators

All optical isolators commercially available today belong to this type.

4.1 Polarizer Analyzer Type

This type is the most common type directly using the Faraday effect. As shown in Figure 2, this is composed of a polarizer, a Faraday rotator, and an analyzer. The following three types of this simple structure have been reported:
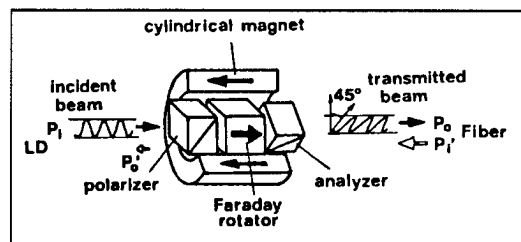

Figure 2.   Microoptics Circuit: Basic Structure of Polarizer Analyzer Type Optical Isolator

(1) Spatial propagation type

The light to be treated is the light propagating in space. In this case, it has the same structure as that shown in Figure 2. The aim is for the

71

optical isolator to have as much effective area as possible. This type is mainly used in laboratories for optical experiments.

(2) LD module type

An optical isolator such as that shown in Figure 2 is set up in very close proximity to an LD so that they become one unit or LD module. It is what is known as an LD module with an optical isolator. In this case, it is most effective to prevent the LD from suffering disturbance. As a device, this type has reached completion and is evaluated as such.

(3) Optical fiber type

As shown in Figure 3, in this type of structure, the optical isolator is directly attached on the middle of the fiber. A micro isolator has been proposed for this. In this case, the critical problem is the making of a micropolarizer analyzer that can be directly mounted on the fiber. To solve this, Lamipol with a multiple layer film structure of metal film and dielectric film is under consideration.
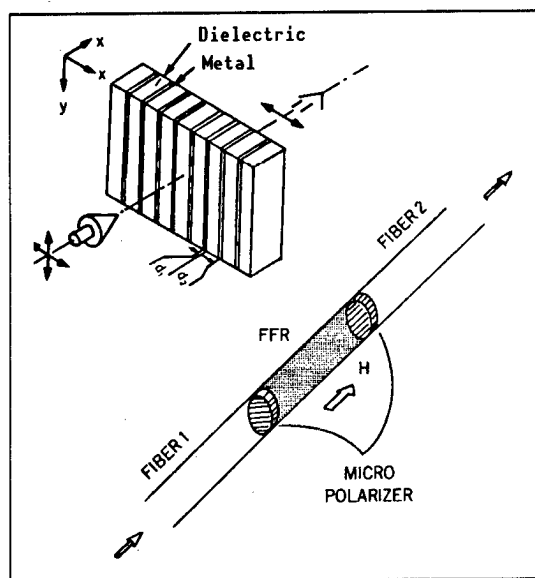

Figure 3. Optical Fiber Type Optical Isolator

The problems of this polarizer analyzer type are as follows:

1) Since insertion loss has polarization dependency of the incident light, the polarization direction of the incident light from LD, etc., and the polarizer direction must be accurately aligned.

2) It is difficult to make it applicable for a wider band and to achieve temperature stability.

This is because Faraday rotation θ_F (°/cm) changes wavelength and temperature as shown in Figures 4 and 5, while reverse loss, accordingly, changes as
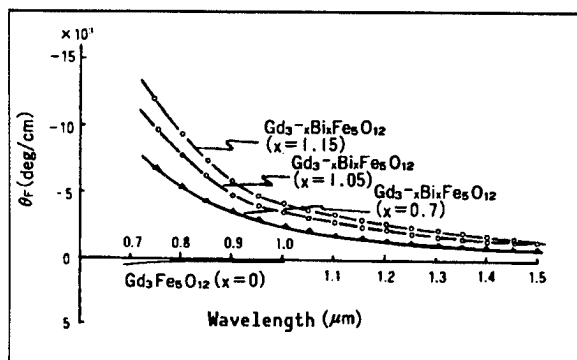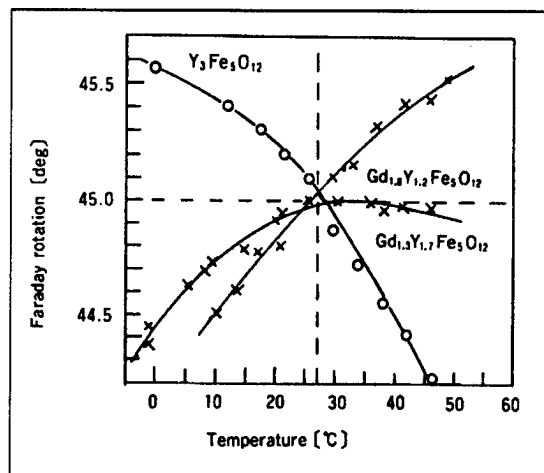
72

Figure 4.   Wavelength Properties of   Figure 5.   Temperature Properties of
            Faraday Rotation of   Faraday Rotation of
            Various Garnets   Various Garnets

$-10\log \sin^2 (\theta_{F0} - O_F)$.   Studies using Gd-YIG and $Yb_3Fe_5O_{12}$ to improve this have been reported.   Nevertheless, when using this type over a wide practical range in a service temperature range of $-20 \sim 60°C$ at $0.8 \sim 1.5$ μm, even more stringent performance requirements obtain.

It is judged that an LD module type of this system will be in the mainstream of optical communication from now on.   Also, the optical fiber type is likely to be used for special applications such as instrumentation.

4.2   Wedge Shape Prism Type

The principle of this system utilizes the nonreversible complex refractivity of the magnetic material.   In other words, a polarizer analyzer is not necessary because of the use of nonreversible shift of the ordinary light and extraordinary light from the optical axis.   In this case, the wedge shape prism and the coupling lens form the principal components.   The advantages of this system are: insertion loss has no polarization dependency of the incident light; and because extinction of the light is made in such a way as to utilize the slant of the optical axis, the phenomenon makes sharp change.   In particular, the latter is digital, in contrast to the analog extinction of the light in the polarizer analyzer system.   Therefore, its characteristic is its capacity to withstand temperature change and wavelength change.

The following two types are reported for this system:

(1)   Optical fiber type

In this structure, optical fibers (pigtails) are attached to both ends of the optical isolator, as shown in Figure 6.   For the wedge shape complex refraction prism type, a single crystal of rutile is used.   To increase the effect of optical axis shift, a globular coupling lens is used for one end.
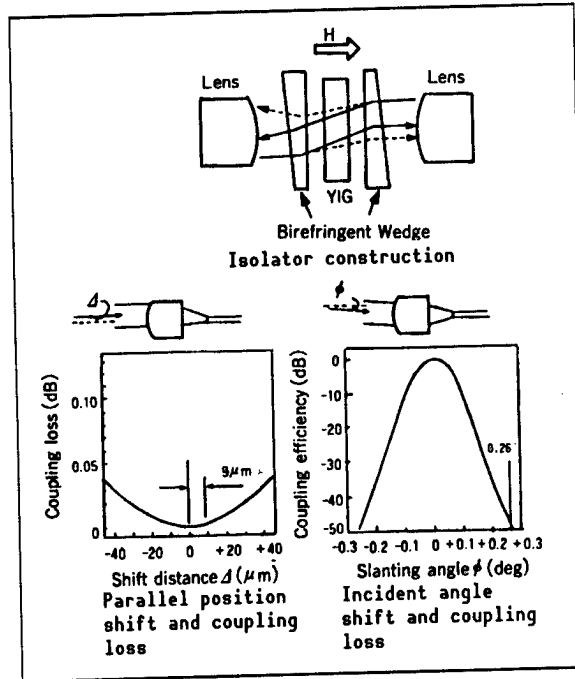
73

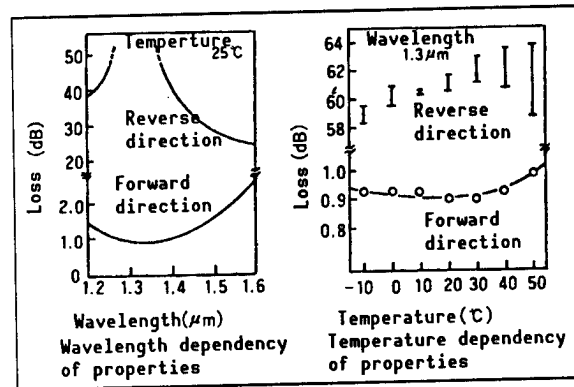Figure 6. Principle of Wedge Shape Prism Type Optical Isolator

Figure 7. Properties of Wedge Shape Prism Type Two-Step Optical Isolator

In performance, this is a so-called two-step optical isolator with two isolators connected. As Figure 7 shows, superior properties of a reverse direction loss of over 25 dB at a temperature of 25°C with λ = 1.2 ~ 1.6 μm and a reverse loss of over 55 dB over a temperature range of -20 ~ 50°C at λ = 1.3 μm are reported. In this case, no special material properties are needed. All that is required is YIG single crystals. In principle, the materials listed in Table 3 are all used for Faraday rotation.

(2) LD module type

The principle of this type is identical to that of the fiber type. Since this is set up close to the LD, as shown in Figure 8, miniaturization has been suggested. In performance, a reverse loss of 35 dB and an insertion loss of 0.24 dB at 18 ~ 55°C have been reported.

Table 2. Main Paramagnetic Substances Used for Optical Isolator

Materials	Properties	Wavelength (μm)	(Velte) constant (10^{-3}deg/Oe·cm)	Performance index (deg/dB)
FR-2	Glass	0.633	1.2	
FR-5	"	0.633	1.2	
	"	1.06	4.0	
SF-6	"	1.06	0.5	
ZnSe	Single crystal	0.82	3.4	
BGO	"	0.85	3.2	
BSO	"	0.633	3.67	
	"	0.87	1.7	
	"	1.15	0.93	
CdMnTe	"	0.62	150	460(at 3000 G)

Table 3. Main Ferromagnetic Substances Used for Optical Isolator

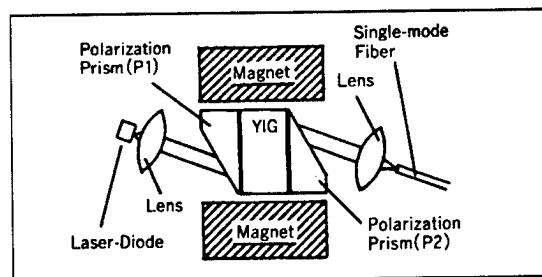| Materials	Manufacturing methods	Wavelength (μm)	Performance index (deg/dB)
YIG	Flux method	1.3	300
YIG	"	0.8	1.5
GdBiIG	"	"	44
YIG	TSFZ method	"	81
(GaY) (FeV)G	Grain growth	1.55	96
(GdY)IG	LPE	1.3	230
(GdBi) (FeAlGa)G	LPE	"	270
(YGdBi) (FeGa)G	LPE	0.8	26
(GdBi) (FeGaAl)G	LPE	"	27
(CaGdBi) (FeAlGa)G	LPE	"	30
$Bi_3Fe_5O_{12}$	LPE	"	55

Figure 8. Structure of Wedge Shape Prism Type
(LD Module Type) Optical Isolator

Conceivable problems in regard to this type are the requirements for high processing precision, including the wedge shape prism, YIG and lens, as well as high assembly precision. On the other hand, the advantage is that if these requirements are sufficiently met, superb stability, as mentioned above, can be obtained.

5. Waveguide Type Optical Isolator

This purpose of the waveguide type optical isolator is to cope with the optical integrated circuit. Mostly, this type is still at the idea stage on the R&D level; isolator property evaluation reports are hardly available.

5.1 Mode Selector Type

This system has been proposed as a waveguide type since the early days of isolator development. As shown in Figure 9, in addition to a section generating Faraday rotation (advancing the direction of light parallel to the direction of magnetization), its structure needs a mode transformation section (direction of magnetization slanted). In the case of the direction of easy flow, the mode transformation section functions to correct a mode slanted at 45° due to Faraday rotation to the TE wave, which is the propagation mode on the transmitted edge. In the case of the reverse direction, it functions to correct the mode to the TM wave, and all is absorbed by the input side mode selector. The mode selector consists of metallic films such as Al, Au, Ag, etc., and is equivalent to a polarizer analyzer. Currently, YIG type film on a GGG substrate is in the mainstream among waveguides. For film materials, YIG, Bi-YIG, Bi-Gd-YIG, etc., are prepared by the sputter method and are being reviewed. In principle, this method is equivalent to a polarizer analyzer type of microoptics circuit. As a result, the method of extinction of light is analog, so problems will probably exist in terms of wavelength dependency and temperature properties. It should be noted, however, that setting up the Faraday rotation section in proximity to the mode transformation section, as shown in Figure 9, has not met success yet. Current R&D efforts are focused on the manufacture of the mode transformation section.
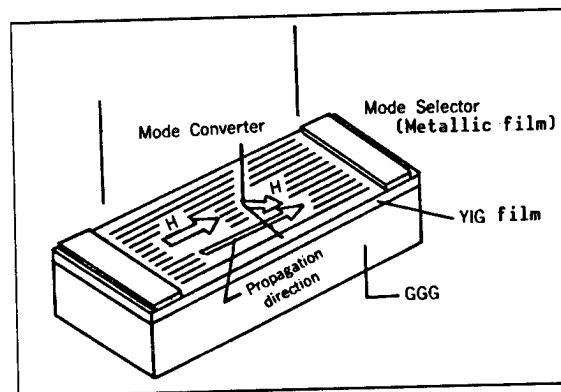

Figure 9. Structure of Mode Selector Type Optical Isolator

5.2 Nonreversible Phase Shifter Type

This system makes use of nonreversibility of the propagation mode by utilizing a nonreversible phase shifter, as shown in Figure 10. In this case, there is no section equivalent to the polarizer analyzer. The nonreversible phase shifter is attached to the waveguide with two Y branches. In the direction of easy flow, it assumes the even mode and
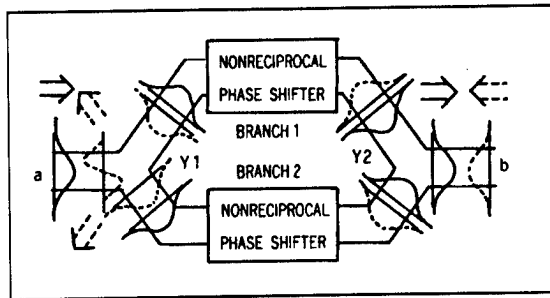
Figure 10. Principle of Nonreversible Phase Shifter Optical Isolator

propagation mode. In the case of reverse direction, the phase shifts to the odd mode and the light is radiated to outside the system. This is equivalent to a wedge shape prism type, the basic principle of which is the nonreversible shift of the optical axis. However, the perfect odd mode does not exist and some even mode is present, so analog changes in the extinction of light will probably occur. Although overall evaluation of this device has not been made, like the polarizer analyzer type, wavelength dependency and temperature dependency will probably pose a problem.

At present, the way to manufacture the nonreversible phase shifter is the subject of research. Under consideration are GGG single crystal for the substrate, LPE film of Bi-YIG for the nonreversible waveguide, ZnTe for the rib type waveguide, SiO_2 film, etc. For the method of impressing the magnetic field, the supply of current via a micropattern is being proposed.

6. Main Materials Used for Optical Isolator

The optical isolator is a nonreversible element using the Faraday effect. There are two types of Faraday effect: the Faraday effect of paramagnetic material and that of ferromagnetic material. The former is mainly glass, and the latter chiefly garnet crystals. These materials are summarized in Tables 2 and 3.

Glass and garnet materials have about 1 μm as the boundary. Glass is used for shorter wavelengths than this, while garnet is used for longer wavelengths. Note that glass has a small Faraday rotation angle per unit length. To obtain a Faraday rotation angle of 45°, glass must be a few centimeters long under a magnetic field of 3,000 Oe. In the case of paramagnetism, stronger magnetic field intensity will increase the Faraday rotation angle, so research is being conducted to obtain a strong magnetic field by devising magnetic circuitry. However, even this is insufficient for miniaturization. The appearance of materials having a large Faraday rotation at a wavelength of under 1 μm with small loss is awaited.

For optical communication over a band of 1.3 μm, garnet materials are mostly used. the major problem in this case is to determine which is better--LPE film or bulk crystal. This is a controversial subject. The characteristics of each are explained below:

77

1) Since it is difficult to manufacture stably an LPE film of over 200 or 300 μm, the Faraday rotation tends to be scattered. Consequently, film thickness needs to be controlled precisely. But because many chips can be obtained at one time, once the manufacturing condition is established, there is a cost advantage. In the case of LPE film, the prescribed Faraday rotation is obtained with as thin film as possible, so Bi substitution film is used, although with the Bi substitution garnet the temperature dependency of its Faraday rotation angle is a little larger than that of YIG.

2) Bi substitution single crystals in bulk are produced by the flux method. Since this does not have a substrate like the LPE film, it is suited for miniaturization. However, the flux method itself has many instability factors with a scattering of Faraday rotation. Thickness control therefore tends to be difficult.

3) Based on these considerations, for high-performance optical isolators that have the appropriate temperature properties and wavelength properties, YIG single crystals made by the FZ method are used. For optical isolators for miniaturization to match the LD modules, LPE or Bi type garnet produced by the flux method appear to be used.

7. Magnetic Circuitry of Cylindrical Magnet

How to magnetize Faraday-rotation materials (Faraday rotator) uniformly is a critical question in device design. But while there is a great deal of knowhow in this field, not many reports are available.

As shown in Figure 2, normally a Faraday rotator is placed inside a cylindrical magnet and subjected to magnetization. The size of this Faraday rotator determines the optimum size and dimensional ratio of the cylindrical magnet. This will not be discussed in detail, but the basic properties of the cylindrical magnet are as follows:

Figure 11 illustrates the changes in the magnetic field on the central axis when magnet thickness L is changed, with the ratio of inner diameter to outer diameter of the cylindrical magnet ($\alpha = D_0/Di$) constant. When the magnet thickness L is thin, the magnetic field distribution curve exhibits a single peak property, whereas a double peak property appears when L is thick. The intensity of the central magnetic field reaches a maximum of Hm with a thickness of Lm.

$$\frac{Lm}{Di} = \frac{\alpha^{2/3}}{\sqrt{\alpha^{2/3}+1}} \qquad (1)$$

$$Hm = Br \frac{\alpha^{2/3}-1}{\sqrt{1+\alpha^{2/3}+\alpha^{4/3}}} \qquad (2)$$

When the ratio of inner diameter to outer diameter $\alpha = D_0/Di$ is large, the central magnetic field Hm is large. In this case, Br is the magnet's

residual magnetic flux density. Also, at a thickness of Lw, the magnetic field distribution curve changes from a single peak to a double peak.

$$\frac{Lw}{Di} = \alpha^{2/5} \sqrt{\frac{\alpha^{6/5}-1}{\alpha^{4/5}-1}} \tag{3}$$
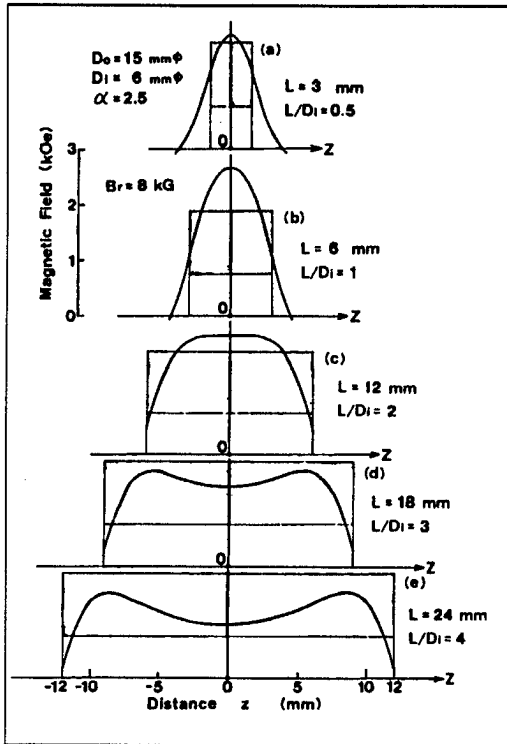

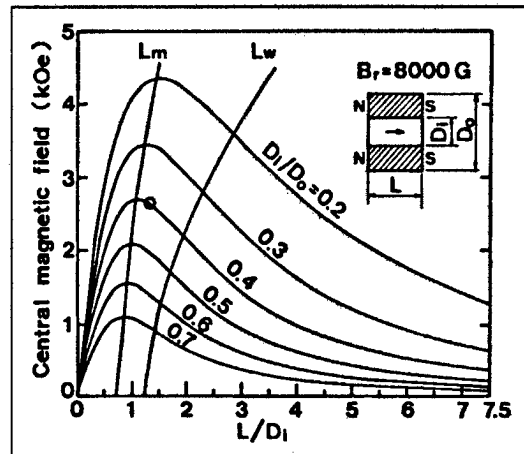Figure 11. Magnetic Field Distribution on Central Axis When Thickness of Cylindrical Magnet Changes

Figure 12. Correlation Between Dimensional Ratio and Central Magnetic Field Intensity of Cylindrical Magnet

Figure 12 shows thickness L/Di normalized by the inner diameter on the transverse axis and the magnetic field intensity on the vertical axis, where residual magnetic flux density Br is set at 8000 G. The curve on the left side in Figure 12 is the result of plotting the points of the maximum magnetic field as calculated from formula (1), while the curve on the right side is the result of plotting transition points from single peak to double peak as calculated from formula (3).

When in actual use, an optical isolator having much magnetic field intensity as possible and good magnetic field distribution is preferable. This means that the region between curves Lm and Lw in Figure 12 is best suited.

8. Two-Step Optical Isolator

For measuring coherent optical communication and high-precision light, an optical isolator having a reverse loss in excess of 60 dB is necessary. To

79

realize this, a two-step optical isolator is required. The two-step optical isolator coupled with optical fiber was already described in Subsection 4.2.

Recently a new high-performance two-step optical isolator for spatial propagation has been developed. As shown in Figure 13, this has two optical isolators arranged in such a way that the permanent magnet will repel. This arrangement provides the advantage that the Faraday rotation angle of the first optical isolator is mutually in reverse to that of the second optical isolator, so that the polarization face will not be rotated by the incident beam and the transmitted beam.
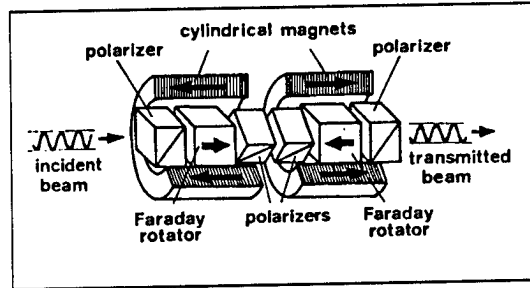

Figure 13.   Diagram Showing Principle of Spatial
Propagation Type Two-Step Optical Isolator

Also, when the two-step optical isolator determines the role to be played by each optical isolator--for example, low-temperature side, high-temperature side, short wavelength side, and long wavelength side--the result is the realization of an optical isolator with temperature stability over a wide band.

The properties of a two-step optical isolator having the structure shown in Figure 13 are illustrated in Figure 14.   An optical isolator meeting the specifications of a reverse low of over 60 dB and an insertion low of under 2 dB over a range of -20 ~ 60°C at 1.55 ± 0.02 μm has been developed.
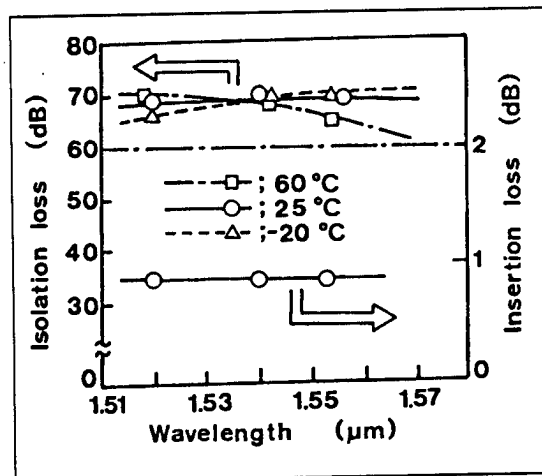

Figure 14.   Properties of Spatial Propagation Type
Two-Step Optical Isolator

80

9. Conclusion

A comparison of the optical isolator with the microwave isolator shows a surprising degree of similarity. in the case of microwave, the isolator's role of protecting the oscillator from disturbance is identical. Even in the case of coherent optical communication, microwave means all coherent communication, so the same principle applies. Note that the waveguide type optical isolator, which is equivalent to the edge guide mode in microwave, has not been studied yet. This should be a topic of future research.

From the authors' experience in developing microwave isolators, potential demand from the system side for the function can be simply summarized: "If possible, we would like to dispense with it." However, the fact is that microwave isolators have now become an indispensable device for improvement of the quality of communication and effective utilization of wavelength.

Now that monolithic semiconductor devices are predominant, optical isolators, like the mass of magnetic materials, may be considered controversial. Nevertheless, we venture to say, despite fear of speaking from a self-centered viewpoint, that the introduction of controversial elements to some degree contributes to creating harmonious systems beneficial for mankind. It is anticipated that with advances in optical communication in the future, the market of optical isolators will expand more and more.

20107/9365

Methods of Quantum Noise Control in Communications

[Article by M. Nakagawa, et al., Keio Gijuku University]

[Text] 1. **Introduction**

There is no denying that communication is indispensable to our social life. Of the means of communication available, optical communication is one that can transmit large volumes of data at high speed and with high reliability to another party. Optical communication is replacing telecommunication and is steadily consolidating its position as the next century approaches.

Man's greatest interest in regard to communication lies in whether transmitted signals go through transmission lines, survive a variety of interference elements such as attenuation and noise, and reach another party with certainty. As far as optical communication is concerned, this interest may be put as follows: How far can signals be transmitted through fiber without relay? Is optical communication possible over a very great distance from one satellite to another? If possible, how many mW are required for the emission output to cope with interference elements? What about the type of optical detector required? What about the modulation type and code type? If there were absolutely no interference elements, even signals of minute output could reach the other party, but interference elements are an essential fact of communication.

Interference elements in optical communication can be roughly divided into two types. One is elements common in telecommunications: attenuation of signals due to fiber, attenuation generated by an expanding beam as light advances in a vacuum, thermal noise generated in an electric circuit after light has been detected, and so on. The other is quantum noise, which hardly poses a problem in telecommunication at a lower frequency than light, but which cannot be ignored in such a high frequency signal as that of light.

In this paper, after explaining quantum noise, methods to alleviate the effect of this unavoidable noise with respect to data transmission will be discussed.

2. Quantum Noise Defying All Attempts at Elimination

The use of light is not confined to the technical field called telecommunication. Man uses it in everyday life. Without it, life would be impossible. The twofold nature of light, the fact that it has a particle property and a wave motion property, is well known. Of these two physical properties, the wave motion property of light is what we experience often in our daily life. For example, a romantic rainbow across the sky after rain shows us that the sunlight is a collection of rays with different wavelengths. But the particle property is something that very few people experience every day. Generally, each light particle cannot be seen; light appears to our eyes as a physical quantity having a specific strength. However, many people must have had experience with a geiger counter that measures radiation with a higher frequency than light. The geiger counter uses a speaker sound to clearly indicate the existence of radiation. It is that scratching sound, "click, click." When a radiation particle enters, it gives off a "click." The next particle enters, another "click." The time interval between particles is random, not fixed. As a result, this is heard as a sound containing irregular components. When this is converted into electric waveform for observation, a pulse line is seen in a state of great noise. Each particle of radiation flies without affecting another, so it has become a waveform in this noise state to be converted to a sonic or electric signal. The noise waveform component of this signal is called quantum noise.

The energy of radiation particles is far stronger than that of light particles, so we clearly detect the existence of radiation particles and that of quantum noise. In the case of light, since its energy is lower than that of radiation, there are few chances of detecting the quantum noise.

However, when optical signals are detected by highly sensitive light-receiving elements, this "click, click" noise (quantum noise) from the same particles (photons) is detected. In optical communication, to provide high reliability, a fixed intensity of light (number of photons) is required. Quantum noise is a major interference in meeting this requirement. In optical communication, in addition to quantum noise, thermal noise familiar in electric circuits, background optical noise and dark current noise coexist. Thermal noise can be substantially eliminated by cooling. Background optical noise and dark current noise can be considerably reduced by the system construction method; theoretically, they can be completely eliminated. On the other hand, quantum noise exists like some tough germ that cannot be killed by boiling or burning; it is the final determining factor of the reliability of the communication system. The ratio of quantum noise to thermal noise of a signal light with frequency f is given by hf/kT (h: Planck's constant, k: Boltzmann's constant, T: temperature). For example, at $f = 10^{15}$ Hz and T = 300 k (normal temperature), hf/kT is approximately 160. It is hoped that this explanation has made clear why we fear quantum noise in optical communication.

Then, are we to understand that quantum noise is so inevitable that nothing can be done about it in optical communication? Recently, there have been some who do not agree with that view.

Before we hear what those who disagree have to say, let us think about quantum noise, in which the wave motion property is involved, in the next section.

3. Quantum Noise Accompanying Wave Motion Property of Light

When light is treated as a wave, the quantum noise explained in the previous section appears as wave phase and amplitude sway.

Consider light signal $S(t)$ with a single frequency fs ($= \omega_s/2\ \pi$).

$$S(t) = A \cdot \cos\ (\omega_s\ t + \theta) \tag{1}$$

In this instance, quantum noise is observed as sway in amplitude A and phase θ. If the signal is rewritten as $A\cos\theta = Xc$, $A\sin\theta = Xs$, the following equation is obtained.

$$S(t) = Xc \cdot \cos\omega_s\ t - Xs \cdot \sin\omega_s\ t \tag{2}$$

In this case, the following relationship of uncertainty exists between the two orthogonal phase components, Xc and Xs, of the amplitude according to Heisenberg's principle of uncertainty.

$$\Delta Xc^2 \cdot \Delta Xs^2 \geq 1/16 \tag{3}$$

ΔXc^2 and ΔXs^2 are determined by the property of the signal light (quantum state), and formula (3) shows that they cannot be freely made small. Then, let us look at how different quantum noise becomes depending on the properties of light. The coherent state which is most familiar as the laser output state is the minimum state of uncertainty where the equality sign holds in formula (3). Moreover, the size of sway of Xc and Xs at this time is equal to 1/4, and noise in good balance is obtained (no phase dependency). As is known, the beams of light radiated by lightbulbs and light-emitting diodes that are around us can be expressed as the statistical coupling state in the coherent state. Hence, the quantum noise which these beams of light have meet the relationship $\Delta Xc^2 = \Delta Xs^2 \geq 1/4$.

As explained above, in light that can be expressed as the coupling state in the coherent state, the pure coherent state exists when there is a minimum of quantum noise. The quantum noise level ($= 1/4$) at this time is generally referred to as the "quantum noise limit." Then, is this quantum noise limit a hurdle that cannot be overcome?

4. Quantum State Control and Quantum Control Communication

One of the recent research themes of quantum optics is "quantum state control." Controlling the quantum state means generating light (quantum state) that cannot be expressed by statistically overlapping the coherent state. The uncertainty relationship of formula (3) is a condition only for the uncertainty product of the two orthogonal phase components, and no limits whatsoever are imposed on each component. Consequently, the size of

84

the sway of the two components may be out of balance ($\Delta Xc^2 = \Delta Xs^2$). When the sway of the two components is in a state of imbalance like this, it is called a squeezed state. In the squeezed state, ΔXc^2 can be made less than 1/4 by making ΔXs^2 larger than 1/4 while maintaining the minimum state of uncertainty (Figure 1). This squeezed state cannot be expressed by the statistical coupling state in the coherent state. Although the squeezed state can be generated by using nonlinear optical elements, the main generating methods are degenerated parametric conversion and four lightwave mixing. Studies of the squeezed state have been actively pursued since 1978, and it has been observed in experiments.
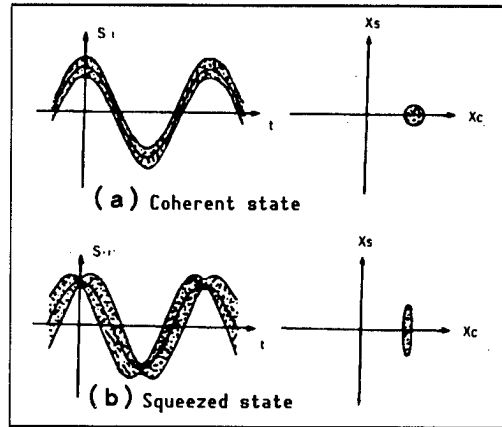

Figure 1. Quantum Noise

Communication using light with a controlled quantum state such as the squeezed state is defined as "quantum control communication." When using the squeezed state as signal light, the coherent communication system using the wave emotion property of light is effective. Because the optical frequency is extremely high ($\approx 10^{15}$ Hz), direct detection of the signal light can neither produce the frequency of light nor the data in phase. Therefore, the receiving side takes the beat of the signal light and local oscillation light (LO light which is in the coherent state), lowers the frequency and receives the signal (Figure 2).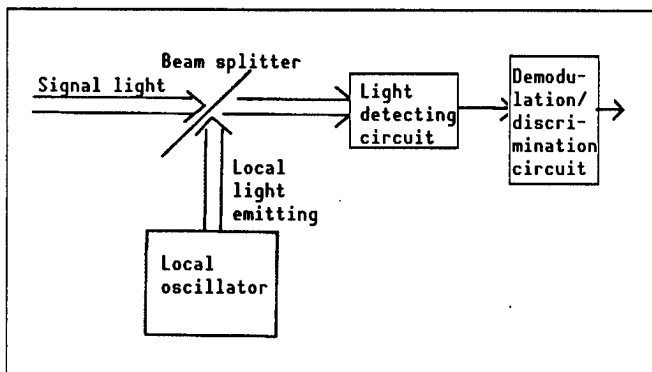 this is called coherent detection. A system in which the frequency of the signal light differs from that of the LO light is called a heterodyne detection system, while a system in which both frequencies are identical is called a homodyne detection system. Of these two system,s the homodyne detection system can make maximum use of the advantages of the squeezed state by matching the phase of the LO light to that of the signal light in the squeezed state having a minimum of noise. Now, let us see how reliability

Figure 2. Coherent Detection Method

is improved by using light in the squeezed state for the signal instead of in the coherent state.

For a communication system, the two-value phase modulation homodyne (BPSK homodyne) detection system will be used to make the most of the merits of the squeezed state. The reliability of the communication system can be evaluated in terms of the signal-to-noise ratio (SNR) that determines the signal power (average number of photons) and the bit error rate (BER). At this time, the BER can be given as follows using the SNR of the signal light:

$$BER = \frac{1}{\sqrt{2\pi}} \int_{\sqrt{SNR}}^{\infty} \exp[-x^2/2] \, dx \qquad (4)$$

If the average number of photons contained in 1 bit of signal is given as <n>, the SNR of light in the coherent state (quantum noise 1/4) becomes 4<n>. In the case of the squeezed state, conditions to maximize the SNR were obtained by Yuen, et al. The SNR at this time becomes 4<n> • (<n> + 1) and has an SNR <n> + 1 times that of light in the coherent state. Figure 3 shows SNRs in the coherent state and in the squeezed state. From this it is clear that use of the squeezed state remarkably improves the SNR.
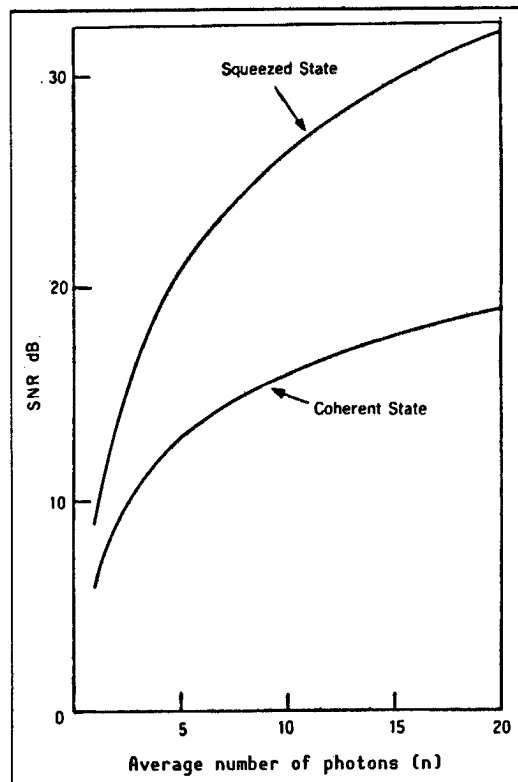

Figure 3. SNR Improvement Through Quantum State Control

In coherent communication, phase synchronization of the signal light and the LO light carries very large weight in determining system reliability. In the case of using light in the squeezed state for communication, its unbalanced quantum noise properties are responsible for creating several problems that would not be posed in the coherent state. They are:

(1) Because of the phase dependency of quantum noise, a slight shift between the phase of the signal light and that of the LO light causes major performance deterioration.

(2) Since signals for synchronization are orthogonal to the data-carrying components, quantum noise is larger than 1/4.

(3) Diffusion of the refractory index in the transmission line causes a phase shift of the signal light, and the signal power moves to components with a great deal of noise, greatly diminishing performance.
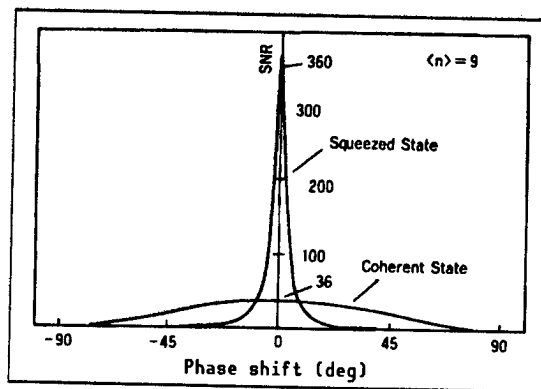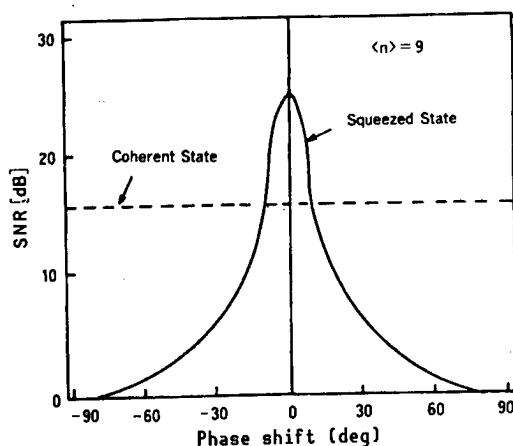

Figure 4. SNR Deterioration Properties From Phase Shift Between Signal Light and Local Light Emission

The first problem is shown in Figure 4. The average number of photons $\langle n \rangle$ is nine and the squeezed state shows that the SNR is in the maximum state. This indicates that in the coherent state, the SNR deterioration due to the phase shift from LO light is not too sensitive to the phase difference, but in the squeezed state, drastic deterioration occurs. Moreover, when the phase difference between the signal light and the LO light is more than approximately 10°, it is clear that the SNR has become worse than in the coherent state. The second problem is, as is clear from Figure 1, the signal for synchronization is carried on the component in which quantum noise is the maximum, so accurate synchronization becomes difficult, thus causing the first problem. Also, SNR deterioration due to phase shift is a problem that does not occur in the coherent state. This is also serious when the phase difference between the signal light and the LO light is nil (Figure 5). Also, performance deterioration at this time is very steep, and this trend becomes more intense as the average number of photons increases.

In the next section, a synchronous system to resolve these problems will be proposed and its operation will be explained.

(a) SNR deterioration properties from signal
    light phase shift (no phase difference
    between signal light and local light
    emission)
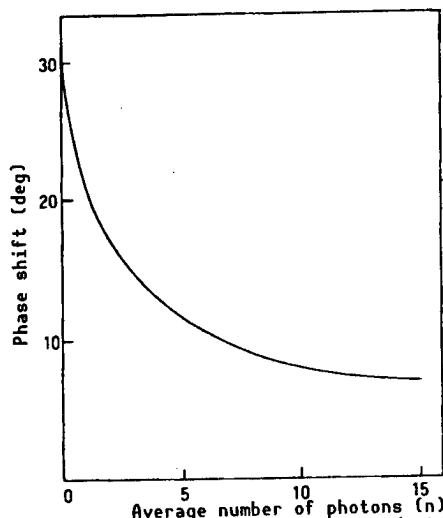
(b) Phase shift when SNR in squeezed state
    equals that in coherent state

Figure 5.

5. Synchronous System for Squeezed State Signals

In Figure 6, a block diagram of a synchronous system to resolve the problems
is shown (the symbols are PS for phase shifter, CP for directional coupler,
PD for photo detector, LPF for low pass filter, and MP for microprocessor).
This system is composed of the optical phase-locked loop (PLL), which has
been modified for detection signals in the squeezed state, and the
transmission line phase shift canceler to eliminate effects of phase shift
on the transmission line.

First, an explanation of the light PLL operation will be made. This light
PLL operates basically on the same principle as the decision driven-PLL.
It is characterized by the use of four directional couplers, for

photodetectors, and two differential amplifiers to make up two balanced-mixers (note: of the two quantum noises, signal light, and LO light, one can be eliminated in the balanced-mixer). One uses the data detection branch to mix the signal light and the LO light to cancel the quantum noise of the LO light. On the other hand, the branch for phase synchronous signals uses another balanced-mixer conversely to cancel the quantum noise (larger than 1/4) of the signal light and mix so that no effects of that are received. By mixing these two beams of light, respectively, the branch for data detection maintains the advantages of the squeezed state signals, while the branch for phase-locked signals must detect the component with a great deal of quantum noise out of the two DC/AC phase amplitudes of the squeezed state signals. But by canceling that N, the quantum noise of the LO light in the coherent state becomes dominant, so the conventional theory of coherent state signals can be used as is.
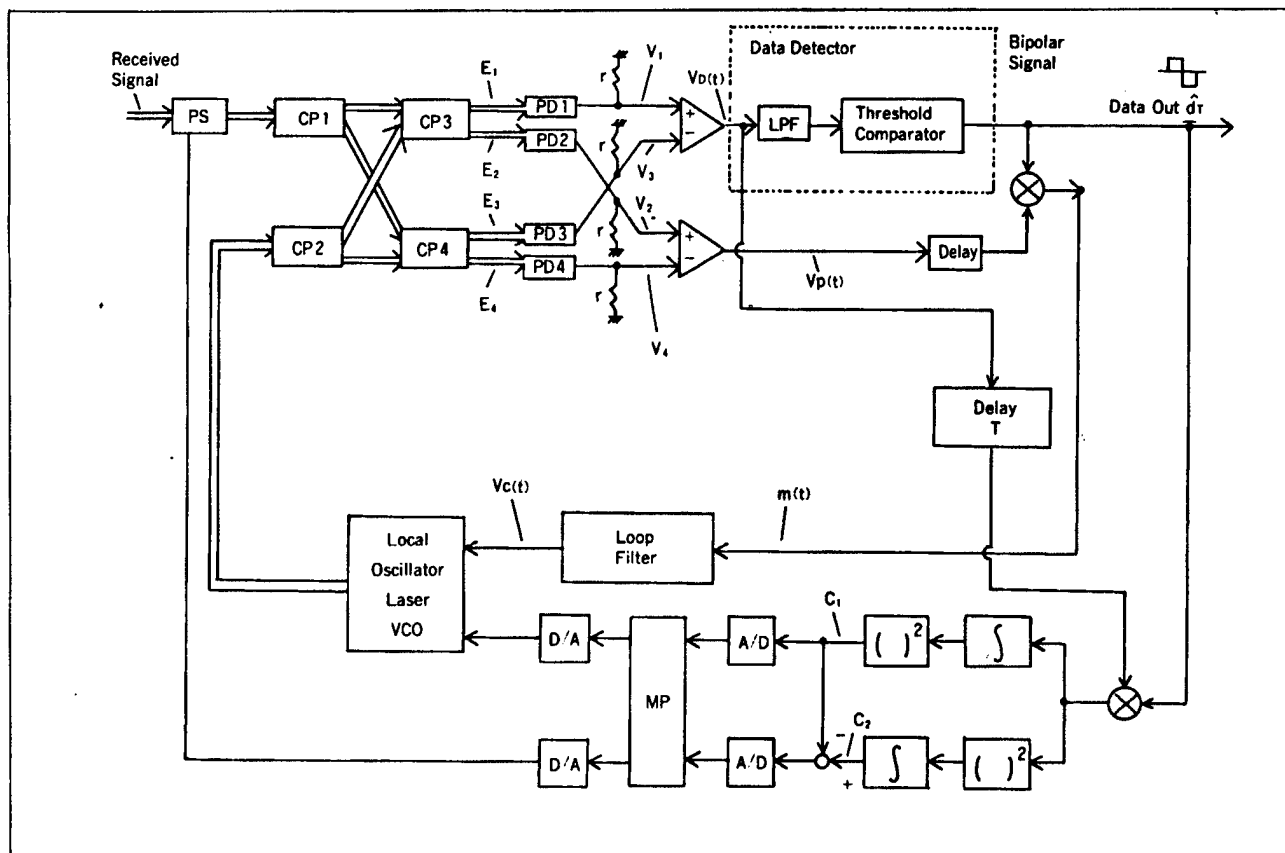

Figure 6. Synchronization System for Squeezed State Signals

Another system, the transmission line phase shift canceler, will be explained. Since from time to time, this system measures the SN ratio of the DATA signals detected and uses it as an evaluation function to perform loop control, it takes the form of digital signal processing (DSP). First, the DATA signal immediately after detection is delayed 1 bit to cancel the data component, then it is multiplied by ±1 DATA as appropriate. The signal

power and noise power of this signal are obtained by the integrator, square machine, and adding machine. (C1 in Figure 6 indicates signal power, C2 the total of signal power and noise power.) This output is used to compute the SN ratio by microprocessor, and based on this result, the phase shifter uses electrical engineering elements to control the phase of the signal light. The output of the microprocessor is connected to the LO light in order to compensate for the deterioration of stability of light PLL by this phase shift canceler, and even in the LO light, the shift is the same size as the phase fluctuation of the signal light. Also, changes in the phase shift of this transmission light must not be too rapid, so that the DSP system can adequately follow.

By using these systems, the problems concerning phase synchronization of the squeezed state signals with unbalanced quantum noise distribution can be solved.

6. Conclusion

The foregoing provided an outline of the quantum control communication system, problems concerning synchronization, and their solution. It would not be true to say that quantum control communication has no problem. The biggest problem of quantum state control is the decrease in its advantages as a result of loss. When there is no loss, the squeezed state signal has an SNR that is a maximum of $<n>$ + 1 times that of the coherent state. But once loss occurs, the SNR drastically deteriorates. In a communication system with a loss over 3 dB, improvement of the SNR can bring the loss to under 3 dB. However, for communication, the loss on the transmission line is so great that use of the squeezed state for the transmission light source does not provide adequate results. To solve this loss problem, it has recently been proposed to use the "communication system to conduct quantum state control on the receiving side," utilizing the fact that the properties in the coherent state are not affected by loss (Figure 7). It has been demonstrated that this exhibits very good properties.
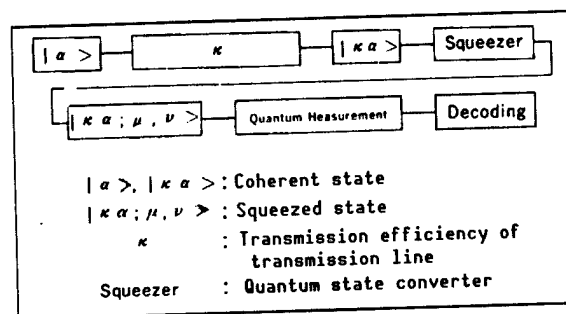

Figure 7. Receiving Quantum State Control Communication System

There are several problems yet to be resolved in the quantum control communication system. By solving them one by one, this system will definitely be realized in the near future as the next-generation high-reliability communication system.

20107/9365   - END -

/10

Foreign Broadcast Information Service (FBIS) and Joint Publications Research Service (JPRS) publications contain political, economic, military, and sociological news, commentary, and other information, as well as scientific and technical data and reports. All information has been obtained from foreign radio and television broadcasts, news agency transmissions, newspapers, books, and periodicals. Items generally are processed from the first or best available source; it should not be inferred that they have been disseminated only in the medium, in the language, or to the area indicated. Items from foreign language sources are translated; those from English-language sources are transcribed, with personal and place names rendered in accordance with FBIS transliteration style.

Headlines, editorial reports, and material enclosed in brackets [ ] are supplied by FBIS/JPRS. Processing indicators such as [Text] or [Excerpts] in the first line of each item indicate how the information was processed from the original. Unfamiliar names rendered phonetically are enclosed in parentheses. Words or names preceded by a question mark and enclosed in parentheses were not clear from the original source but have been supplied as appropriate to the context. Other unattributed parenthetical notes within the body of an item originate with the source. Times within items are as given by the source. Passages in boldface or italics are as published.

SUBSCRIPTION/PROCUREMENT INFORMATION

The FBIS DAILY REPORT contains current news and information and is published Monday through Friday in eight volumes: China, East Europe, Soviet Union, East Asia, Near East & South Asia, Sub-Saharan Africa, Latin America, and West Europe. Supplements to the DAILY REPORTs may also be available periodically and will be distributed to regular DAILY REPORT subscribers. JPRS publications, which include approximately 50 regional, worldwide, and topical reports, generally contain less time-sensitive information and are published periodically.

Current DAILY REPORTs and JPRS publications are listed in *Government Reports Announcements* issued semimonthly by the National Technical Information Service (NTIS), 5285 Port Royal Road, Springfield, Virginia 22161 and the *Monthly Catalog of U.S. Government Publications* issued by the Superintendent of Documents, U.S. Government Printing Office, Washington, D.C. 20402.

The public may subscribe to either hardcover or microfiche versions of the DAILY REPORTs and JPRS publications through NTIS at the above address or by calling (703) 487-4630. Subscription rates will be provided by NTIS upon request. Subscriptions are available outside the United States from NTIS or appointed foreign dealers. New subscribers should expect a 30-day delay in receipt of the first issue.

U.S. Government offices may obtain subscriptions to the DAILY REPORTs or JPRS publications (hardcover or microfiche) at no charge through their sponsoring organizations. For additional information or assistance, call FBIS, (202) 338-6735,or write to P.O. Box 2604, Washington, D.C. 20013. Department of Defense consumers are required to submit requests through appropriate command validation channels to DIA, RTS-2C, Washington, D.C. 20301. (Telephone: (202) 373-3771, Autovon: 243-3771.)

Back issues or single copies of the DAILY REPORTs and JPRS publications are not available. Both the DAILY REPORTs and the JPRS publications are on file for public reference at the Library of Congress and at many Federal Depository Libraries. Reference copies may also be seen at many public and university libraries throughout the United States.